SCUOLA NORMALE SUPERIORE

PH. D. THESIS

Addressing the drug-delivery endosomal-entrapment issue through a CPP-AMP chimeric peptide

Fabrizio Salomone

ADVISORS

Fabio Beltram

Francesco Cardarelli

2015

To Deburini

Foreword

This thesis is the result of my research activity at the NEST laborarory of Scuola Normale Superiore in Pisa: I began my studies on the endosomal entrapment issue in 2009, prompted by the group interest in the molecular biophysics approach to drug-delivery issues. This research was carried out within a joint PhD program sponsored by Scuola Normale Superiore and Italian Institute of Technology.

List of publications

F Salomone, F Cardarelli, M Di Luca, C Boccardi, R Nifosì, G Bardi, L Di Bari, M Serresi, and F Beltram.
"A novel chimeric cell-penetrating peptide with membrane-disruptive properties for efficient endosomal escape"
Journal of Controlled Release 163 (2012) 293-303

F Salomone, F Cardarelli, G Signore, C Boccardi, and F Beltram.
"In vitro efficient transfection by CM_{18}-Tat_{11} hybrid peptide: A new tool for gene-delivery applications "
PLoS ONE 8 (2013) e70108

A Fasoli*, F Salomone*, M Benedusi, C Boccardi, G Rispoli, F Beltram, and F Cardarelli. * co-authorship
"Mechanistic insight into CM_{18}-Tat_{11} peptide membrane-perturbing action by whole-cell patch-clamp recording"
Molecules 19 (2014) 9228-9236

F Salomone, M Breton, I Leray, F Cardarelli, C Boccardi, D Bonhenry, M Tarek, LM Mir, and F Beltram.
"High-yield non-toxic gene transfer through conjugation of CM_{18}-Tat_{11} chimeric peptide with nanosecond electric pulses"
Molecular Pharmaceutics 11 (2014) 2466-2474

Publications not included in this thesis:

L Albertazzi, FM Mickler, GM Pavan, F Salomone, G Bardi, M Panniello, E Amir, T Kang, KL Kilops, C Brauchle, RJ Amir, and CJ Hawker
"Enhanced bioactivity of internally functionalized cationic dendrimers with PEG cores"
Biomacromolecules 13 (2012) 4089-4097

G Caracciolo, F Cardarelli, D Pozzi, F Salomone, G Maccari, G Bardi, A Capriotti, C Cavaliere, M Papi, and A Laganà.
"Selective targeting capability acquired with a protein corona adsorbed on the surface of 1,2-dioleoyl-3-trimethylammonium propane/DNA nanoparticles"
ACS Applied Materials & Interfaces 5 (2013) 13171-13179

D Pozzi, C Marchini, F Cardarelli, F Salomone, S Coppola, M Montani, ME Zabaleta, MA Digman, E Gratton, V Colapicchioni, and G Caracciolo.
"Mechanistic evaluation of the transfection barriers involved in lipid-mediated gene delivery: interplay between nanostructure and composition"
BBA – Biomembranes 1838 *(2014) 957-967*

D Pozzi, F Cardarelli, F Salomone, C Marchini, H Amenitsch, G La Barbera, and G Caracciolo. "An intracellular lamellar-nonlamellar phase transition razionalizes the efficiency boost of cholesterol-containing lipoplexes"
Applied Physics Letters

Table of Contents

Introduction **1**

1 CM_{18}-Tat_{11} chimeric peptide: a new tool to tackle the endosomal escape issue **5**

1.1 Endocytosis **6**

1.1.1 Phagocytosis 10

1.1.2 Macropinocytosis 11

1.1.3 Clathrin-mediated pathway 12

1.1.4 Caveolin-mediated pathway 13

1.1.5 Flotillin-dependent pathway 15

1.1.6 GRAF1-dependent pathway 16

1.1.7 Arf6-dependent pathway 17

1.1.8 RhoA-dependent pathway 17

1.2 The endosomal escape issue **18**

1.2.1 Endosomal escape mechanisms 18

1.2.2 Viral-protein-derived peptides 21

1.2.3 Synthetic peptides 22

1.2.4 α-helical antimicrobic peptide: an unconventional tool to overcome endosomal entrapment 24

1.3 CM_{18}-Tat_{11}: a chimera peptide exploiting cell-penetrating peptides and AMPs properties **29**

2 CM_{18}-Tat_{11} functional design and cargo-delivery applications **33**

2.1 Characterization of CM_{18}-Tat_{11} structure and membrane interaction **35**

2.1.1 CM_{18}-Tat_{11} primary and secondary structure study 35

2.1.2 CM_{18}-Tat_{11} interaction with biological membranes 37

2.2 Evaluation of CM_{18}-Tat_{11} as a drug-delivery vector **43**

2.2.1 CM_{18}-Tat_{11} promotes the escape of Tat_{11}-EGFP fusion protein from endosomal vesicles 43

2.2.2 Quantitative analysis of CM_{18}-Tat_{11}-induced cargo release from vesicles 45

2.2.3 CM_{18}-Tat_{11} promotes the cytoplasmic delivery of different size dextrans 49

2.3 CM_{18}-Tat_{11} drug-delivery system overview **51**

3 CM_{18}-Tat_{11} as a tool for *in vitro* gene-delivery 55

3.1 CM_{18}-Tat_{11}/pDNA complexes: physicochemical properties and transfection efficiency evaluation 57

3.1.1 CM_{18}-Tat_{11}/pDNA binding ability: vector characterization 57

3.1.2 *In vitro* transfection efficiency 60

3.2 Gene vector intracellular trafficking 62

3.2.1 FRET-based real-time imaging of cell uptake dynamics 62

3.2.2 Complex integrity evaluation in endosomal-like conditions 66

3.3 Concluding remarks 68

4 CM_{18}-Tat_{11} membrane-perturbing activity in living cells 71

4.1 CM_{18}-Tat_{11} intravesicular localization 73

4.1.1 Static dielectric constant imaging by a GFP chromophore analog 73

4.1.2 Ratiometric imaging by confocal microscopy and image analysis 75

4.1.3 Evaluation of peptides intravesicular spatial distribution 76

4.2 CM_{18}-Tat_{11} membrane-perturbing mechanism 80

4.2.1 Whole-cell patch clamp analysis of membrane exogenous currents 80

4.2.2 Membrane-perturbing mechanism evaluation 83

5 Concluding remarks and research perspectives 87

Appendices 93

A High-yield, non-toxic gene transfer by CM_{18}-Tat_{11} and nanosecond electric pulses 95

B Methodological considerations 107

Bibliography 121

List of Figures

Fig. 1.1 Mechanisms of extracellular uptake by endocytosis in a typical eukaryotic cell. 7

Fig. 1.2 Schematics of the different endocytic compartments. 9

Fig. 1.3 Macropinocytosis schematic representation 12

Fig. 1.4 Clathrin-mediated pathway schematic representation 13

Fig 1.5 Summary of endocytic pathways that take place in lipid raft domains of the cell membrane and some of their key regulators 15

Fig. 1.6 Emblematic examples of endosomolysis mechanisms 20

Fig. 1.7 AMP amphipatic α-helical structure 25

Fig. 1.8 Cecropin-A/Melittin sequences combinations 29

Fig. 1.9 Helical wheel display of the cecropin-mellitin hybrid, CM_{15} 30

Fig. 2.1 Peptides sequences and CD spectra 36

Fig. 2.2 CM_{18}-Tat_{11} MD simulation 37

Fig. 2.3 Peptide toxicity assays 38

Fig. 2.4 Effect of heparin on peptides uptake 39

Fig. 2.5 Cell uptake and cytotoxicity of peptides 41

Fig. 2.6 CM_{18}-Tat_{11} internalization route studied by confocal microscopy 42

Fig. 2.7 Intracellular distribution of Tat_{11}-EGFP recombinant protein 43

Fig. 2.8 CM_{18}-Tat_{11}-driven cytosolic release of Tat_{11}-EGFP recombinant protein 44

Fig. 2.9 CM_{18}-Tat_{11}-driven cytosolic release of Calcein 46

Fig. 2.10 PI assay on Calcein-releasing cells and CM_{18}-Tat_{11}-mediated release of Calcein in different cell lines 47

Fig. 2.11 Flow cytometry analysis 48

Fig. 2.12 Quantitative analysis of Calcein release kinetics 49

Fig. 2.13 CM_{18}-Tat_{11}-driven cytosolic release of different-size dextrans 50

Fig. 2.14 Calcein and CM_{18}-Tat_{11} cell distribution at different CM_{18}-Tat_{11} concentrations 52

Fig. 2.15 Schematic model of CM_{18}-Tat_{11}-mediated vesicle destabilization and cargo release 53

Fig. 3.1 CM_{18}-Tat_{11}/pDNA complex characterization 58

Fig. 3.2 ξ-potentials of CM_{18}-Tat_{11}/pDNA nanoparticles 59

Fig. 3.3 CM_{18}-Tat_{11}/pDNA complex *in vitro* transfection efficiency and cytotoxicity 60

Fig. 3.4 CM_{18}-Tat_{11}/pDNA *in vitro* transfection efficiency in CHO-K1 cells 61

Fig. 3.5 Spectroscopic properties of peptides-atto633/pDNA-Cy3 complexes 62

Fig. 3.6 Cell uptake dynamics of peptides-atto633/pDNA-Cy3 complexes 64

Fig. 3.7 Acceptor photobleaching assay 65

Fig. 3.8. Intracellular final fate of DNA/peptide complex in HeLa cells 66

Fig. 3.9 *In vitro* peptide/pDNA complex stability evaluation in endosomal-like conditions 67

Fig. 3.10 Graphical scheme of CM_{18}-Tat_{11}/pDNA binary complexes disassembling evolution 69

Fig. 4.1. Polarity probe labeling and spectroscopic characterization 74

Fig. 4.2 Nomarsky images and polarity maps of CHO-K1 cells 77

Fig. 4.3 Medium ε distribution in cell population and schematic vesicular membrane localization 79

Fig. 4.4. The experimental set employed to investigate the permeabilisation properties of CM_{15} inserted in a natural eukaryotic membrane 80

Fig. 4.5. Outline of the technique employed.....81

Fig. 4.6. Kinetics of peptide-induced membrane permeabilization of CHO-K1 cells.....83

Fig. 4.7. Schematic representation of the membrane destabilization mechanis.....85

Fig. 5.1. CM_{18}-Tat_{11}–siRNA complex characterization.....89

Fig. A.1 Qualitative evaluation of GUVs exposure to CM_{18}-Tat_{11} +/- 10 ns electric pulse(s) 97

Fig. A.2 Quantitative evaluation of GUVs exposure to CM_{18}-Tat_{11} or 10 ns electric pulse(s) 98

Fig. A.3 Quantitative evaluation of GUVs exposure to peptides or +/- 10 ns electric pulse.....99

Fig. A.4 Vector/pDNA complex +/- 40 ns electric pulses *in vitro* TE and cytotoxicity 100

Fig. A.5 YO-PRO-1 assay on cells exposed to CM_{18}-Tat_{11} +/- 40 ns electric pulses 101

Fig. A.6 MD simulation of POPC bilayer patch exposure to CM_{18}-Tat_{11} and 10 ns electric pulse.....103

Fig A.7 MD simulation of CM_{18} molecular interaction with a membrane bilayer during NP shooting.....104

Fig A.8 MD simulation of Tat_{11} molecular translocation through a membrane bilayer during NP shooting.....104

Fig. A.9 Schematic model of CM_{18}-Tat_{11} and NPs cooperative endosomal vesicle perturbation and pDNA release.....106

List of Tables

Tab. 1.1 Sequences and endosomal escape mechanisms of selected endosomolytic peptides 28

Tab. 3.1 Size distribution of CM_{18}-Tat_{11}/pDNA complexes 59

Introduction

The ability to cross the cellular membrane and gain access to the cell interior, or even to a specific cellular compartment, still represents a major obstacle for any intracellular drug-delivery protocol. During the past two decades a large number of peptides were identified that can drive the cellular import of cargo molecules. Peptide-mediated delivery of bioactive molecules can be a particularly powerful approach, even superior to commonly-used delivery systems (e.g. liposomes, microinjection, electroporation, viral systems). In fact, peptide vectors guarantee high-yield delivery, low toxicity, and the possibility to enter a wide range of target cells. These vectors are collectively called cell-penetrating peptides (CPPs) and are able to trigger the uptake of various biomolecules into the cell.

Among the commonly used CPPs, the arginine-rich motif of Tat protein from HIV-1 (sequence: YGRKKRRQRRR) has attracted much interest owing to its ability to efficiently drive the internalization of a large variety of cargoes, from small particles to proteins, nucleic acids and liposomes, into a vast range of mammalian cell types. In the past years our research group focused also on the study of Tat_{11} peptide intracellular transport biology. We demonstrated that the nuclear localization of different cargoes can be finely tuned by rational mutagenesis of peptide sequence. Despite the variety of biotechnological applications that could result from this knowledge, to date all reports unequivocally show that, when administrated in the cell medium, Tat_{11}-linked cargo molecules are massively sequestered into endosomal vesicles and finally encounter metabolic degradation. This limits their actual intracellular availability, severely hampering any application of Tat_{11} for delivery purposes. I identified this issue as the key point to tackle in my research activity.

In this work linear cationic α-helical antimicrobial peptides (AMPs) were exploited as a new source of aminoacidic sequences with membrane-disruptive properties to complement Tat_{11} properties. Specifically I employed a sequence from

the well-known CM (Cecropin-A and Melittin hybrids) series of AMPs, where various combinations of the hydrophilic N-terminal domain of Cecropin-A are fused to different portions of the hydrophobic N-terminal domain of Melittin. In this thesis, I shall demonstrate that a newly designed chimeric peptide, CM_{18}-Tat_{11}, in which the Tat_{11} motif is fused to the CM_{18} module (KWKLFKKIGAVLKVLTTG, residues 1-7 of Cecropin-A and 2–12 of Melittin) combines the two main desired functionalities for a cell delivery vector: efficient cellular uptake and selective destabilization of endocytic-vesicle membranes. This yields the ability to promote the intracellular release of a vast range of cargoes. Finally, I shall provide novel insights into its membrane-destabilization mechanism.

This thesis is organized as follows:

- In ***Chapter 1*** I shall provide a brief review on the endocytosis process with a special focus on the endosomal entrapment issue in the drug-delivery field. I shall describe exemplary cases for the different classes of peptidic agents developed in order to increase the drug-delivery efficiency by actively perturbing the vesicle membranes, with particular attention to the emerging platform of AMP-derived sequences. Based on the presented knowledge, I shall illustrate the basis for the creation of a new chimeric peptide based on the fusion of Tat_{11} to CM_{18}.

- From ***Chapter 2*** on I am going to report on the experimental part of my thesis. First, I shall present the work carried out to characterize CM_{18}-Tat_{11} chimeric peptide by a physicochemical point of view. I shall demonstrate that the addition of the Tat_{11} module neither affects the typical α-helical secondary structure of CM_{18} nor its membrane-disrupting ability. On the other hand, the Tat_{11} module ensures rapid and effective translocation of the whole chimera from the extracellular medium into endocytic vesicles. As a result, when administered to cells at sub-micromolar concentration, CM_{18}-Tat_{11} is efficiently taken up by the cell and subsequently promotes membrane destabilization of endocytic vesicles. I shall show that the chimeric peptide effectively enhances the escape and subsequent intracellular diffusion of a vast range of co-localized membrane-impermeable molecules (i.e. Tat_{11}-EGFP fusion protein, Calcein, and different-size dextrans) with no detectable cytotoxicity.

- In the first part of ***Chapter 3*** I shall report on the exploitation of CM_{18}-Tat_{11} physicochemical properties and intrinsic modularity for its application as a delivery vector for plasmidic DNA (pDNA), in this case following direct peptide-cargo

conjugation. I shall demonstrate that CM_{18}-Tat_{11}/DNA nanocomplexes can be obtained spontaneously in solution, with controlled size, surface charge, and stability. Based on this, a candidate complex will be identified, that presents the physicochemical properties best suited to yield a combination of high cellular uptake, low cytotoxicity, and efficient plasmid expression. The high delivery yields obtained prompted us to investigate the intracellular vector fate during its route towards the nuclear compartment. Therefore, in the second part of Chapter 3, I shall illustrate how vector intracellular trafficking is monitored in real time and in live cells by confocal microscopy. In particular, fluorescence resonant energy transfer (FRET) between suitably-labeled DNA and peptide modules will be exploited to monitor peptide-DNA disassembly during endocytosis, and correlate this process to transfection timing and efficiency.

- In ***Chapter 4***, I shall look into CM_{18}-Tat_{11} activity and localization inside the endosomal vesicles, with particular attention for the molecular mechanism of membrane bilayer perturbation, compared to the isolated Tat_{11} and CM_{18} modules. By a straightforward combination of a peptide-linked polarity sensor to measure dielectric constants at the peptide location and whole-cell patch clamp analysis of peptide-evoked membrane currents, membrane localization and destabilization properties of the chimeric peptide are investigated. Consequently CM_{18}-Tat_{11} action on the endosomal membrane shall be associated with a "carpet" mechanism, capable of leading to bilayer destabilisation in a detergent-like manner. I shall also highlight a synergetic behavior between the two moieties in the chimera peptide: CM_{18} increase the membrane residence time of Tat_{11}, while the latter promotes the switch of the AMP membrane-perturbing mechanism from "toroidal pore" to "carpet" model.

- In ***Chapter 5*** I shall summarize the main findings of this research activity and discuss some crucial aspects of CM_{18}-Tat_{11} peptide, as its role as prototype for the rational engineering of novel "modular" cell-penetrating peptides with membrane-disruptive properties. Moreover I shall briefly introduce very recent results on the exploitation of CM_{18}-Tat_{11} as a delivery vector for small-interfering RNA (siRNA) molecules.

Chapter

1

CM_{18}-Tat_{11} chimeric peptide: a new tool to tackle the endosomal escape issue

Many potentially powerful therapeutic and diagnostic strategies require the delivery of macromolecules of interest into a specific cellular compartments[1-4]. In fact a variety of bioactive macromolecules, such as plasmid DNA (pDNA), small-interfering RNA (siRNA), antisense oligonucleotides, recombinant proteins, contrast agents, and drugs must access a target intracellular compartment (nucleus, cytosol or mithocondria) to elicit a therapeutic or diagnostic response[5]. However, cellular delivery of macromolecules remains a major challenge and has been an intense area of investigation over the past two decades[5]. Cell-specific delivery of macromolecules is limited by several extracellular and intracellular barriers. Extracellular barriers include instability in hostile biological environments (due to proteases, nucleases, the immune defense and scavenger systems) and non-target cell binding[6]. The plasma membrane represents a major obstacle for the intracellular drug delivery by imposing an extremely selective filter for compound transfer into the intracellular milieu. The hydrophobic nature of phospholipid bilayers hinders direct cell penetration of extracellular-administered macromolecules owing to their high molecular weight and/or unfavorable physiochemical characteristics (i.e. hydrophilic, surface charge, shape, etc...) that prevent advantageous interactions with the lipid phase of the bilayer. This scenario solicits the development of

strategies for the efficient intracellular delivery of macromolecular cargoes[7]. Following interaction with the extracellular side of the plasma membrane, these internalization vectors exploit primarily endocytosis as their route for intracellular relocation of active macromolecules[8].

1.1 Endocytosis

Endocytosis is a constitutive way for a cell to sense its surrounding milieu and acquire macromolecules that are not able to diffuse or be transported through the plasma membrane. In addition to the uptake of extracellular molecules, endocytic processes also regulate surface receptors and receptor interactions (including antigen presentation), cell motility and mitosis, and several signaling cascades[9]. Furthermore, endocytosis represents the primary route exploited by bacteria and viruses to enter cells[10,11]. During endocytosis membrane-enclosed sacs, known as vesicles, pinch off from the plasma membrane (engulfing a sample of the extracellular environment) and move towards the cell interior acting as gateways for the internalization of external solutes and macromolecules (see Fig 1.1). This natural process can be exploited by delivery vectors to bypass the plasma membrane barrier and gain access to the internal milieu. The endocytic system consists of an articulated array of different pathways that vary greatly in cargo selectivity, environmental conditions, intracellular trafficking, maturation and destination[9]. Therefore, a thorough understanding of the various modes of endocytosis and their intracellular itineraries is crucial for the design of efficient macromolecule delivery vectors.

On account of this, I shall discuss the different mechanisms of endocytosis focusing on how internalized materials are sorted within the cell during their intracellular journey. The traditional classification divides the uptake processes in two categories based on the size of the internalized molecules: phagocytosis (i.e. cell eating) and pinocytosis (i.e. cell drinking). Larger particulate matter, including nanomaterial aggregates and opsonized nanoparticles (sizes can be from hundreds of nm to many μm), are captured by phagocytosis[12]. This mechanism is associated with, but not limited to, phagocytic cells such as macrophages, monocytes and dendritic cells. Conversely, pinocytosis is ubiquitous to virtually all eukaryotic cells

and for this case internalizing vesicles typically have a smaller diameter, i.e., in the range of 50 nm to several 100 nm[13]. Pinocytosis provides a large number of alternative gateways for cellular entry. In fact, a growing number of distinct internalization pathways have been identified an these are usually named after either the proteins that mediate membrane invagination and/or the physiological cargoes[14]. Figure 1.1 schematically illustrates the main endocytic mechanisms together with the intracellular fate of internalized materials.

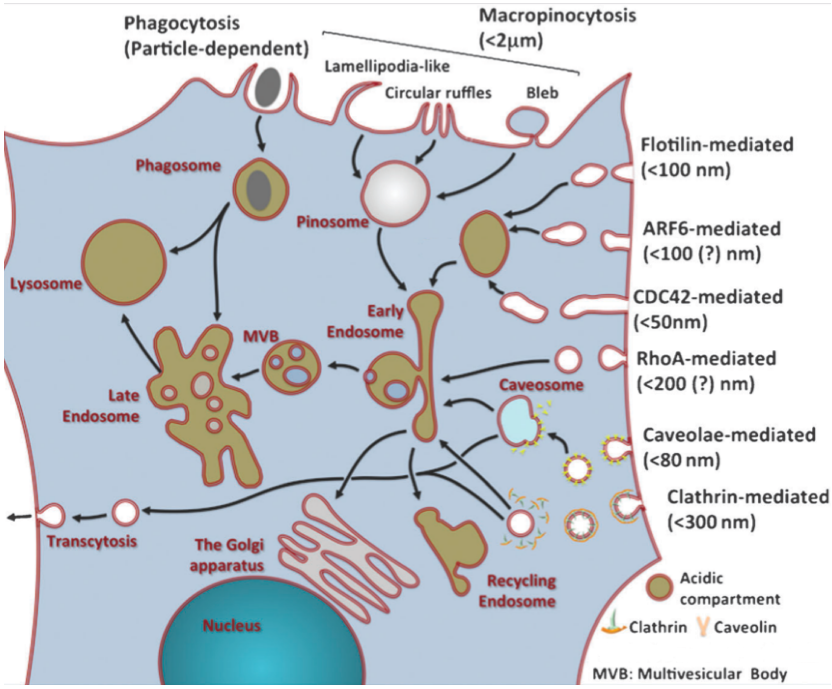

Fig. 1.1 Mechanisms of extracellular uptake by endocytosis in a typical eukaryotic cell. Adapted from Canton et al.[14]

All these mechanisms generally share four fundamental steps: (i) specific binding event at the cell surface; (ii) plasma membrane budding and pinch off; (iii) tethering of the resulting trafficking vesicle and (iv) trafficking of the vesicle to a specific sub-cellular site. While specific binding and recognition at the membrane extracellular side are highly characteristic for each pathway, it is possible to describe some common features for the other three steps. From a mechanical point

of view, for most endocytic pathways the initial membrane remodeling can be broken down in two phases: membrane invagination and subsequent pinch off of the resulting vesicle. Both are energetically expensive and need to overcome the resistance of the cell membrane to take place[15]. In general, endocytosis-induced membrane remodeling begins with the formation of functional nanoscopic domains on the membrane surface. These domains often promote local membrane deformation, and generate regions with different curvatures. Once the membrane is deformed to the point that a vesicle buds, the subsequent stage involves vesicle detachment from the plasma membrane. For most entry mechanisms, a common protein from the GTPase family regulates this process, dynamin. Dynamin assembles into a helical polymer around the constricted phospholipid neck formed by the invagination of the membrane. This irreversibly severs the endocytotic vesicle from the plasma membrane[16,17]. Following detachment from the plasma membrane, the resulting vesicle proceeds along the endocytic trafficking system. This consists of a spatiotemporal succession of steps through different sub-cellular compartments, which continuously share their content (mainly via the exchange of small vesicles[18]) while undergoing structural transformation and functional makeover (see Fig 1.2). In this trafficking scenario it is possible to roughly distinguish three main districts: early endosomes (EEs), late endosomes (LEs) and lysosomes. EEs represent the first station for most endocytic pathways and they are often located in the periphery of the cell. A pH range between 6.1 and 6.8 characterizes these compartments, where the acidification process is promoted by vacuolar adenosine triphosphatase action (protons are pumped from the cytosol into the vesicular lumen). Morphologicaly EEs appear as pleomorphic compartments that comprise cisternae regions with slender tubules (ca. 60–80 nm diameter) and large vesicles (ca. 300–400 nm diameter). The latter are multivesicular bodies with membrane invaginations either free in the lumen or in contact with the limiting membrane. The EEs are responsible for: (i) ensuring that housekeeping receptors are recycled back to the plasma membrane (directly or indirectly via recycling endosome); (ii) sorting material toward the Trans Golgi Network (TGN); and (iii) shuttling receptors and internalized materials that require downregulation/degradation to the LE. The EE structure is directly correlated to its function. Tubules regulate communication with the TGN and the recycling pathway, as well as the entry of the trafficking vesicles. Conversely, the multivesicular parts lead to the formation of multivesicular bodies (MVB), which contain factors and proteins that must be degraded in lysosomes. They are believed to be shuttled via

microtubules to LEs probably delivering their cargo by fusion[19]. MVBs rapidly reach the LE where the internal pH drops to the 5.5–4.8 range. LEs have also a pleomorphic architecture that comprises tubular and multivesicular areas. Each of these regions has a different protein and lipid composition dedicated to the sorting of internalized materials[20]. Finally, from LEs the internalized material can reach the terminal station of the endocytic degradation pathway, the lysosome. Lysosomes represent about 5% of the intracellular volume and have a distinct size and morphology including multi-lamellar and/or spiral membranous structures refereed to as membrane whorls. The luminal pH of lysosomes is maintained around 4.5 by proton-pumping vacuolar ATPases[21]. Soluble lysosomal hydrolases and integral lysosomal membrane proteins are the main regulators of lysosome function. Their combined action is responsible for the lysosome catabolic capacity[22]. Alongside its role in the endocytic pathway, lysosomes have a major function in the degradation of intracellular materials (e.g. autophagy), degradation of the extracellular matrix and initiation of apoptosis[23].

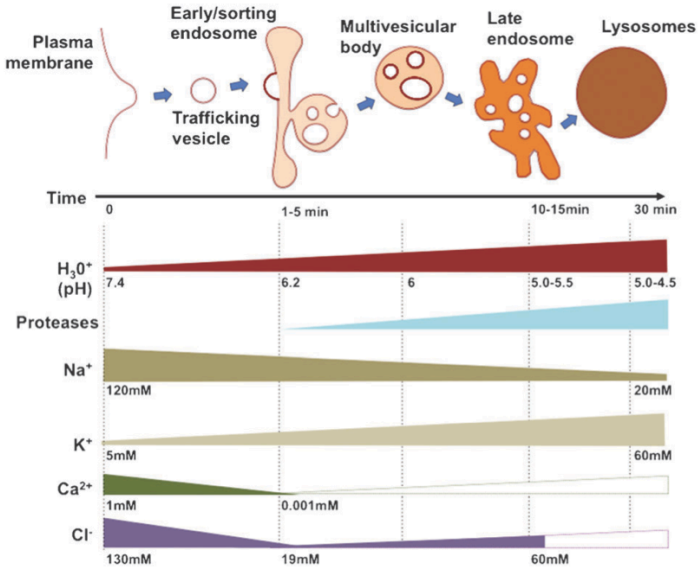

Fig. 1.2 Schematics of the different endocytic compartments. The time that the endocytosed material takes from its entry to reach each organelle is plotted alongside the organelle internal pH, protease and several ions concentrations. Taken from Canton et al.[14]

In the following sections the various endocytic pathways will be illustrated in some detail with special emphasis on the intracellular journey and destination reserved to internalized cargo-vector delivery complexes.

1.1.1 Phagocytosis

Phagocytosis commonly takes place in specialized cells called professional phagocytes[24]. In addition, other non-professional phagocytes can exhibit phagocytic characteristics under certain conditions. In fact, large particle engulfment was reported in fibroblasts[25], endothelial cells[26], and epithelial cells.[27] Phagocytes can recognize foreign bodies directly by the "eat me" signals the latter express. For cargoes that lack these signals, phagocyte recognition is dependent on particle opsonization. Through this process foreign materials are coated by the attachment of classical complement proteins and/or antibodies. Phagocytic cells then respond accordingly, depending on which proteins opsonize the particles. Phagocytosis is an actin-based internalization process triggered by the specific cell-membrane recognition of extracellular particles through the recruitment of membrane receptors. This interaction directs a cup-shaped membrane protrusion (mediated by actin polymerization) that gradually surrounds the recognized particle. The distortion of the membrane ends with the formation of an uncoated vesicle, named phagosome, with shape and size dictated by the endocytosed material (as large as 5–10 mm)[28]. Due to the fact that the large volume of internalized material requires prompt and effective processing, phagosomes usually bypass the EEs and directly fuse with lysosomes (to form mature phagolysosomes)[29] accelerating the degradative process. In phagolysosomes, the internalized material is exposed to a low-pH environment and attacked by degrading enzymes. Therefore, for efficient intracellular delivery via the phagocytic route vectors must be capable of quickly carrying their cargoes out of the phagosome to avoid phagolysosomal degradation.

1.1.2 Macropinocytosis

Macropinocytosis is defined as a transient, growth-factor-induced, actin-dependent endocytic process that leads to the internalization of fluids and membranes in large vacuoles[10]. As shown in Fig. 1.3, macropinocytosis starts with ruffling that can be non-specific and spreads over the entire cell membrane due to a global increase in actin polymerization[30]. Depending on the cell type and activation pathway, ruffles can be planar folds[31] (lamellipodia-like), circular cup-shaped extensions[32] (circular ruffles), or large plasma-membrane extrusions[31] (blebs; see Fig 1.1). These membrane protrusions can be stimulated by the activation of growth-factor receptors[30] and by a variety of particles including bacteria, apoptotic bodies, necrotic cells, and viruses[30]. These protrusions are the consequence of cytosolic actin polymerization initiated and regulated by specific GTPases, such as Rac1, ADP-ribosylation factor 6 (Arf6) and Cell-division-Control protein 42 (Cdc42)[33,34]. It is worth noting that not all membrane protrusions lead to the formation of macropinosomes. Most retreat back into the plasma membrane while few succeed in forming vacuoles filled with external fluid. Vacuoles undergo membrane fission resulting in the formation of the macropinosome[31]. The fission mechanism and vesicle closure in both lamellipodia-like and circular ruffle macropinocytosis are regulated by dynamin[35]. In contrast, bleb-associated macropynocitosis is dynamin independent[36]. Macropinosomes are larger than other endocytic vesicles, and are typically heterogeneous in size (from 0.5 to 10 mm) and shape.[31] The fate of macropinosomes differs according to the cell type. However in the majority of cells macropinosomes mature along the endocytic degradation pathway[37]. Upon endocytosis, macropinosomes acidify and acquire EE markers and/or early-endosome antigen 1(EEA-1). They then further acidify and shrink acquiring late-endosome markers and then fuse with other late endosomes or with lysosomes[37]. This fate was reported for macrophages[38], HEK293[39], COS-1 cells[40], and brain microvascular endothelial cells[41]. On the other hand, in EGF-treated A431 cells, macropinosomes have a different fate and do not fuse with the lysosomes. In this case, early macropinosomes do not seem to mature beyond the EE stage as EEA-1 mediates the homotypic fusion between macropinosomes, and finally these compartments recycle their contents to the exterior of the cell[42].

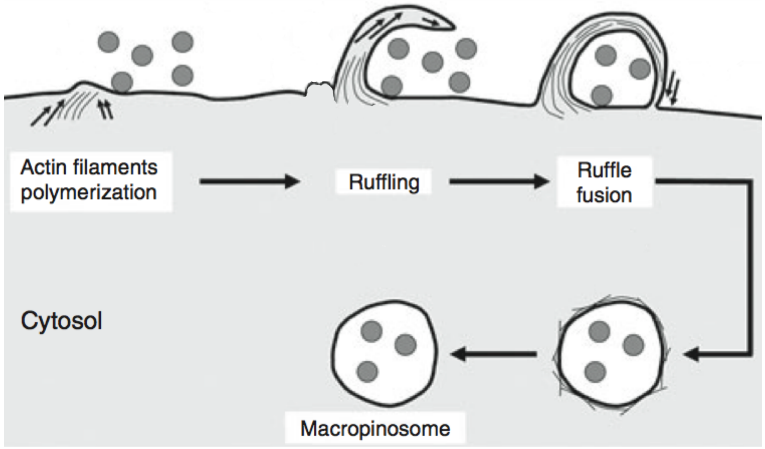

Fig. 1.3 Macropinocytosis schematic representation. Macropinocytosis starts with an increase in actin polymerization, which results in cell membrane ruffling. The planar membrane ruffles may fold and fuse with the plasma membrane to form macropinosomes. In the cytosol, the macropinosome loses the actin filaments on its surface. Adapted from El-Sayed et al.[8]

1.1.3 Clathrin-mediated pathway

Clathrin-mediated endocytosis (CME) is by far the most studied of all the endocytosis mechanisms. CME is involved in nutrient uptake[43], receptor signalling[43], as well as synaptic vesicle recycling in neurons[44]. Also, CME is the most common internalization pathway exploited by viruses[10]. The rate of membrane internalization via CME ranges between 1–5% per minute[45]. The first stage of CME involves the sorting of trans-membrane receptors that upon binding to their ligands trigger the formation of 'coated pits' on the cytosolic side of the plasma membrane. These pits originate from the assembly of several cytosolic proteins into a coating cage (with clathrin as the main unit) that stabilizes the membrane inward curvature. Clathrin has a peculiar three-legged structure, known as triskelion, resulting from the assembly of the three clathrin heavy chains, each associated with a clathrin light chain[46]. Clathrin assembly is also responsible for the formation of the vesicle neck. Here dynamin-2 polymerization constitutes a coil that constricts the neck eventually promoting the pinching off of the clathrin-coated pit into a clathrin-coated vesicle (CCV)[47]. As shown in Fig. 1.4, once the CCV is detached, the clathrin basket wears off from the receptor-loaded vesicle, leaving a naked vesicle that undergoes further

intracellular trafficking. In the cytosol, these uncoated vesicles fuse with one another and with various vesicles from other endocytic pathways to form the EE station. During EE acidification internalized cargoes are sorted. Some are recycled back to the cell exterior through recycling endosomes, while unrecycled cargoes are conveyed into the degradation pathway towards the final lysosome compartment[48].

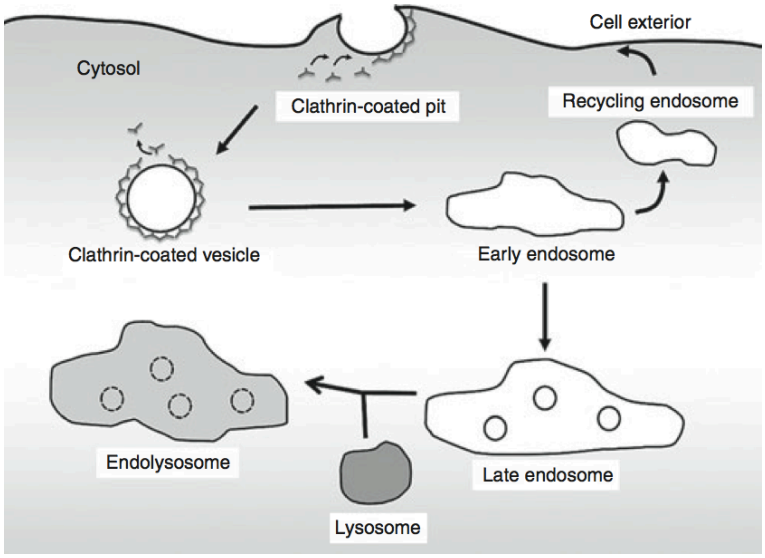

Fig. 1.4 Clathrin-mediated pathway schematic representation. Clathrin is recruited from the cytosol into the inner leaflet of the cell membrane to form the clathrin-coated pit. The pit then is pinched off, to form a CCV that then begins to lose its clathrin coat in the cytosol. This is followed by the fusion of these uncoated vesicles with each other and with various vesicles from other endocytic pathways to form an EE. At this stage the internalized cargoes are either recycled back to the cell exterior through recycling endosomes or directed to the degradation pathway. Taken from El-Sayed et al.[8]

1.1.4 Caveolin-mediated pathway

Caveolin-mediated pathway is the best-known endocytic internalization route that takes place in lipid raft domains of the plasma membrane (i. e. glycolipoprotein microdomains, which are more ordered and tightly packed than the surrounding bilayer and float freely within the membrane bilayer). These pathways,

described in Fig. 1.5, internalize plasma membrane proteins that lack cytoplasmic sequences recognizable by clathrin adaptor proteins[49]. Those mechanisms do not require the organization of a complex clathrin coat and therefore typically operate when a less selective and more rapid endocytosis is needed, as in case of receptor signaling down-regulation. Caveolae (from latin, little caves) are 50–80 nm, flask-shaped invaginations present on the surface of muscle cells, endothelial cells, fibroblasts, and adipocytes[50]. They have a striated coat on the membrane surface composed primarily of caveolin-1 (or caveolin-3 in muscle cells) and caveolin-2[51]. Caveolins are 21 kDa membrane proteins anchored to the cell membrane by a hydrophobic sequence[52] and show a high binding affinity for cholesterol in lipid rafts. In particular, Caveolin-1 (and its muscle cell analogous caveolin-3) is responsible for the structural formation of the caveolae[53], while caveolin-2 was reported to act as a scaffolding protein, forming stable hetero-oligomeric complexes with the other caveolins[54]. Finally, recent reports suggest that smaller family of proteins, cavins, may act as coat components that stabilize caveolae[55]. Based on a study of the simian virus 40 intracellular trafficking, whose uptake was thought to be limited to caveolae-dependent endocytosis, caveolae were considered to have a peculiar fate. After pinching off from the membrane (dynamin-dependent), they were believed to fuse with each other to form a mature vesicle, which was referred to as the caveosome[56]. This caveosome was reported to be a neutral vesicle, to bypass the endolysosomal pathway and transfer its cargo to the endoplasmic reticulum[56]. However, a recent revision of the caveolae process showed that what was thought to be a caveosome was instead a stage of maturing endosome in which the accumulating caveolin was awaiting degradation[57]. Authors also suggested that the term caveosome should no longer be used. It is now recognized that the fate of caveolae is cell-type dependent. When caveolar endocytosis takes place in non-endothelial cells, the cargoes are destined for the endolysosomal system[58]. On the other hand, if endocytosis takes place in endothelial cells, especially *in vivo*, the cargo may undergo transcytosis across the endothelial cell to the underlying tissue. The transcytosis of cargoes across the endothelial barrier is the most important trafficking process associated with caveolae[59].

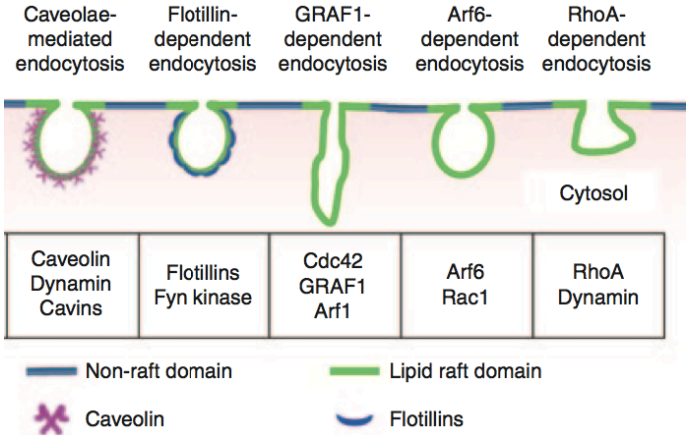

Fig 1.5 Summary of endocytic pathways that take place in lipid raft domains of the cell membrane and some of their key regulators. Caveolae-mediated endocytosis takes place in lipid rafts that are enriched in caveolin and the resulting vesicles are stabilized by cavins. Scission of the vesicles from the cell membrane takes place *via* the action of dynamin. Similarly, flotillin-dependent endocytosis results in the uptake of the cargo into vesicles enriched in flotillins. GRAF1-dependent endocytosis is mediated by the complementary role of Cdc42 with Arf1 in meditating actin polymerization. Similarly, Arf6 mediates the formation of the Arf6-dependent endocytic vesicles in addition to Rac1 which plays a role in scission of these vesicles. RhoA-dependent endocytic vesicles are formed *via* the function of RhoA and actin and vesicles formed are pinched off through the action of dynamin. Adapted from El-Sayed et al.[8]

1.1.5 Flotillin-dependent pathway

Flotillin-dependent endocytosis is an uptake mechanism similar to that involving caveolae, however, flotillin vesicles do not contain caveolin proteins and undergo a different maturation process. Vesicles in the flotillin-dependent endocytosis pathway are enriched in flotillin-1 (reggie-2) and flotillin-2 (reggie-1) proteins. The flotillin proteins were originally discovered in neurons during axon regeneration; however, they were independently recognized as markers of lipid membrane domains and renamed flotillins due to their residence in buoyant (floating)

detergent-insoluble membrane fractions[60]. Flotillin-1 and flotillin-2 are palmitoylated transmembrane proteins that acquire a hairpin structure once inserted in the plasma membrane. Flotillin-mediated endocytosis was shown to follow phosphorylation of the flotillins by Fyn kinase and to be, in general, dynamin independent[61]. Flotillin-positive vesicles co-localize with markers for LEs and lysosomes[61,62] but not with EE markers, indicating that their uptake is different from CME[63]. Many delivery vectors were shown to be internalized through flotillin-dependent endocytosis after binding to cell-surface heparan sulfate proteoglycans[64]. Following endocytosis, the complexes rapidly co-localize with late endolysosomes.

1.1.6 GRAF1-dependent pathway

The GRAF1-dependent endocytosis pathway is characterized by the formation of tubular invagination of the plasma membrane in lipid-raft-rich areas. Vesicles can be 200–600 nm long and 30–50 nm wide[65] enabling the internalization of large volumes of extracellular fluid. The invagination process is regulated by Cdc42 (for actin polymerization) and is sensitive to cholesterol depletion. The resulting pinocytic vesicles differ from macropinosomes in being Rac1-independent and from CCVs and caveolae in being dynamin-independent and not coated with clathrin or enriched in caveolin. The complementary role of Cdc42 with Arf1 in recruiting actin polymerization resembles vesicle formation in the Golgi[66]. On the other hand, the formed tubules require a coat protein to stabilize them. Lundmark *et al.*[67] reported that the protein GRAF1 associates with these vesicles and proposed it as a specific marker for this uptake pathway. They argued that the role of GRAF1 is to stabilize the tubule curvatures after formation is promoted by Arf1[68]. In fact, GRAF1 contains distinctive domains to control membrane deformation and vesicle scission. The GRAF1-dependent endocytosis pathway is estimated to be responsible for >70% of the constitutive fluid uptake in NIH 3T3 cells[69]. After formation, these vesicles become acidic and fuse to EEs from the CME pathway[70]. They are then sorted to LEs[71].

1.1.7 Arf6-dependent pathway

Arf6 is a member of the Ras-like small GTPase family of proteins that play a regulatory role in endocytosis[72]. In addition to its role in CME and macropinocytosis[73], Arf6 was implicated in a distinctive lipid raft related endocytic pathway (for which it represents a specific marker)[74]. Specifically, Blagoveshchenskaya *et al.*[75] reported that Arf6-mediated endocytosis is involved in the constitutive uptake of class I major histocompatibility complex (MHC-I) molecules. This pathway requires the activation of Arf6 and the presence of actin filaments[76], while Rac1 plays a determinant role in dynamin-independent scission of mature vesicles. The common route of Arf6-mediated vesicles is recycling back to the cell surface after fusion to sorting endosomes[76]. Arf6 inactivation is necessary for the recycling of cargoes to the plasma membrane and for fusion to the sorting endosome[77]. The overlap between Arf6-dependent endocytosis and CME is believed to be necessary for the recycling of Arf6-positive vesicles cargoes[78].

1.1.8 RhoA-dependent pathway

RhoA belongs to the Ras homolog gene family[79] and controls actin cytoskeleton dynamics. RhoA regulates actin filament rearrangement, gene expression, cell-shape determination and proliferation[80,81]. RhoA involvement in endocytosis started with the study of interleukin-2 receptor internalization[82]. RhoA-mediated endocytosis was subsequently ascribed for the control of ricin uptake[83] as well as for the entry of Baculovirus[84]. The high specificity for a limited number of cargoes makes this endocytosis pathway one of the least studied ones. RhoA-dependent endocytic vesicles are formed *via* actin rearrangement in lipid raft-rich areas of the plasma membrane. RhoA vesicles are then pinched off through the action of dynamin. It is noteworthy that the role of activated RhoA bound to GTP in mediating clathrin-independent endocytosis is contrary to its role as a negative regulator of CME[85]. After RhoA-dependent internalization, material is transferred to EE compartments and follows the maturation of the endosome to LE and endolysosome[86]. Nevertheless, interference with the common route to lysosome failed to result in the inhibition of RhoA-dependent uptake pathway, probably indicating the presence of an alternative intracellular route.

1.2 The endosomal escape issue

As described in the previous section, aside from Arf6-mediated recycling and caveolae-mediated transcytosis, most endocytic pathways ultimately converge to the lysosome where vesicle contents are degraded[87,88]. Bioactive cargoes that are intended to have a pharmacological action inside the cell must therefore escape the degradative environment of the endolysosomes. Similar to most endocytosed physiological macromolecules, therapeutic and diagnostic cargoes are often inactivated by the acidic lysosomal pH and\or hydrolyzed by lysosomal enzymes. Also, if the delivery construct is destined for a recycling pathway, efficient endosomal escape must occur before return to the plasma membrane. Therefore, for the successful design of any intracellular delivery vector, endosomal escape currently represents the main bottleneck for achieving effective cytosolic delivery[1]. Endosome gatways to the cell interior are comparable with the ones ceased by the vector at the exterior of the cell: macromolecule escape from endosomes ultimately requires passage through a lipid bilayer[6]. In this scenario the goal is to design endosomal-responsive vectors able to specifically permeabilize the EE\LE membrane and release cargoes into the cytosol. This must occur within a specific temporal window, ideally prior to the translocation to lysosomes or recycling endosomes. Various approaches were explored to promote early endosomal escape of cargoes delivery vehicles[1]. In the following sections some of the most-relevant endosomal escape mechanisms and actors will be illustrated.

1.2.1 Endosomal escape mechanisms

Several methods were tested to facilitate the early release of cargoes from the endosomal pathway into the cytosol. For example, a number of chemical agents, such as chloroquine[89], calcium[90] and sucrose[91] were employed to promote efficient cargo escape during *in vitro* application. However, the *in vivo* exploitation of these exogenous additives is limited by safety concerns. In fact, they are found to be toxic for several cell types and can trigger many side effects.[92] Therefore, in the last decades researchers have resorted to carefully-designed synthetic vectors like polymers, lipids, and peptides that can facilitate cytosolic cargo delivery by the promotion of localized endosomal membrane perturbation activity. As shown in Fig. 1.6, their activity is mostly based on three mechanisms of endosomolysis: (i) pore

formation, (ii) proton sponge, and (iii) flip-flop/fusion[1]. Pore formation is based on the binding of agents such as cationic amphiphilic peptides to the lipid bilayer leading to internal membrane tension. This effect can be sufficiently strong to create pores in the lipid membrane that in turn can lead to the release of endosomal contents[93]. Conversely, the proton sponge effect is mediated by agents such as poly(ethylene imine) with a high buffering capacity and flexibility to swell when protonated[94]. Protonation induces an extensive inflow of ions and water into the endosomal environment, which subsequently leads to rupture of the endosomal membrane by osmolysis and release of the entrapped components. In general, vectors containing tertiary amine groups were shown to accumulate in endosomes and become detergents upon protonation resulting in membrane disruption[95]. Finally, the flip-flop/fusion mechanism exploitis vectors (like the so called 'helper lipids'[96] and fusogenic peptides[97]) that take advantage of phospholipid flipping and bilayer fusion. These are processes that under normal conditions are necessary to maintain lipid membrane asymmetry (catalyzed by flippase enzyme[98]) and promoting vesicle maturation, respectively. In this case the fusion vector exploits the interaction with the phospholipids to deform the bilayer and create an exit-route for its cargo.

In all cases described so far, specific environmental changes during endosomal trafficking, such as pH lowering, proteolytic enzymes activation, or membrane composition modification are necessary to trigger endosomal escape by affecting the vector and/or the lipid bilayer characteristics[99]. This local activation is necessary to avoid toxic side effects when the administered vector is located on the extracellular side of the plasma membrane during the uptake process. In addition, when selecting an endosomal bioresponsive vector it should be taken into account that, regardless of the endolysosomal release mechanism, the poor serum stability[100,101] and collateral toxicity[102,103] of fully synthetic polymers and lipids limit their use *in vitro* and *in vivo*. Nonetheless, encouraging results were obtained (both in terms of delivery efficiency and toxicity level) with endosomal-membrane perturbing agents based on viral-protein-derived, rational-designed or antimicrobial amino acid sequences[104-106].

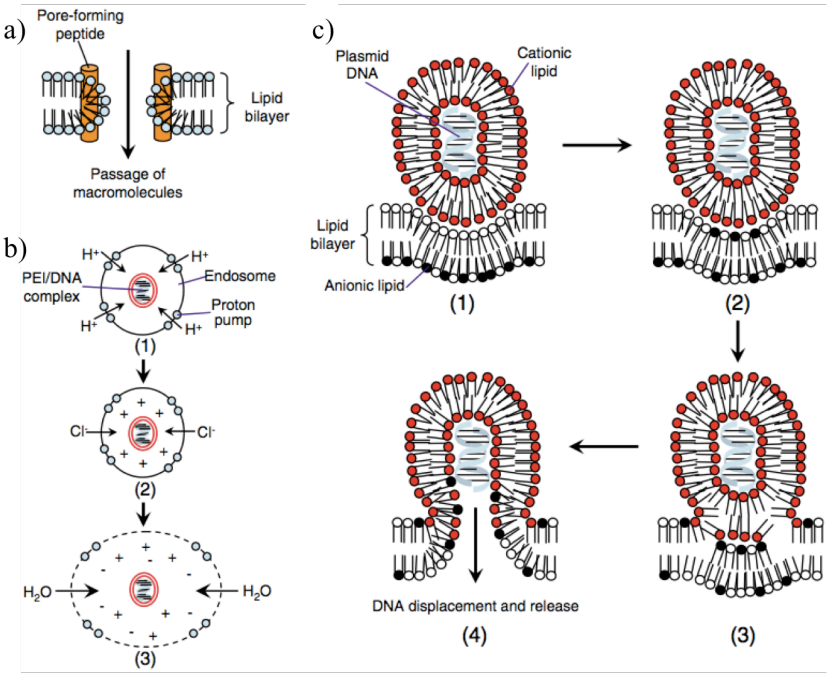

Fig. 1.6 Emblematic examples of endosomolysis mechanisms. (**a**) Pore formation. Pore forming peptides induce bending of the membrane and contiguity of the bilayer leaflets, thus opening a pore in the membrane and facilitating release of endosomal contents. (**b**) Proton sponge. The polyplex exacerbates proton accumulation in the endosome (1), inducing passive chloride influx (2), and causing osmotic swelling and endosomal rupture (3). (**c**) Flip-flop/Fusion. The lipoplex becomes endocytosed (1), and destabilizes the membrane, inducing flipping of anionic lipids from the cytoplasm to face the endosomal lumen (2). The anionic lipids form charge neutral ion pairs with cationic lipids of the complex (3), thus displacing the DNA and releasing it into the cytoplasm (4). Taken from Medina-Kauwe et al.[1]

In the following sections some examples of peptidic agents that were shown to enhance endosomal escape following delivery are described. The sequence and endosomal-escape mechanism for each system are summarized in Tab. 1.1.

1.2.2 Viral-protein-derived peptides

A number of small viral protein domains were identified that favor the endosomal escape of the entire viral capsule (or part of it) following uptake. In many cases, the isolated sequence is able to exert its function when fused to a paylod of interest.

The haemagglutinin 2 (HA2) protein subunit from the human influenza virus was one of the first reported examples of a virus-derived agent capable of causing membrane fusion/destabilization activity by itself. Human influenza virus is an enveloped virus that utilizes fusion to the endosomal membrane for delivery of its genetic material into the cytoplasm of infected cells. The virus envelope is composed of two major glycoproteins: hemagglutinin (HA) and neuraminidase. HA in turn comprises two subunits. In particular, the HA2 subunit possesses a fusion domain at its N terminus that forms an α-helix structure capable of insertion into endosomal membranes, thus initiating the fusion process. The acidic pH of endosomes induces a conformational change in the hemagglutinin protein and exposes the α-helix structure in the HA2 subunit. This in turn results in insertion of the α-helix into the endosomal membrane and leads to fusion between the virus envelope and the endosomal membrane. As a result the viral nucleocapsid is released into the cytoplasm of the infected cell[107,108]. Utilization of this fusogenic segment of HA2 protein to enhance the endosomal escape of arginine-rich peptide-linked cargo was first reported by Wadia et al.[105]. In this report, the Tat-peptide linked to a HA2 peptide was co-incubated with Tat-Cre protein. In the absence of Tat-HA2 peptide, the majority of the Tat-Cre fusion protein was found trapped in macropinosomes up to 24 h after transduction. Improved endosomal escape, quantified by Cre recombination, was observed when Tat-HA2 was co-incubated with Tat-Cre. According to the authors, however, more than 99% of the Tat fusion protein remained trapped in macropinosomes even after the fusogenic peptide Tat-HA2 treatment[109].

In search of more efficient derivatives of the influenza HA2 peptide, Plank et al.[110] introduced the INF7 peptide as a pH-sensitive, more potent membrane-destabilizing peptide. In this peptide, two glutamic acid moieties were added to the HA-2 structure in order to extend the α-helix conformation and increase pH sensitivity. Recent studies confirmed that INF7 has a slightly more pronounced pH sensitivity as compared to the parent HA2 peptide[111]. It is also worth mentioning that other relevant derivatives of influenza HA2 peptide (H5WYG[112,113], E5CA[114-116]

and ppTG1[117,118]) were investigated and engineered with the aim of improving the fusogenic properties and triggering selectivity of this moiety.

Another example of a virus-derived fusogenic peptide is the gp41 transmembrane peptide of the Env glycoprotein from HIV. Similarly to HA2, it acts as a fusogenic agent due to its α-helical conformation. This peptide was used as a hydrophobic domain in combination with a hydrophilic domain derived from the nuclear localization sequence of SV40 large TY antigen (MPG peptide). The gp41 fusion mechanism is not well understood although pore formation was proposed[119,120]. The gp41-derived peptide demonstrated significant lytic activity[121], however, and its fusogenic properties must be carefully tuned to reduce cellular totoxicity.

1.2.3 Synthetic peptides

Several endosomolytic peptides with specific sequences and length were rationally designed to enhance cytosolic delivery by exploiting the natural environmental changes occurring along the various endosomal pathways.

Lundeberg et al.[122] started from the amino acid sequence of Penetratin, one of the first discovered peptide vectors. Their report was the first to demonstrate the rational modification of an existing peptide vector in order to achieve increased endosomal escape and hence improved biological activity. Based on the fact that several reports showed an increased biological effect of penetratin by enhanced endosomolysis action through the linking or co-incubation with endosomolytic agents[105,123], Lundeberg et al. developed a penetratin analog with some amino acids replaced by histidines, under the supposition that upon protonation the peptide would change its secondary structure and form an α-helix with the ability to penetrate the endosomal membrane. The designed peptide, EB1, was also N-terminally extended with six amino acids in order to give it the desired length. At low molar ratios EB1 showed superior delivery properties compared with penetratin. Unfortunately, although EB1 yielded a better biological response than addition of the fusion peptide HA2 to penetratin, it also resulted in a higher degree of cytotoxicity.

The N-terminal sequence of the influenza virus haemagglutinin subunit HA2 was used as a model to construct two new peptides for endosomal escape. One of these is KALA, a cationic amphipathic peptide. KALA undergoes a conformational change from pH 7.5 to 5.0, that leads to a destabilization of endosomal membranes,

similar to HA2, as reported in several studies[124-127]. GALA is another synthetic amphipathic peptide with a substitution of glycine for a specific glutamic acid from a mutant sequence of influenza virus. GALA also undergoes a pH-dependent conformational change resulting in the formation of a helical structure that induces the content leakage from large unilamellar phosphatidylcholine vesicles[128]. The mechanism of membrane perturbation induced by these amphipathic α-helical peptides is not quite understood yet and available information are based only on work with synthetic lipid vesicles[129].

LAH4 and its derivatives constitute another class of peptides that exhibit efficient gene-transfer activity[130,131]. Peptides of the LAH4 family are synthetic, cationic, amphipathic peptides containing a variable number of histidine and hydrophobic amino acid residues (mainly alanines and leucines). *In vitro* transfection experiments indicate that peptides with four to five histidine residues in the central region of the sequence achieve high transfection efficiency comparable to polyethylenimine (PEI) action. Furthermore, LAH4 peptides undergo a pH-dependent conformational change from a transmembrane orientation at neutral pH to an in-plane orientation at low pH. The pH at which the conformation transition takes place is crucial and significantly impacts transfection efficiency[130,132,133]. Based on these observations it was proposed that at neutral pH LAH4 adopts a transmembrane orientation without disrupting membrane integrity if administered below a certain concentration threshold[134].

Finally Andaloussi and co-workers[135] hypothesized that introduction of a potent proton-accepting moiety, i.e. a novel chloroquine analog[136], into a stearylated peptide vector (i.e. Transportan10, TP10) would facilitate escape from acidic endosomal compartments by osmotic swelling and by delaying endosomal acidification. TP10 was chosen since it was previously used successfully both *in vitro* and *in vivo*[137] for nucleic acid delivery. The designed vector, PepFect 6, formed stable peptide/siRNA nanoparticles and rapidly promoted endosomal escape. It was shown to lead to a robust RNAi response, with minimal associated transcriptomic or proteomic changes. However, the *in vivo* gene silencing results were not as significant when compared to standard lipid-based delivery systems[135].

In all aforementioned cases, the endosomal perturbing-activity triggered by the peptide is strictly dependent on the environmental conditions of the endosomal pathways encountered by the cargo-vector complex, namely: pH, enzymatic set, or

membrane composition[138]. Moreover, escape from the endocytic vesicle can also be dependent on the nature of the primary endocytic vesicle or the speed of transport to the endolysosomal compartments (both factors are dictated by the uptake mechanism). These restrictions represent important considerations for the design of peptide delivery vectors due to the fact that the specific endosomal pathway undertaken by the vector is dependent on both the attached cargo and specific target-cell population. Cargo characteristics, such as size, surface charge, shape, and concentration[139] not only influence vector-uptake efficiency but also the predominance of a specific internalization pathway. In addition, vector trafficking may be cell-type specific and dependent on the predominance of a particular endocytosis pathway in that cell[59]. The internal environment of EEs and LEs may also be dependent on cell type. This can impact delivery efficiency. In these scenarios, a membrane-perturbing agent must be active independent of its endosomal-entry route to be efficiently employed in different drug-delivery strategies for a wide range of cell targets.

1.2.4 α-helical antimicrobic peptide: an unconventional tool to overcome endosomal entrapment

In the last decade, several research groups investigated the antimicrobic peptides (AMPs) family as a new source for the development of delivery vectors able to overcome the endosomal entrapment bottleneck thanks to their characteristic concentration-dependent membrane-perturbing properties[140]. This is interesting due to the fact that during endocytosis the vector local concentration and its ratio compared to the membrane surface greatly increase from their original value in the extracellular medium independently of the specific pathway[141].

In particular, much work focused on the class of α-helical cationic peptides, which constitutes an essential part of the "innate" first line of defense against bacterial infections[140]. α-helical AMPs were exploited as delivery tools owing to their low immunogenity impact and physicochemical properties: AMPs are tipically disordered in aqueous solution but assume an α-helical secondary structure in hydrophobic environments (see Fig. 1.7). The latter conformation is responsible for their concentration-dependent membrane-disrupting properties[140]. Specifically, at low peptide/lipid ratios peptides are bound parallel to the lipid bilayer[142]; however

as the ratio increases, peptides preferentially align perpendicularly to the membrane and finally insert into the bilayer and perturb its stability. The exact mechanism of membrane permeabilization is still debated[140]. These properties were exploited in preliminary drug-delivery applications of cathelin-associated human LL-37[143,144] and bee-venom Melittin[145] antimicrobial peptides by themselves or as a part of a multi-component delivery system. Concerning Melittin, much work was devoted to the reduction of its intrinsic hemolytic activity by focused sequence mutations[146,147]. In the following sections physico-chemical properties and reported applications shall be briefly illustrated for the two AMPs.

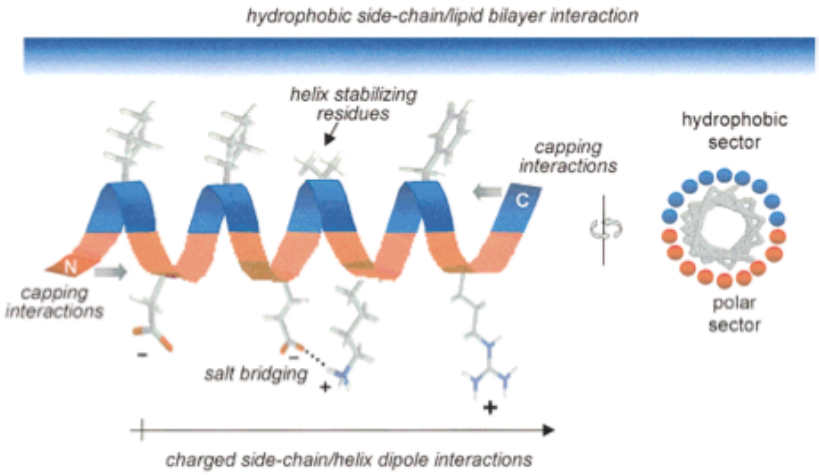

Fig. 1.7 AMP amphipatic α-helical structure. In blue it is highlighted the hydrophobic sector of the helix, while the polar side is depicted in orange. Taken from Tossi et al.[148]

- **The human cathelin-associated antimicrobial peptide LL-37**

LL-37 represents the only AMP identified in the human cathelicidin family. It is a 37-residue peptide that carries 16 charged residues in total. At neutral pH, its net charge is +6[149]. LL-37 is a proteolytic cleavage product corresponding to the C-terminus of its precursor human cationic antibacterial protein of 18 kDa (hCAP18)[150-152]. It displays antimicrobial activity against both Gram-positive and Gram-negative bacteria at a minimum inhibitory concentration (MIC) below the 10 μg/ml range[153]. In addition, LL-37 can interact with both zwitterionic and negatively charged lipid vesicles, adopting predominantly α-helical structures[149,154]. This in turn can lead to membrane disruption and subsequent content leakage via a detergent-like carpet mechanism[149,155].

The delivery properties of LL-37 were mainly tested through non-covalent conjugation with short oligonucleotides[143] or pDNA[144]. Zhang et al. demonstrated intracellular delivery of short oligonucleotides to COS-7 cells with no associated cytotoxicity at sub-micromolar concentration[143]. Concomitantly, Sandgren et al. demonstrated efficient LL-37-mediated delivery of pDNA into CHO-K1 cells. In these reports it was claimed that LL-37 endosomal membrane-perturbing activity[144] is accountable for oligonucleotide nuclear delivery. Unfortunately, a critical analysis of the underlying membrane-perturbing mechanism inside endosomal vesicles was not provided. Moreover the more widespread use of LL-37 as a delivery vector is hampered by its intrinsic hemolytic activity (at micromolar concentration), and its long amino acid sequence (leading to a low-yield, expensive chemical synthesis).

- **The bee venom antimicrobial peptide Melittin**

Mellitin is a 26-residue antimicrobial peptide found in the venom of the honey bee Apis mellifera. Mellitin contains distinct hydrophilic and hydrophobic domains at its termini with four cationic amino acids sequestered near the C-terminus. Melittin displays strong, broad-spectrum antimicrobial activity but is also highly hemolytic[146,147]. In solution Melittin undergoes a concentration-dependent equilibrium between a random-coil monomer and a predominantly α-helical tetramer[156]. A number of studies indicate that in the presence of bilayers Mellitin forms N-terminal and C-terminal α-helices separated by a flexible hinge (reviewed in[157,158]). At high lipid:peptide ratios (e.g., >200:1) membrane-bound Melittin is

monomeric with its helical axis parallel to the membrane surface[157,158], and each of its lysine residues is exposed to the aqueous phase[159]. As the concentration of membrane-bound Melittin is increased, the peptide undergoes a dynamic reorientation and eventually produces a complete destruction (micellization) of the membrane bilayer[157,158].

Melittin is the most exploited AMP for drug-delivery applications. Early attempts using unmodified Melittin as a delivery agent were reported by Legendre et al.[145,160], but showed rather unsatisfactory results because of the fast partitioning of Melittin into cell membranes, with concomitant high toxicity. Two main strategies were introduced to postpone Melittin membrane-perturbing activity (e.g. at the level of endosomes): (i) the amines of Melittin were modified with dimethylmaleic anhydride (DMMAn), which minimizes lytic activity at the extracellular neutral pH; then, upon endosomal acidification, the DMMAn protecting groups are cleaved and the lytic activity is restored[161,162]; (ii) Melittin original sequence was altered by replacing or subtracting some key amino acid residues. Boeckle et al. substitued neutral glutamines (Gln_{25} and Gln_{26}) with negatively-charged (at neutral pH) glutamic acid residues (CMA-3 peptide) within Melittin positively-charged domains, which are important for its lytic activity. As a consequence, glutamic acid residues become fully protonated only at acidic pH values (i.e. inside endosomes), restoring Melittin original charge balance and lytic activity in a controlled manner[163]. Moreover, Tan Y-X et al. synthetized a Melittin truncated version (MT-20) consisting of 1-20 residues, which preserves a α-helical structure. This Melittin truncated analog showed lower hemolytic activity than Melittin itself under physiological conditions, but higher lytic activity at acidic pH[164]. All the strategies presented above were useful in reducing Melittin toxicity, but, at the same time, their performance was related on specific environmental conditions within the endosomal vesicles, thus narrowing their drug-delivery application range.

Despite its intrinsic hemolytic properties, Melittin (with its concentration-dependent membrane-perturbing activity) remains an interesting prototype for further development of a widely effective endosomal-perturbing agents. In my research I investigated a new strategy to suppress Mellitin cytoxicity, while at the same time focus its lytic activity to the endosomal compartments without relying on any environment-associated trigger. To accomplish this task, I exploited a Melittin-derived AMP (specifically constructed to reduce its hemolytic activity) in

conjugation with an arginine-rich short peptide introduced to promote the AMP membrane-perturbing activity within endosomal compartments.

Endosomolytic peptide	Primary sequence	Endosomal escape mechanism	Main Reference
Virus-derived			
HA2	GLFGAIAGFIEGGWTGMIDG WYG	Fusion	105
INF7	GLFEAIEGFIENGWEG MIDGWYG	Fusion	110
H5WYG	GLFHAIAHFIHGGWHGLIHGWYG	Fusion	112
E5CA	GLFEAIAEFIEGGWEGLIEGCA	Fusion	114
ppTG1	GLFKALLKLLKSLWKLLLKA	Fusion	117
MPG	GALFLGFLGAAGSTMGAWS QPKKKRKV	Pore/Fusion	119
Synthetic			
EB1	LIRLWSHLIHIWFQNRRLKW KKK	Fusion	122
KALA	WEAKLAKALAKALAKHLAKALAKALKACEA	Fusion	124
GALA	WEAALAEALAEALAEHLAEALAEALEALAA	Fusion	128
LAH4	KKALLALALHHLAHLALHLALALKKA	Unclear	130
PepFect6	Stearyl-AGYLLGK(K_3QN_4)INLKALAALAKKIL	Proton sponge	135
AMP-derived			
LL-37	LLGDFFRKSKEKIGKEFKRIVQRIKDFLRNLVP RTES	Unclear	143
Melittin	GIGAVLKVLTTGLPALISWIKRKRQQ	Pore	145
DMMAn-Melittin	GIGAVLK(DMMA)VLTTGLPALISWIK(DMMA) RK(DMMA)RQQ	Pore	161
CMA-3	GIGAVLKVLTTGLPALISWIKRKREEC	Pore	163
MT-20	GIGAVLKVLTTGLPALISWI	Pore	164

Tab. 1.1 Sequences and endosomal escape mechanisms of selected endosomolytic peptides that are being investigated for nucleic acid and protein delivery.

1.3 CM_{18}-Tat_{11}: a chimera peptide exploiting cell-penetrating peptides and AMPs properties

As stated in the previous section, AMP literature was screened looking for a peptidic sequence able to maintain Melittin membrane-perturbing skills, while silencing its undesired hemolytic activity. In this perspective, it is worth mentioning that a group of short hybrid peptides containing sequences from Cecropin A and Melittin (CM series) peptides appear very promising. These chimeric constructs are among the smallest and most effective AMP-derived peptides with membrane-perturbing ability[142]. A typical CM hybrid is constructed from a combination of the N-terminal hydrophilic domain of Cecropin with the N-terminal hydrophobic domain of Mellitin, or vice versa. Initial studies examined peptides containing from 18 to 37 amino acid residues, with net charges of +5 to +7[147,165]. Most constructs displayed antibacterial activity comparable to full-length Cecropins but, interestingly, lacked the hemolytic properties associated with Mellitin. Those studies were followed by a further reduction in size, with the identification of several active constructs having only around 15 amino acid residues[146]. These short peptides contain the first 7–8 residues of Cecropin A with various combinations of mostly hydrophobic amino acid residues from the N-terminus of Mellitin (see Fig 1.8). Lethal concentrations against a panel of bacteria ranged from 0.1 to 15 μM, while hemolytic concentrations were higher[146].

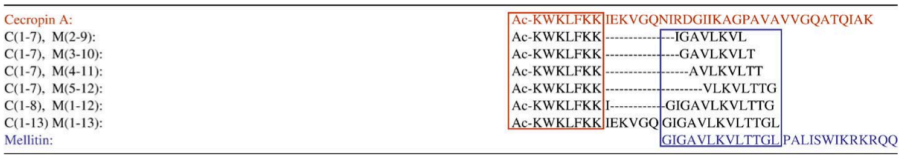

Fig. 1.8 Cecropin-A/Melittin sequences combinations. The Cecropin-Mellitin hybrids incorporate the cationic N-terminal domain of Cecropin A (red box) and mostly hydrophobic amino acid residues from the N-terminal of Mellitin (blue box). Taken from Sato et al.[142]

CM hybrids, like their parent peptides, are members of the linear, amphipathic α-helical class of AMPs (described in the previous section). They adopt a random coil configuration in aqueous solution, and transition to an α-helical secondary structure in the presence of lipid bilayers or helix-promoting organic solvents[146]. Upon folding, CM hybrids are highly amphipathic, showing an almost ideal distribution of polar and non-polar amino acid residues along the opposite sides of their α-helical secondary structure (see CM_{15} representative case in the helical wheel display in Fig. 1.9). This configuration is similar to full-length Cecropins, where along the helical structure a cationic N-terminal domain and a predominantly hydrophobic C-terminal domain can be identified.

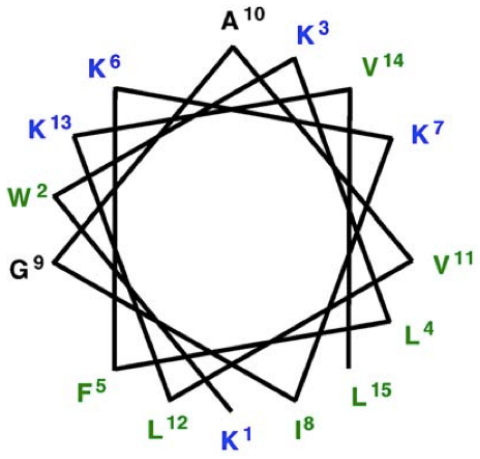

Fig. 1.9 Helical wheel display of the cecropin-mellitin hybrid, CM_{15}. The polar (in blue) and non-polar (in green) residues side chains are mostly sequestered on opposite faces of the helix. Taken from Sato et al.[142]

Several studies showed that CM hybrids[166] efficiently disrupt bacterial outer- and inner-membranes permeability. Although the mechanisms involved in perturbing the outer membrane remain poorly defined at a molecular level, most studies have focused on the events associated with binding to and disruption of the inner membrane. This may occur through a detergent-like "carpet" mechanism[167-169], or the formation of discrete pores that dissipate ion gradients[170-172].

CM peptides membrane-perturbing skills and associated low cytotoxicity prompted us to consider them as endosomal membrane-perturbing agents. However, the application of such AMP-derived sequences *per se* for drug-delivery purposes is hindered thus far by their rather low affinity for the eukaryotic outer leaflet, compared to the prokaryotic one[173]. In fact, although the weak interaction of CM peptides with eukaryotic plasma membranes limits their hemolytic action, it also strongly impairs their endosomal uptake, compromising their concentration-dependent membrane activity in endosomal compartments. To overcome this limitation, here we complemented the membrane-perturbing ability of a CM sequence with the rapid and effective uptake in eukaryotic cells guaranteed by a classical cell-penetrating peptide (CPP).

CPPs are an important class of non-viral delivery vectors, based on the discovery that peptidic sequences extracted from a number of naturally occuring proteins are able to enter cells by themselves through direct interaction with the plasma membrane. During the past two decades a large number of peptides were identified that can lead to the cellular import of cargo molecules[174-176]. Today there are more than one hundred known CPPs that can be exploited as delivery vectors for different cargoes (from small molecules such as chemotherapeutic drugs to macromolecules such as pDNAs and proteins). CPPs are characterized by a short sequence, usually less than 30 amino acids in length, and by the presence of numerous basic residues, which provides a net positive charge at physiological pH[177]. It is worth mentioning that, contrary to other delivery vectors, CPPs are easy to handle, have low toxicity, and are being clinically evaluated[177]

Among the many CPPs present in litterature, here we focused focused on an arginine-rich peptide, Tat_{11}, in line with the long-lasting research activity conducted at NEST laboratory on its delivery properties[178-180]. Tat_{11} development has its origin on the observation published by Frankel and Pabo that the human-immunodeficiency virus transactivator-of-transcription (HIV-Tat) protein can penetrate cells and activate HIV-1-specific genes[181]. This basic HIV-Tat-derived peptide (amino acid residues 47–57, YGRKKRRQRRR, charged residues underlined)[182] gained a great deal of attention as a delivery tool for macromolecules[139]. In essence, the transmembrane activity of Tat_{11} peptide was largely attributed to the high density of guanidine groups, whereas the remaining structural elements were found to play a minor or no role[139,183]. Despite the original controversy surrounding the uptake mechanism it is now widely accepted that the

Tat peptide is internalized mainly via endocytosis when administered at low μM concentrations to the cells in culture[184]. A large number of observations support the idea that macropinocytosis could be the dominant Tat_{11}-driven uptake pathway[185], but additional reports suggest clathrin-mediated endocytosis and caveolin-mediated endocytosis as alternative endocytic pathways[186,187]. Overall, the lack of complete inhibition by selective drugs or complete co-localization with known markers consistently suggests a multiplicity of entry pathways for this basic peptide[188]. It must be kept in mind that Tat_{11} peptide can adhere to any negatively charged molecule on the cell surface due to its high positive charge and presumably enter a cell through any or multiple types of endocytic vesicles. A cells plasma membrane turnover continues constitutively at an estimated rate of ~2-5%/min[189,190], meaning 100% of the cells surface is internalized nonspecifically in less than an hour, notwithstanding the faster receptor-mediated or stimulated route of uptake. In all cases, although characterized by a strong endocytic uptake, the internalized Tat_{11} peptide (either alone or linked to cargoes) does not escape endocytic vesicles. Endosomal escape is believed to be the main bottleneck for the efficient intracellular delivery of functional macromolecules by the Tat_{11} peptide. Several studies showed that Tat_{11} peptide linked to quantum dots[191], oligonucleotides[192], or proteins[193] remains trapped in endocytic vesicles after uptake, unless an endosomal escape device is included in the system[194].

Based on the advantages and drawbacks of CM and Tat_{11} peptides described in this chapter, I envisioned the possibility to fuse the two sequences in order to obtain a new drug-delivery vector, able to overcome the intrinsic limitations of the individual modules but preserve their specific skills. In the aim of this work, the chimeric carrier should be able to perform a strong but temporary (therefore not toxic) interaction with a cells plasma membrane, followed by massive endocytic uptake (thanks to Tat_{11} activity). Once trapped in high doses inside the endosomal lumen, the CM moiety should be able to reach its active membrane-perturbing concentration and promptly disrupt the membrane bilayer, thus triggering the payload release into the intracellular lumen. In the next chapters, I shall illustrate the steps through which I implemented this idea.

Chapter

2

CM_{18}-Tat_{11} functional design and cargo-delivery applications

As stated in the previous Chapter, endocytosis represents a primary candidate for drug-delivery strategies. Escape from an endocytic vesicle compartment, which isolates its content from the cytoplasm, is a necessary step for successful delivery with this approach. Indeed this step is at present a crucial obstacle for the exploitation of CPP-mediated delivery of macromolecules in therapeutic and/or diagnostic applications. In fact, even if it can drive the cellular uptake of a vast range of non-permeant molecules (e.g. proteins, nucleic acids, etc.), CPP-driven endocytosis does not usually lead to a satisfactory cytosolic concentration of the cargo-molecule. The latter instead is eventually degraded in the lysosomal compartment. To tackle this issue, here I investigated the combination of the well-known CPP uptake property of the arginine-rich Tat_{11} motif with the membrane-disruptive (concentration-dependent) ability of a linear cationic α-helical AMP, extrapolated from the recent developed series of peptides, defined as CM (Cecropin A and Melittin hybrids)[142]. Specifically we chose to exploit the CM_{18} sequence (KWKLFKKIGAVLKVLTTG, residues 1–7 of Cecropin-A and residues 2–12 of Melittin, C(1–7)M(2–12)). This peptide was designed on the basis of an extensively characterized CM peptide, CM_{15} (C(1–7)M(2–9)), which received particular

attention in reason of its broad-spectrum antimicrobial efficacy. Interestingly, decreasing CM_{15} length even by one residue only to give the 14-mer, (C(1−7)M(2−8)), or altering its original sequence (even through a single amino acid substitution) markedly reduce its antimicrobial activity[170]. This activity reduction is produced by the alteration of its amphipatic structure, which present an ideal distribution of polar and non-polar side chains sequestered on opposite faces of an α-helix that spans all CM_{15} sequence. Membrane bilayer interaction, insertion and perturbation processes are all dependent on the α-helical structure. In this scenario, it could be speculated that the direct fusion to the highly-charged Tat_{11} sequence would lead, in light of the proximity of the arginine residues to the terminal twist of the α-helix, to the alteration of CM_{15} original secondary structure or anyway to the perturbation of its interplay with the membrane. Taking the cue from the fact that adding an additional residue to CM_{15} ((C(1−7)M(2−8), a threonine residue from the original Melittin sequence) only slightly enhanced its activity[170] (due to its weak involvement in the helix formation), it was decided to extend of three amino acids, namely TTG from Melittin peptide, CM_{15} sequence. This way allows to isolate its original secondary structure from the perturbation of Tat_{11} positive charges. So the CM_{18}-Tat_{11} chimera vector should preserve a marked α-helical structure on its AMP moiety and at the same time be suitable for high-yield solid-phase synthesis, due to a final chain length within thirty amino acids.

In this Chapter the physico-chemical characterization of chimeric CM_{18}-Tat_{11} peptide is presented. First of all, it is demonstrated that addition of the Tat_{11} module neither affects the typical α-helical secondary structure of CM_{18} nor its membrane-disrupting ability. Secondly, it is verified that the Tat_{11} module continues to ensure rapid and effective translocation from the extracellular medium into endocytic vesicles following interactions with membrane proteoglycans, even in conjugation with the AMP moiety. These two conditions represent essential requisites for the efficient application of the chimera peptide for drug-delivery tasks.

We shall show that when administered to cells at sub-micromolar concentration, CM_{18}-Tat_{11} is efficiently taken up by the cell and subsequently promotes membrane destabilization of endocytic vesicles. Indeed the chimeric peptide effectively enhances the escape and subsequent intracellular localization of a vast range of co-localized membrane-impermeable molecules, i.e. Tat_{11}-Enhanced Green Fluorescent Protein (EGFP), Calcein, and different-size dextrans, with no detectable cytotoxicity.

2.1 Characterization of CM_{18}-Tat_{11} structure and membrane interaction

2.1.1 CM_{18}-Tat_{11} primary and secondary structure study

As shown in Fig. 2.1a, the synthesis of CM_{18}-Tat_{11} vector was realized by the direct fusion of CM_{18} peptide sequence to the arginine-rich motif of Tat_{11}. The two isolated components (CM_{18} and Tat_{11}) were also produced and used as controls. An additional C-terminal cysteine was added to all peptides to permit selective labeling with the atto-633 fluorophore (for the description of all the experimental procedures employed hereafter see App. B). The purported AMP activity of the CM_{18} module relies on its characteristic secondary structure, as demonstrated by others for similar CM peptides[195]. In order to investigate whether the addition of the Tat_{11} moiety affected CM_{18} ability to form α-helical structures, the peptide conformation was measured by circular dichroism (CD) analysis. The CM_{18}-Tat_{11} CD-spectrum in aqueous solution (phosphate buffer, PBS) shows a high degree of random-coil conformation (Fig. 2.1b, red line). By contrast, in the presence of 50% trifluoroethanol (TFE), added for mimic the membrane hydrophobic environment, the CD spectrum is characterized by a minimum at 205 nm, a pronounced shoulder at 221 nm, and a maximum at 190 nm (Fig. 2.1c, red line), the typical signatures of the α-helical conformation. The same structural properties emerged from the CD analysis of the isolated CM_{18} peptide (Figs. 2.1b,c black lines). On the contrary, isolated Tat_{11} adopts an unstructured or extended conformation in both hydrophilic and hydrophobic conditions. This can be deduced from its flat spectrum with only a pronounced minimum centered at 200 nm (Figs. 2.1b,c, gray lines). The similarity between CM_{18}-Tat_{11} and CM_{18} CD spectra demonstrates that the typical α-helical structure of the AMP module is not biased towards the random coil conformation by the presence of the unstructured and highly charged Tat_{11} moiety. Rather, in hydrophobic medium, the CM_{18}-Tat_{11} chimera shows a similar per-residue degree of helical formation.

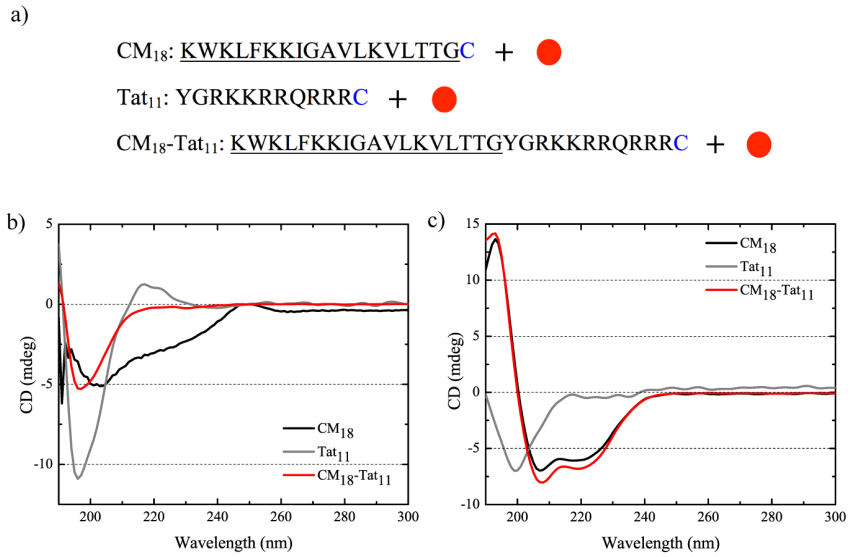

Fig. 2.1 Peptides sequences and CD spectra. (**a**) Single-letter amminoacid code sequences of CM_{18}, Tat_{11} and CM_{18}-Tat_{11} peptides. Red circles: atto-633 fluorophore. (**b**) CD spectra of all peptides in PBS (pH 7.4) at a concentration of about 0.1 mM. The spectra are normalized per number of residues. (**c**) CD spectra in 50:50 TFE:PBS solution.

In order to confirm the structural data from CD analysis, a molecular dynamics (MD) investigation of CM_{18}-Tat_{11} peptide structure in water and TFE/water mixture was carried out. MD simulations confirmed the presence of helix formation in the TFE/water mixture at room temperature (Fig. 2.2, inset), in agreement with CD data and allowed to locate the specific peptide regions participating in secondary-structure formation. The helical secondary structure spans the entire CM_{18} part (a.a. 2-18) of the chimera and partially extends to the Tat_{11} portion (a.a. 18-21). The α-helical portion closely matches the NMR structure of CM_{15} peptide[196]. It is worth noting that in the above-mentioned peptide region folding events are clearly observed during CM_{18}-Tat_{11} MD trajectories in the TFE/water mixture, while the rest of the Tat_{11} section is kept unstructured at room temperature in both media (see selected snapshots in Fig. 2.2).

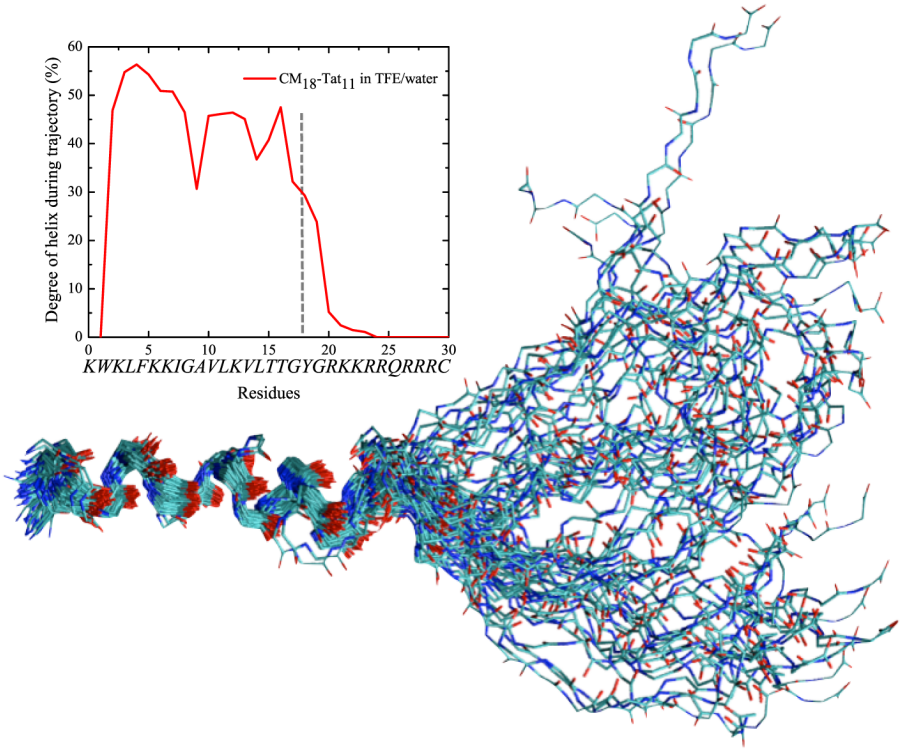

Fig. 2.2 CM_{18}-Tat_{11} MD simulation. Superposition of MD snapshots forming a α-helix in the 2-21 region of the peptide. Only backbone atoms are shown, and the superposition is based on a.a. 1 to 16. Inset: Per-residue percentage of helix conformation during MD trajectories at room temperature (299.5 ºK) of the CM_{18}-Tat_{11} in TFE/water mixture.

2.1.2 CM_{18}-Tat_{11} interaction with biological membranes

Once established that Tat_{11} addition does not affect CM_{18} structural properties, its possible influence on CM_{18} membrane-perturbing activity was tested through the evaluation of CM_{18}-Tat_{11} antimicrobial skills. To this end it was first assessed the minimal bactericidal concentration (MBC) of CM_{18}, CM_{18}-Tat_{11} and Tat_{11} against the standard laboratory strain of *S. aureus* ATCC 33591 by a micro-dilution assay. As shown in Fig. 2.3a, CM_{18} and CM_{18}-Tat_{11} peptides displayed bactericidal activity at a concentration of 0.5 μM and 0.25 μM, respectively, while a considerably higher MBC was observed for Tat_{11} (4 μM), consistently with previously-reported

results[197]. In line with our structural analysis, bactericidal assay data indicate that the addition of Tat_{11} does not reduce CM_{18} activity, as shown by a virtually unaltered, if not decreased, MBC.

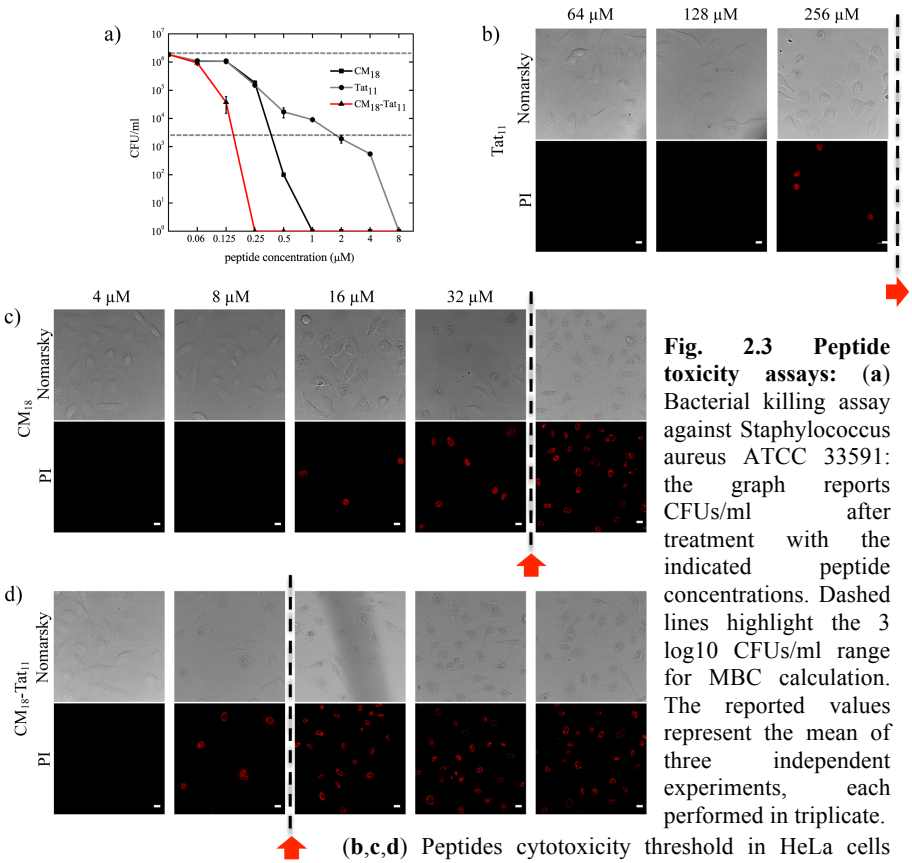

Fig. 2.3 Peptide toxicity assays: (a) Bacterial killing assay against Staphylococcus aureus ATCC 33591: the graph reports CFUs/ml after treatment with the indicated peptide concentrations. Dashed lines highlight the 3 log10 CFUs/ml range for MBC calculation. The reported values represent the mean of three independent experiments, each performed in triplicate. **(b,c,d)** Peptides cytotoxicity threshold in HeLa cells visualized by PI staining. HeLa cells were treated for 30 minutes with increasing concentrations of each peptide. Then cells were washed in PBS and PI was added. Nomarsky (gray) and Propidium Iodide (PI) (red) images for different amounts of Tat_{11} **(a)**, CM_{18} **(b)**, and CM_{18}-Tat_{11} **(c)**. The red arrowed dashed vertical lines indicate the measured viability threshold. Scale bars: 10 μm.

A parallel assay was carried out in order to evaluate the disruption activity of the chimera and of the two isolated moieties on the eukaryotic plasma membrane. The data from this investigation are important for understanding both the specific

cytotoxicity threshold and the 'membrane active concentration' of each peptide. Specifically I performed a co-treatment of PI and increasing peptide amounts in the extracellular medium of HeLa cells (Fig. 2.3b, c, d). Notably, the three peptides maintain the same relative efficacy observed in the bacterial killing assay, but with a significant shift towards higher absolute concentration values (i.e. 8-16 μM for CM_{18}-Tat_{11}, 32-64 μM for CM_{18}, and above 250 μM for Tat_{11}). Both these activity assays were performed with and without the atto-633 fluorophore, with analogous results. These cytotoxicity values set an upper threshold for the safe application of the chimera peptide with eukaryotic cells. So it was decided to proceed in the investigation by running tests on eukaryotic cells with three peptide concentrations below that limit, namely 0.1, 0.5 and 5 μM.

Once verified that the CM_{18} membrane-perturbing properties are reproduced in the chimera peptide, we proceed to verify that also Tat_{11} plasma membrane-interaction skills were preserved in the hybrid vector. As stated in this chapter introduction, the Tat_{11}-module is expected to play a major role in the endosomal uptake due to its strong interaction with cell membranes caused by its arginine content (and the associated net positive charge). This was confirmed by evaluating the amount of vector cellular uptake in the presence of heparin, a known specific inhibitor of Tat-peptide interaction with negatively-charged cell-surface components[198]. As shown in Fig. 2.4, heparin was able to almost completely stop Tat-mediated uptake and significantly reduce CM_{18}-Tat_{11} internalization, while it minimally perturbed CM_{18} internalization.

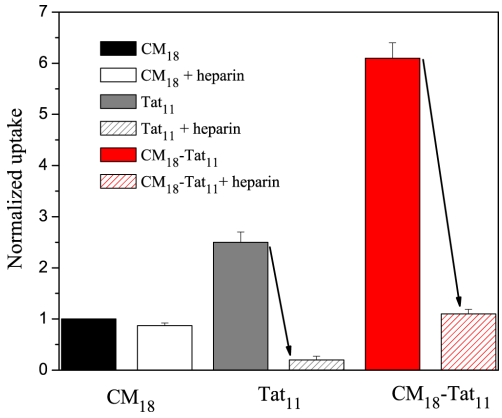

Fig. 2.4 Effect of heparin on peptides uptake. HeLa cells were treated with 0.5 μM of Tat_{11}, CM_{18}, and CM_{18}–Tat_{11} peptides, which were pre-incubated for 1 h at room temperature either in absence or presence of 2.5 μM heparin. Flow cytometry analysis was performed on detached cells. Results are normalized with respect to the mean uptake value obtained for isolated CM_{18}. As expected, heparin is able to almost completely block Tat_{11}-mediated uptake, while it minimally perturbs CM_{18} interaction with the membrane.

Flow cytometry analysis quantitatively showed that CM_{18}-Tat_{11} uptake in HeLa cells is substantially higher (~7 times) compared to isolated CM_{18} (see Fig. 2.5a, lower panel; 0.5 μM peptide concentration). This result is even more significant if considered in light of fluorescence imaging analysis; in fact they suggest that such a difference in cellular uptake relies on a higher vesicle-loading ability of CM_{18}-Tat_{11} compared to CM_{18} rather than on an increase in the overall number of vesicles (see Fig. 2.5a, upper panel, the two picture show almost the same number of vesicles, but with markedly-different signal intensity). Moreover, since isolated-Tat_{11} uptake efficiency is only twice that found with isolated CM_{18} (Fig. 2.5a, lower panel), data indicate an unexpected synergistic effect of the two modules within the chimera, only in part attributable to the total number of positively-charged residues (this effect will be further described in Chapter 4 in order to explain CM contribution on the chimera membrane bilayer interaction after external matrix recruitment). Finally, in order to rule out any possible toxic effect of CM_{18}-Tat_{11} on cell metabolism, the standard water-soluble tetrazolium salt (2-(2-methoxy-4-nitrophenyl)-3-(4-nitrophenyl)-5-(2,4-disulfophenyl)-2H-tetrazolium, monosodium salt, wst-8) assay was performed at each of the three chosen peptide concentrations, using isolated CM_{18} and Tat_{11} as controls. Figure 2.5b shows that the three peptides do not depress cell metabolism at all tested concentrations 2 hours after administration. On the contrary, with respect to untreated cells, a slight increase is observed in the overall cellular activity/metabolism (viability index > 100%), analogously to previous reports[199]. As expected for positive control, cells treated with 20% DMSO showed a 50% metabolism reduction.

Considering the fact that, as described in Chapter 1, CM peptides membrane-perturbing activity display a pronounced threshold effect[142], the observed endosomal uptake increase of CM_{18} module following Tat_{11} conjugation is extremely interesting. In fact, it suggests a selective relocation of the AMP module membrane-disruption function from the plasma membrane to the endosomal compartment. Here it would exert its action without any plasma membrane perturbation, consequently avoiding any side effect on cells viability (as supported by the wst-8 assay).

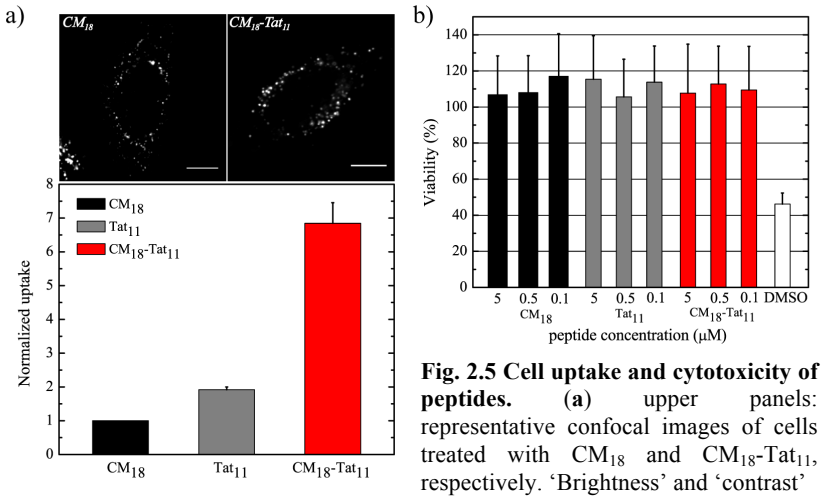

Fig. 2.5 Cell uptake and cytotoxicity of peptides. (**a**) upper panels: representative confocal images of cells treated with CM_{18} and CM_{18}-Tat_{11}, respectively. 'Brightness' and 'contrast' scales were adjusted to obtain almost the same overall intensity in the two images and better visualize vesicles. Scale bar: 10 μm; lower graph: flow cytometry analysis of uptake at 0.5 μM peptide concentration. Results are normalized with respect to the mean uptake value obtained for isolated CM_{18}. (**b**) Wst-8 assay to evaluate cell metabolic activity. The wst-8 reagent was added for 2 hours and absorbance at 450 nm measured. Untreated cells are defined as 100% viable, while cells exposed to 20% dimethyl sulfoxide are used as positive control for decreased metabolic activity.

Finally, for the characterization of the chimera peptide uptake process in eukaryotic cells, one should comment on the intracellular routes paced by CM_{18}-Tat_{11}-loaded vesicles. It was already reported in the first chapter that the uptake of Tat-peptide vectors seems to occur predominantly via macropinocytosis[109], however depending on the cargo, others internalization routes were also reported[186,187]. In order to verify which is the elective endocytosis pathway for CM_{18}-Tat_{11} when applied free of cargo, we performed co-localization assays with specific biomarkers of different endocytic routes. As shown in Fig. 2.6a, the atto-633 labeled CM_{18}-Tat_{11} (red channel) strongly co-localizes with the FITC-labeled 70-kd dextran (green channel), a standard marker of macropinosomes[200]. Moreover, as testified by the colocalization of CM_{18}-Tat_{11} with lysotracker (Fig. 2.6b), lysosomes appear to be the main final localization for the peptide. As control, no significant colocalization is observed between labeled CM_{18}-Tat_{11} and caveolin-E^1GFP, a specific marker of the caveolar pathway (Fig. 2.6c).

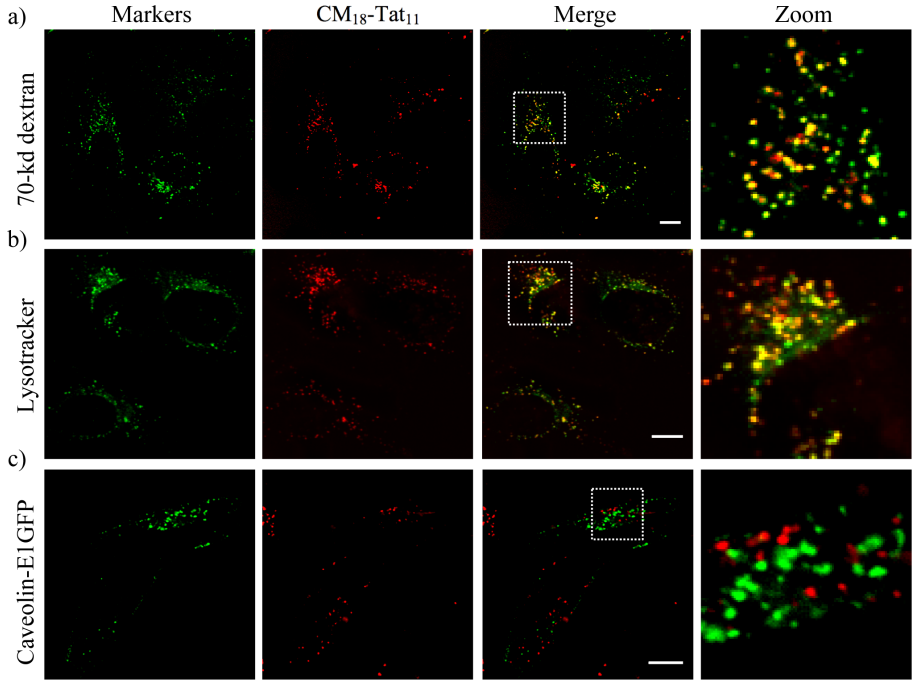

Fig. 2.6 CM_{18}-Tat_{11} internalization route studied by confocal microscopy. Co-treatment with 0.5 µM atto-633-labeled CM_{18}-Tat_{11} and different endocytic fluorescent markers, namely: (**a**) 70-kd Dextran to label macropinocytosis; (**b**) lysotracker to label lysosomes; (**c**) Caveolin-E^{1}GFP to label the caveolar pathway. Co-localization of signals is better showed in the 'merge' and 'zoom' panels. Scale bars: 10 µm.

In conclusion, in the interaction with biological membranes CM_{18}-Tat_{11} vector appears to preserve and combine its isolated components distinctive features. In fact it actively perturbs microbial membranes at the same level of its AMP moiety, while it is massively internalized by endocytosis due to a strong interaction with the extracellular matrix as it happens for its CPP module. The combination of these two features will be very beneficial for the chimera peptide drug-delivery application.

2.2 Evaluation of CM_{18}-Tat_{11} as a drug-delivery vector

The data presented in the previous paragraph suggest that CM_{18} membrane-destabilization properties and Tat_{11} endosomal-uptake skills are preserved, if not enhanced, in the chimera vector. The fact that extracellular-administered CM_{18}-Tat_{11} is then localized and concentrated in the endosomal compartment can suggest that it should be able to efficiently break the endosomal entrapment, locally exploiting CM_{18} activity. To evaluate this hypothesis for preliminary tests, cargo molecules were employed that can be co-administered to the cell medium with CM_{18}-Tat_{11} and whose natural fate would be the engulfment in the endosomal compartments.

2.2.1 CM_{18}-Tat_{11} promotes the escape of Tat_{11}-EGFP fusion protein from endosomal vesicles

The delivery investigation started by exploiting the fluorescent protein EGFP, fused at its N-terminal with Tat_{11} motif (which promotes the protein efficient endosomal uptake). Cell incubation with Tat_{11}-EGFP recombinant protein results in the well known[105] intracellular punctuate fluorescence pattern (Fig. 2.7a). In fact no detectable release into the intracellular milieu occurs and the recombinant proteins are confined within the endocytic vesicles[187].

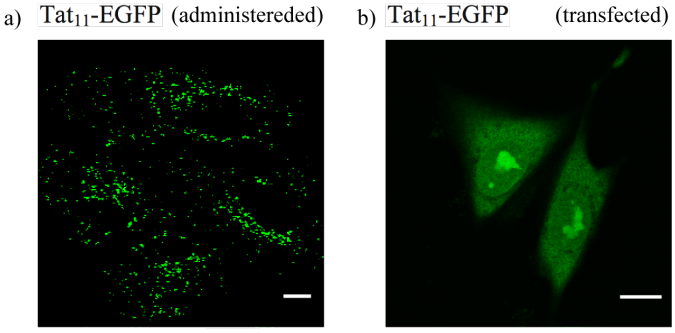

Fig. 2.7 Intracellular distribution of Tat_{11}-EGFP recombinant protein. (**a**) Extracellular administration of 5 µM Tat_{11}-EGFP alone results in extensive vesicular staining, which accumulates at the perinuclear region. (**b**) Cells transiently transfected with Tat_{11}-EGFP plasmid. Scale bars: 10 µm.

A successful membrane destabilization would lead to a different intracellular fluorescence pattern that ideally should match that observed upon transfection with the Tat_{11}-EGFP plasmid. As reported in earlier works from NEST laboratory[179,180], in this case the fluorescence signal is characterized by a homogeneous distribution between compartments with the local enrichment of the nucleoli (Fig. 2.7b). In order to test the chimera activity in the endosomal compartment, Tat_{11}-EGFP was administered to the cell population in the presence of CM_{18}-Tat_{11}. As shown in Fig. 2.8 (merge panel) a high degree of co-localization between the recombinant protein and the peptide fluorescent signals was observed inside the endosomal vesicles, as expected in light of the presence of Tat_{11} moiety in both molecules. More interestingly, for most of the treated cells I detected a diffused Tat_{11}-EGFP fluorescence within the cells (Fig. 2.8). This result is consistent with the release of a significant fraction of the recombinant cargo from the endosomal *cage*. Moreover it is worth noting that the green signal distribution and in particular its nucleolar accumulation indicate the recombinant cargo integrity. Its targeting properties are not affected during the internalization/escaping process, indicating that the cargo molecule escape happens already in early-stage endosomal compartments, before reaching late stages where the characteristic proteolytic enzymes are activated.

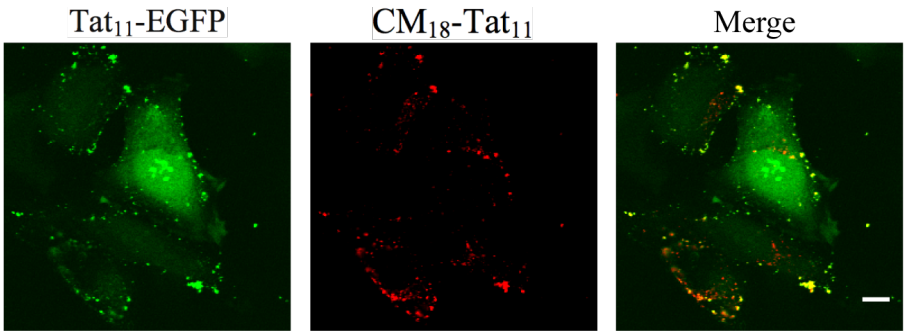

Fig. 2.8 CM_{18}-Tat_{11}-driven cytosolic release of Tat_{11}-EGFP recombinant protein. Co-treatment of 0.5 µM atto-633-labeled CM_{18}-Tat_{11} with 5 µM Tat_{11}-EGFP promotes the protein release from vesicles into the cytoplasm, thus showing its typical intracellular localization. Scale bars: 10 µm.

2.2.2 Quantitative analysis of CM_{18}-Tat_{11}-induced cargo release from vesicles

In order to provide a more quantitative description of CM_{18}-Tat_{11}-induced cargo release from vesicles, a delivery assay based on the membrane-impermeable, intrinsically-fluorescent 622-Da Calcein molecule was exploited. In fact, owing to its photophysical and biological properties, Calcein represents an ideal fluorescent tracer to monitor the effects of membrane-perturbing agents on newly formed vesicles. When administered in the external medium, Calcein is readily taken up by cells via constitutive endocytosis and it is permanently sequestered into vesicles[201]. Furthermore, Calcein release from vesicles leads to a remarkable increase in the overall cell fluorescence. This stems from (i) a reduction in self-quenching of Calcein fluorescence that occurs when it is present at high concentration inside vesicles, and (ii) the transition of Calcein from a pH less than 6.0 (as is the case for most vesicles) to one greater than 7.0 in the cytosol[202]. This yields a very good sensitivity to even small amounts of cargo released into the cell interior, and can be exploited in properly-designed control experiments. As expected, cells incubated with 250 μM of Calcein alone show intense punctuate fluorescence (indicative of an endocytosis-mediated internalization process, as it can be appreciated from Nomarsky panel in Fig. 2.9a) but no detectable diffuse fluorescence in the intracellular milieu (Calcein panel Fig. 2.9a). On the contrary, in the presence of CM_{18}-Tat_{11} (Fig. 2.9b), both a high degree of co-localization of the two molecules within vesicles and a diffuse Calcein signal throughout the intracellular milieu are detected. Analogously to the case of Tat_{11}-EGFP, the latter effect can be ascribed to CM_{18}-Tat_{11}-triggered vesicle destabilization and subsequent release of co-localized cargo into the cytoplasm. As controls, similar experiments were performed in the presence of isolated Tat_{11} (Fig. 2.9c) or CM_{18} (Fig. 2.9d) modules: in spite of the high degree of co-localization within vesicles, neither peptide is able to promote Calcein release into the cell. For the CPP module this is the consequence of low membrane-perturbing activity, while in the case of the AMP moiety, a weak endosomal uptake prevents it from reaching the necessary concentration threshold.

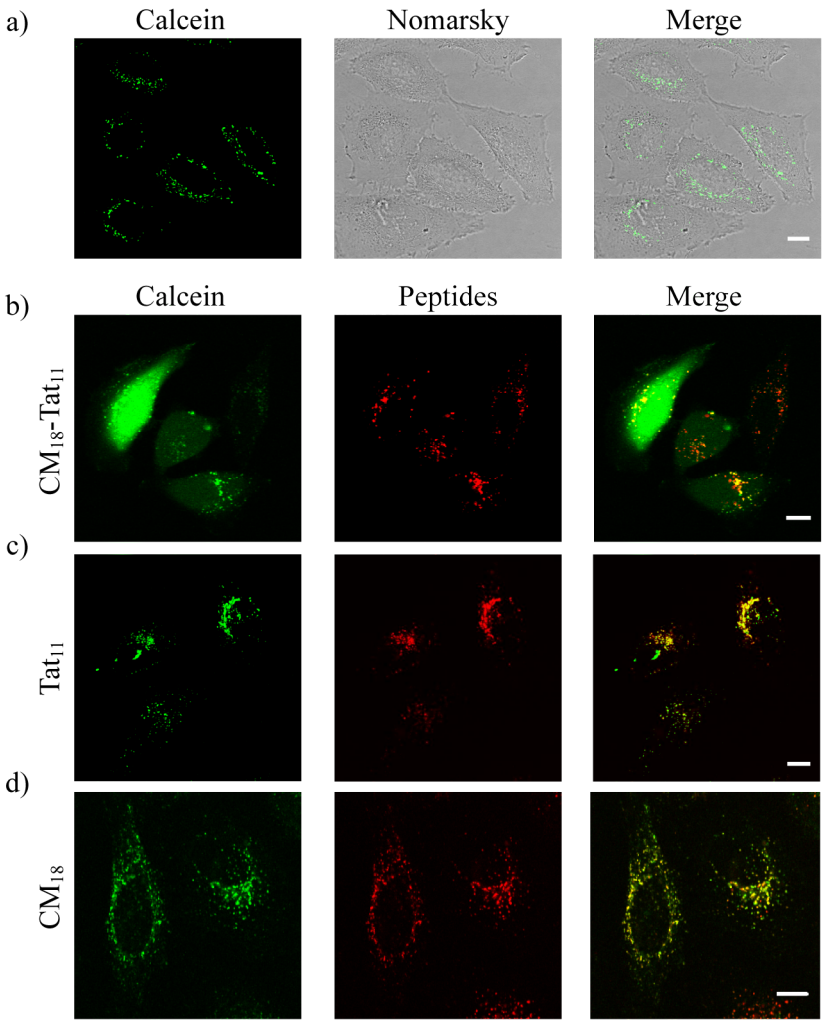

Fig. 2.9 CM_{18}-Tat_{11}-driven cytosolic release of Calcein. Fluorescence and Nomarsky images of cells treated with 250 µM of Calcein alone (**a**) or co-treated with 250 µM of Calcein and 0.5 µM of CM_{18}-Tat_{11} (**b**), Tat_{11} (**c**), and CM_{18} (**d**) respectively. Scale bars: 10 µm.

Finally in order to rule out the possibility that Calcein (as any other cargo) may penetrate directly from the extracellular medium (i.e. through 'temporary pores' in the cell membrane, promoted by the chimera peptide), cells were co-treated with PI, Calcein and CM_{18}-Tat_{11}: as shown in Fig. 2.10a, the few cells with PI-positive nuclei did not match with viable cells showing cytosolic Calcein release. Moreover, to discard the hypothesis of cell-specific activity for CM_{18}-Tat_{11}, the test was also extended to other cell lines, namely CHO-K1 and HUVEC cells (Fig. 2.10b,c).

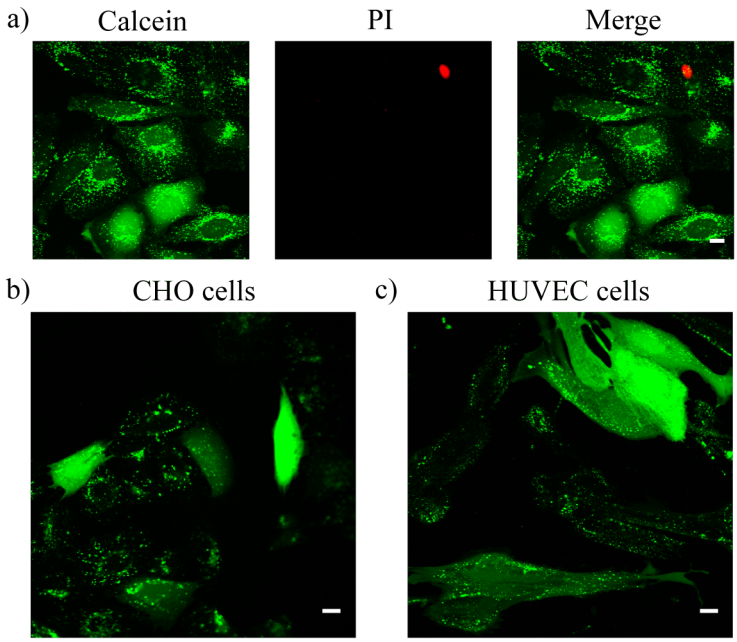

Fig. 2.10 PI assay on Calcein-releasing cells and CM_{18}-Tat_{11}-mediated release of Calcein in different cell lines. (**a**) HeLa cells were incubated for 1 h at 37 °C with culture medium containing 8 µg/mL PI, 250 µM Calcein and 5 µM CM_{18}-Tat_{11}. Confocal microscopy images: from left to right, PI, Calcein and merge image. CHO-K1 (**b**), and HUVEC (**c**) cell lines were treated as described in Fig. 2.9 Confocal images show Calcein intracellular release. Scale bars: 10 µm.

It is worth noting that, at a qualitative cell-population inspection, different cells showed a rather high variability in the fraction of cargo release into the cytoplasm when treated with CM_{18}-Tat_{11} (e.i. cells in Fig. 2.10b). The reason(s) for this variability among different cells are not quite clear, although they may merely stem from differences in the rate/amount of endocytosis occurring in individual cells during culture incubation with Calcein and CM_{18}-Tat_{11}. Following the guidelines of Jones and colleagues[201], Calcein properties were also exploited to provide a flow cytometry-based quantitative estimate of peptide efficiency in the whole population of treated cells. Cells with a Calcein-derived fluorescence 2.5 times (or more) that of controls were scored as presenting 'high Calcein fluorescence', based on the observation that 2.5 was the average fluorescence ratio between cells presenting only punctuate signal and cells with diffuse cytosolic mark: It was found that more than 40% of the cells (part of the red curve highlighted by a grey area in Fig. 2.11) present 'high Calcein fluorescence', thus indicating substantial Calcein release into the cytoplasm.

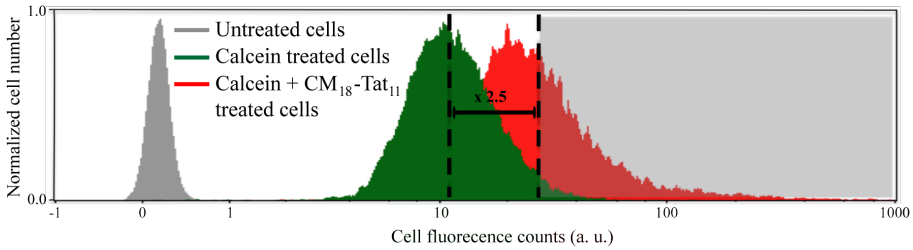

Fig. 2.11 Flow cytometry analysis of Calcein release on cells co-incubated with 250 µM Calcein and 0.5 µM atto-633-labelled CM_{18}-Tat_{11}: gray curve, untreated cells; green curve, Calcein treated cells; red curve, Calcein and CM_{18}-Tat_{11} treated cells; the grey area underlines the cell population with 'high Calcein fluorescence'.

Quantitative analysis of stacks of images acquired by confocal microscopy allowed us also to measure Calcein-release kinetics (Fig. 2.12). Under the conditions tested, the release of Calcein mediated by CM_{18}-Tat_{11} shows a biphasic trend: it increases linearly with time until a plateau is reached and then typically decreases exponentially to an intermediate level (Fig. 2.12). The increase in Calcein cytoplasmic concentration typically lasts up to 2-3 hours, analogously to what observed by others in a similar assay[201]. The subsequent decrease is readily

explained as the effect of P-glycoprotein pumps present on the plasma membrane of HeLa cells: they specifically recognize Calcein with μmolar affinity and actively transport it out of the cell[203].

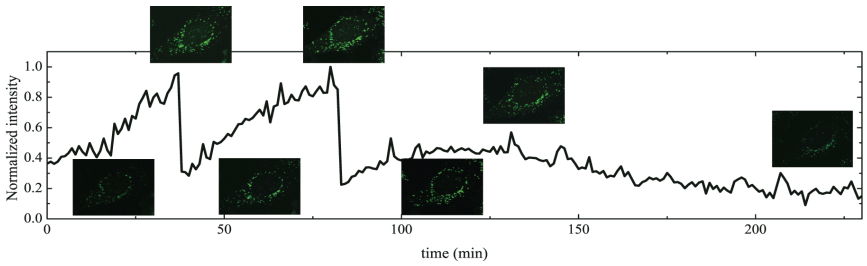

Fig. 2.12 Quantitative analysis of Calcein release kinetics. On a typical 'high Calcein fluorescence' cell its green signal was repeatedly bleached and recovery measured by time-lapse imaging. Characteristic time points of the experiment are associated with the corresponding fluorescence image insets.

2.2.3 CM_{18}-Tat_{11} promotes the cytoplasmic delivery of different size dextrans

In the previous sections it was demonstrated that CM_{18}-Tat_{11} was shown to actively promote the cytosolic release of the 622-Da Calcein molecule as well of the 28-kDa Tat_{11}-EGFP protein cargo. In order to investigate whether there is any cargo-specific effect (e.g. molecular size or chemical composition) on the release activity of CM_{18}-Tat_{11}, the investigation was extended to the delivery properties of the chimera peptide by studying the intracellular fate of a third class of molecules, i.e. dextrans, in presence of CM_{18}-Tat_{11} peptide. This class of sugars was chosen since they efficiently enter cells (mainly via lipid-raft-mediated macropinocytosis[204]) after simple extracellular administration with no spontaneous release from endosomes. Furthermore they are available at different molecular sizes, and fluorescently-labeled versions are commercially accessible. Here we shall describe experiments with 3, 10, and 40-kDa fluorescently-labeled dextrans administrated to the cells medium with or without CM_{18}-Tat_{11} peptide. As expected, when dextrans are administrated alone, only an intracellular punctuate fluorescence pattern from endosomal compartments can be observed (Figs 2.13 a,c,e).

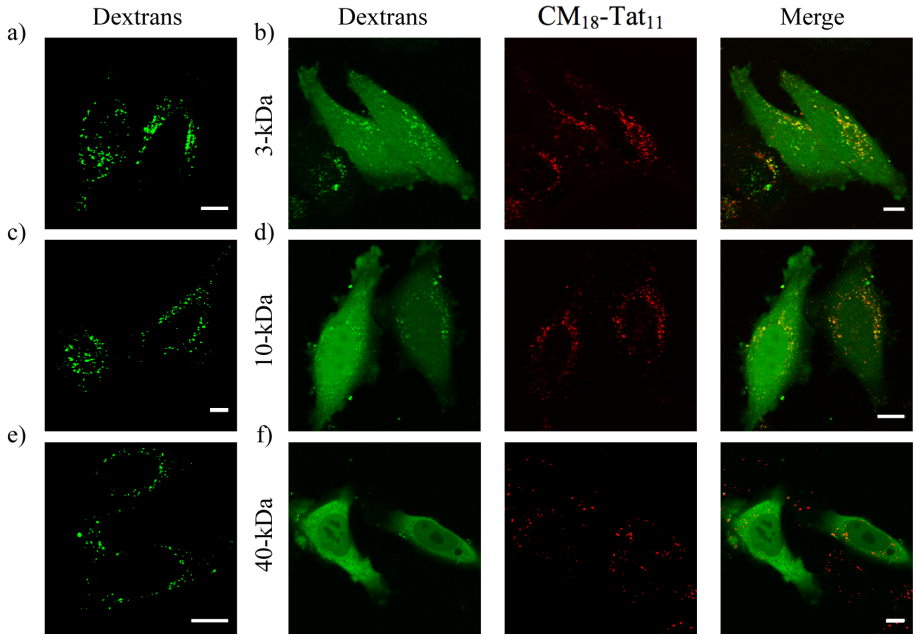

Fig. 2.13 CM_{18}-Tat_{11}-driven cytosolic release of different-size dextrans. Cells co-treatment of 0.5 μM atto-633-labeled CM_{18}-Tat_{11} (in red) results in the cytosolic delivery of fluorescently-labeled 3-kDa (**b**), 10-kDa (**d**), and 40-kDa (**f**) dextrans (in green) compared to different molecular size dextrans administered alone (respectevely **a**,**c**,**e**). Scale bars: 10 μm.

Remarkably, in the presence of CM_{18}-Tat_{11} cells show a detectable level of co-localization of the peptide signal ('red' channel) with the dextran signal ('green' channel) within vesicles (yellow stain in Figs. 2.13b, d, f right panels) and, at the same time, diffused intracellular fluorescence in the green channel (Figs. 2.13b, d, f). In analogy with what observed so far, this diffused signal demonstrates the release of the green-labeled glucans into the cytosol. It should be noted that the intracellular localization of the released molecules depends on their molecular weight, with the 3- and 10-kDa dextrans being homogeneously distributed between the nucleus and the cytoplasm (K_{eq}~1) and the 40-kDa one mostly accumulated in the cytosol (K_{eq}=0.61±0.03), since the hydrodynamic radius of the largest dextrans (~5 nm[205]) is close to the cut-off for passive diffusion through nuclear pores[206].

2.3 CM_{18}-Tat_{11} drug-delivery system overview

The chimera CM_{18}-Tat_{11} peptide was shown to retain both the structural and functional characteristics of the CM_{18} module, i.e. it did assume the typical α-helical secondary structure in hydrophobic environments and was able to perturb bacterial membranes at the expected concentration. At the same time, Tat_{11} addition successfully increased CM_{18} cellular uptake in eukaryotic cells and led to effective internalization through the endosomal route, with no detectable cytotoxic effects in the range of concentrations of interest. A key requisite for the successful application of such a vector to membrane-perturbing system for delivery purposes is the correct balance between the characteristic 'peptide active concentration' (i.e. the concentration needed to disrupt membrane integrity) and the specific cellular location where this concentration is actually achieved. Based on the data presented, the capture of molecules in the vesicular lumen leads to the presence of a CM_{18}-Tat_{11} active concentration (~16 μM, as shown by PI assay) within vesicles, even when only 100 nM of peptide is administered in the extracellular medium. This estimated 100-fold concentration increase should not be overemphasized since the required active concentration of peptide in the vesicles may be lowered by the intrinsically leaky nature of their membrane[207], by the fact that LEs are enriched in the negatively charged phospholipid bis(monoacylglycero)phosphate[208] (comporting a membrane composition similar to the one of bacterial inner membrane), and by the lack of reinforcing cytoskeleton structural proteins which are typical of the plasma membrane[209]. Importantly, these results show that an analogous overall effect is not sufficient to promote membrane disruption in the case of isolated CM_{18}: apparently its uptake is insufficient (~7 times lower than CM_{18}-Tat_{11}) and its membrane-active concentration too high (~64 μM) to create the conditions for membrane disruption inside the vesicle. A similar argument applies to isolated Tat_{11}: its 2-fold higher uptake compared to CM_{18} is contrasted by its very high membrane-active concentration (above 250 μM). Notably, despite its reported activity on membranes, CM_{18}-Tat_{11} does not promote its own release from vesicles into the cytoplasm except for few instances and only when administered at concentrations above 1 μM (Fig. 2.14). The chimera peptide seems to be strongly bounded to the vesicle membrane bilayer, so that for sub-micromolar applications, even when cargo releasing is promoted through the membrane destabilization, the majority of CM_{18}-

Tat_{11} peptides remains trapped in the lipidic boundaries of the ghost vesicle. On the contrary for micromolar administration it is possible to appreciate CM_{18}-Tat_{11} cytosolic release probably owing to the peptide saturation of vesicle inner leaflet, leading to the presence of free peptide in the vesicle internal milieu, which can then reach the cytosol.

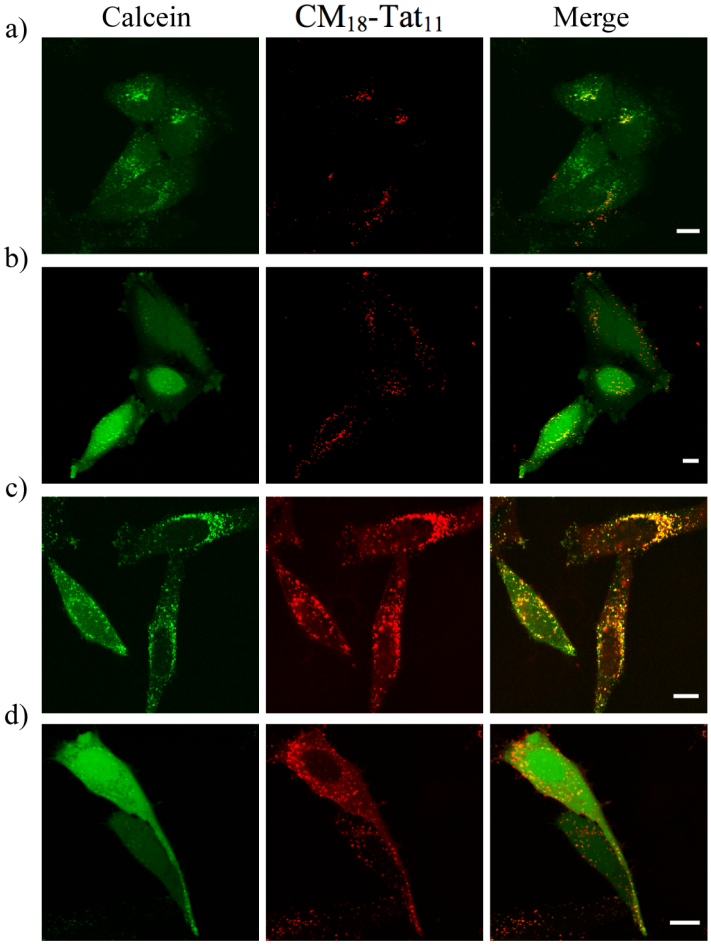

Fig. 2.14 Calcein and CM_{18}-Tat_{11} cell distribution at different CM_{18}-Tat_{11} concentrations. HeLa cells were co-incubated with 250 µM Calcein and 0.1 µM (**a**), or 0.5 µM (**b**), 1 µM (**c**), and 5 µM (**d**) of atto-633-labelled CM_{18}-Tat_{11}. Confocal images show Calcein (left), CM_{18}-Tat_{11} (middle), and their merge (right). Scale bars: 10 µm.

Overall the data presented in this chapter support the scheme of Fig. 2.15: CM_{18}-Tat_{11} enters the cell by endocytosis together with the co-administered macromolecules that at least partially target the same route (Tat_{11}-tagged EGFP in the figure). Then, during the physiological vesicular trafficking, the peptide is quickly able to reach its critical membrane-perturbing concentration, dissolve the bilayer integrity, and promote the release of the co-localized cargo.

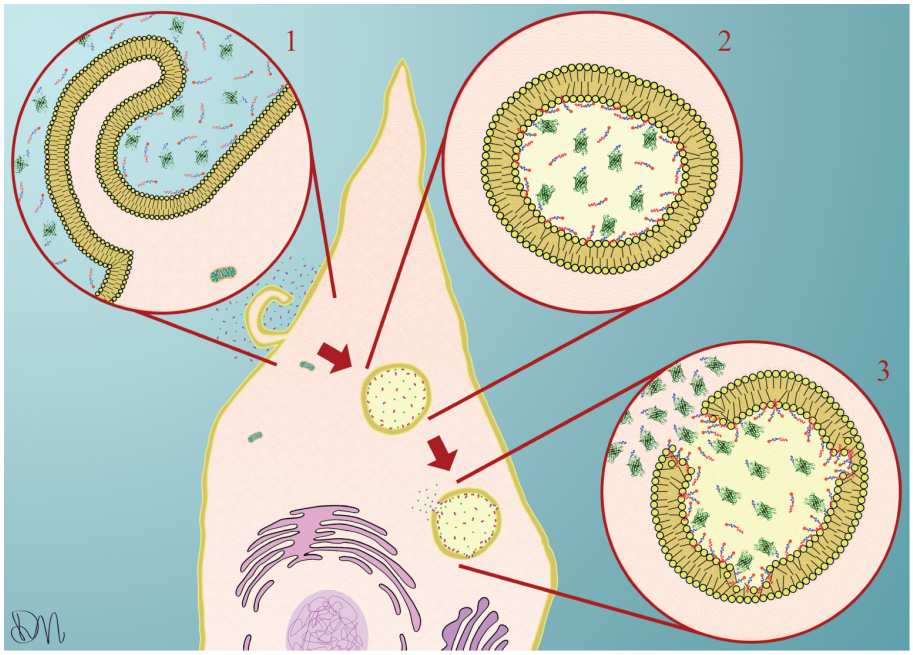

Fig. 2.15 Schematic model of CM_{18}-Tat_{11}-mediated vesicle destabilization and cargo release. Two major steps are highlighted: cargo and peptide endocytic uptake (1); vesicle maturation (2); peptide-driven vesicle-membrane destabilization (3).

Chapter

3

CM_{18}-Tat_{11} as a tool for *in vitro* gene-delivery

Gene therapy is based on the principle that exogenous DNA can adjust the availability of deficient or somewhat altered gene products to normal physiological levels. Its success is largely dependent on the specific delivery-system properties since isolated nucleic acids are easily degraded in the external cell medium and are unable to penetrate biological membranes owing to their molecular weight and negative net charge. Several viral and non-viral approaches were investigated in the last decades[210,211], but they all suffer from severe drawbacks and limitations. For instance, viral vectors such as adenoviruses and retroviruses generally ensure efficient transfection[212] but their clinical use is hindered by several factors, including immune and inflammatory reactions, size limitation on cargo genes, and random integration into the host genome in the case of retroviruses[213,214]. Physical methods such as hydroporation, electroporation, biolistic delivery (gene gun), or ultrasound are all used to deliver DNA across the plasma membrane and result in naked DNA being deposited into the cytoplasm, but can cause significant damage and raise a number of practical problems[215]. Design of non-viral vectors, such as liposomes[216], polymers[217], inorganic nanoparticles[218], and peptides[219] is gaining much attention as a potentially safe, low cost and multi-function option[214,215,220]. In particular, peptide-based materials offer the highly attractive feature of allowing the straightforward incorporation of the specific biological functionalities required for different

biomedical applications (e.g. targeting). Importantly, peptides can be synthesized and characterized with well-established protocols, present relatively low cytotoxicity and immunogenicity, and often can be designed so that they degrade to naturally-occurring compounds in living systems. Concerning cell-penetrating peptides (CPPs) in particular, several studies reported on their applicability to the delivery of DNA plasmids[99,221-227]. Unfortunately, regardless of the detailed peptide sequence and of its possible influence on the mechanism of entry, all reports show that peptide-DNA complexes are massively sequestered into vesicles (for detailed reviews see [228,229]) and this hampers their transfection efficacy, when compared to well-established lipid-based systems[221]. To tackle this issue CM_{18}-Tat_{11} physicochemical properties and intrinsic modularity[230] can be exploited showing its applicability as a delivery vector for pDNA, in this case following direct peptide-cargo conjugation. Briefly, the delivery vector is constituted by a self-assembled CM_{18}-Tat_{11}/DNA complex in which: *i*) the positively-charged arginine-rich Tat_{11} module binds non-covalently to the DNA phosphate groups by simple PBS incubation and then provides high cellular uptake yields for the entire transfectant nanocomplex, while *ii*) the antimicrobial CM_{18} module exerts no significant interactions with the DNA, thus being available to promote successful plasmid intracellular delivery by its well-know membrane-disruptive properties. Interestingly, compared to the delivery applications mentioned in the previous chapter, in this case the AMP module promotes the release of a cargo, which constitutively follows its same internalization route, thus avoiding the need of random vesicle encountering.

In the following paragraphs I shall demonstrate that CM_{18}-Tat_{11}/DNA complexes can be obtained spontaneously in solution, with controlled size, surface charge, and stability. Based on this, a selected candidate will be identified, with the physicochemical properties better suited to yield a combination of high cellular uptake, low cytotoxicity, and efficient plasmid expression. Finally I shall show how vector intracellular trafficking can be monitored in real time and in live cells by confocal microscopy. In particular, fluorescence resonant energy transfer (FRET) between suitably-labeled DNA and peptide modules is exploited to track peptide-DNA disassembly during endocytosis, and correlate this process to transfection timing and efficiency.

3.1 CM_{18}-Tat_{11}/pDNA complexes: physicochemical properties and transfection efficiency evaluation

3.1.1 CM_{18}-Tat_{11}/pDNA binding ability: vector characterization

In recent years, investigations on non-covalent electrostatic interactions of cell-penetrating peptides with nucleic acids prevailed over that on covalent conjugates. This stems from the fact that the synthesis of the latter is cumbersome and hampered by aggregation phenomena. The ability of cationic peptides to bind and condense pDNA stems from ionic interactions between positively-charged amino acids (charged nitrogen atoms from the side chains of arginine, histidine, and lysine residues, or from the N-terminal of the final residue; hereafter defined as N) and negatively-charged base pairs (from phosphate groups, hereafter defined as P) and can be exploited for the successful self-assembly in PBS solution of nanoparticles for gene-delivery[231-233] (see schematic representation in Fig. 3.1a). In order to assess CM_{18}-Tat_{11} suitability as a DNA carrier, a standard ethidium bromide (EtBr) exclusion assay was performed on peptide/pDNA complexes at N:P ratios ranging from 0:1 (isolated DNA) to 32:1. Figure 3.1b shows that CM_{18}-Tat_{11} efficiently condenses the plasmid starting from an N:P ratio of 4:1 (70% exclusion) and is highly effective above 16:1 (complete exclusion of EtBr). On the contrary nanoparticles with N:P ratio lower than 4:1 appear not to be effectively bound, in fact EtBr is able here to penetrate inside their structure or anyway to interact with unloaded pDNA. Agarose-gel retardation assays confirmed that CM_{18}-Tat_{11}/DNA complexes are stabilized by increasing N:P charge ratios: no electroforetic bands corresponding to the isolated plasmid were detected in the gel for N:P ratios above 2:1, even on prolonged runnings (Fig. 3.1c). The gel-loaded complexes remained trapped inside their loading-wells suggesting that no free DNA was detached from its peptidic positive counterparts. It is worth noting that the diffuse signal detected in the loading-wells at N:P 16:1 and 32:1 also suggests an overall complex-charge inversion above the 8:1 threshold, leading to nanoparticle attraction to the negative pole (yellow boxes in Fig. 3.1c).

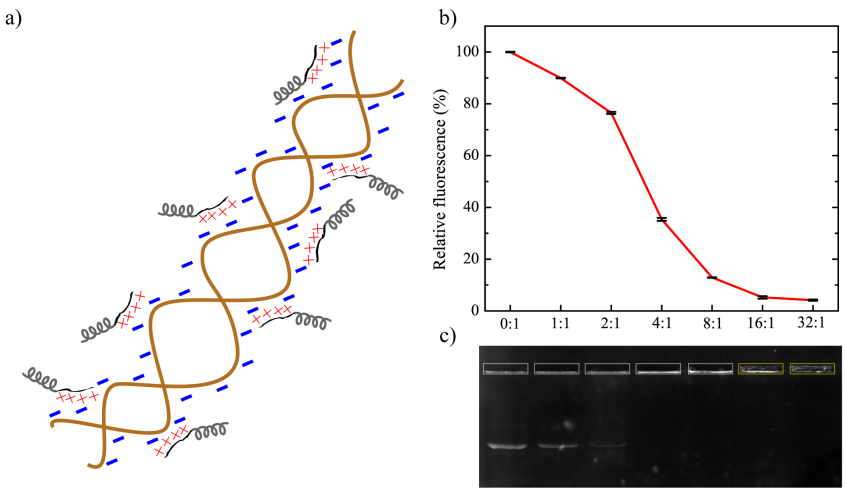

Fig. 3.1 CM_{18}-Tat_{11}/pDNA complex characterization. (**a**) Hypothetical ionic interaction model between pDNA (brown fragment with blue negative charges) and CM_{18}-Tat_{11} peptides (grey: CM_{18} and black: Tat_{11} with red positive charges). (**b**) CM_{18}-Tat_{11} DNA condensation ability analyzed by EtBr exclusion assay. Results for complexes at N:P ratio from 0:1 to 32:1 are given as relative fluorescence and a value of 100% is attributed to the fluorescence of naked DNA with EtBr. The reported values represent the mean of three independent measurements, each performed in triplicate. (**c**) Stability of CM_{18}-Tat_{11}/pDNA binary complex at N/P ratio as in (**b**) evaluated by agarose gel electrophoresis assay. Complexes are electrophoresed on a 0.8% (w/v) agarose gel with TBE running buffer at 80 V for 40 minutes

In order to further investigate the physicochemical properties of peptide/pDNA complexes, particle-size distribution profile and ζ-Potential were measured by dynamic light scattering. A first outcome of this measure was that, independently of the N:P ratio tested, the nanoparticles-size distribution is monodisperse and the formation of aggregates is not promoted. Table 3.1 shows that the particle-size trend nicely mirrors the DNA-protection effect as highlighted by the EtBr exclusion assay and that CM_{18}-Tat_{11}/pDNA complexes appear slightly smaller in size for increasing N:P ratios. This trend probably stems from a ‘condensation effect’ brought by the electrostatics of the peptide-pDNA interaction.

Charge ratio (N:P)	Z-Average diameter
1:1	135.0 ± 7.6
2:1	127.7 ± 3.3
4:1	113.9 ± 1.6
8:1	108.5 ± 1.9
16:1	101.8 ± 3.0
32:1	107.4 ± 2.8

Tab. 3.1 Size distribution of CM_{18}-Tat_{11}/pDNA complexes. Particle size of CM_{18}-Tat_{11}/pDNA binary complexes with different N:P ratios are measured after peptide and pDNA 30-minutes incubation in PBS at room temperature. Particle sizes are expressed as Z-average diameters (nm) and standard deviations are calculated from 20 repeated measurements across 3 trials. In red is highlighted the complex ratio, namely 16:1, showing the best condensation effect.

Notably, the 32:1 complex does not further decrease in size consistently with the saturation of the accessible DNA charges by the peptide positive residues, and likely leads to the presence of free peptide molecules in solution. Additionally, the peptide/pDNA complex ζ-Potential was measured to provide a value for the particle surface net charge. As reported in Fig. 3.2, nanoparticles formed at N:P ratios below 8:1 are in the -35 to -5 mV ζ-Potential range, while those formed at N:P ratios higher than 8:1 show ζ-Potential values above neutrality. It is worth mentioning that a diameter not exceeding 100-300 nm and a net positive nanoparticle surface charge are crucial parameters for any pDNA vector to effectively interact with cell plasma membrane by binding to its negatively-charged counterparts (as extracellular matrix sugars) and be internalized by membrane invaginations inside new endocytic vesicles[210,228].

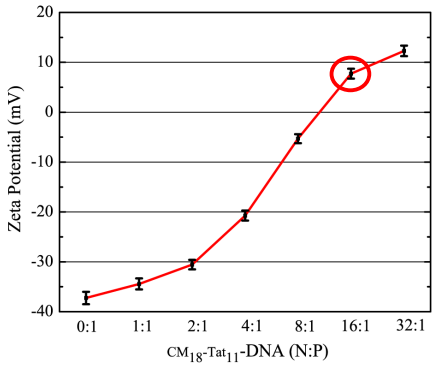

Fig. 3.2 ξ-potentials of CM_{18}-Tat_{11}/pDNA nanoparticles. CM_{18}-Tat_{11}/pDNA binary complexes with N/P ratios as in fig 3.1b are measured at 25 °C by a Zetasizer Nano ZS90 instrument equipped with a red laser of wavelength 630 nm. Each sample is observed with 20 repeated measurements across 3 trials. Error bars in figures indicate standard deviations. Red circle highlights the first complex, namely the 16:1, displaying a net positive charge.

3.1.2 *In vitro* transfection efficiency

The transfection efficiency (TE) of CM_{18}-Tat_{11}/pDNA complexes was measured in HeLa cells by the luciferase expression assay[230]. Based on the data reported above, only N:P ratios from 4:1 to 32:1 were considered eligible for further characterization. As shown in Fig. 3.3a, luciferase gene expression increases by more than two orders magnitude from N:P 4:1 to 16:1 (red columns), reaching a TE comparable with standard lipofection protocols (dark grey column). A further increase of N:P ratio to 32:1 does not lead to further TE improvement, but leads to a slight decrease. As shown by the black columns in Fig. 3.3a, isolated Tat_{11} yields a constant but weak growth in TE for increasing N:P ratios.

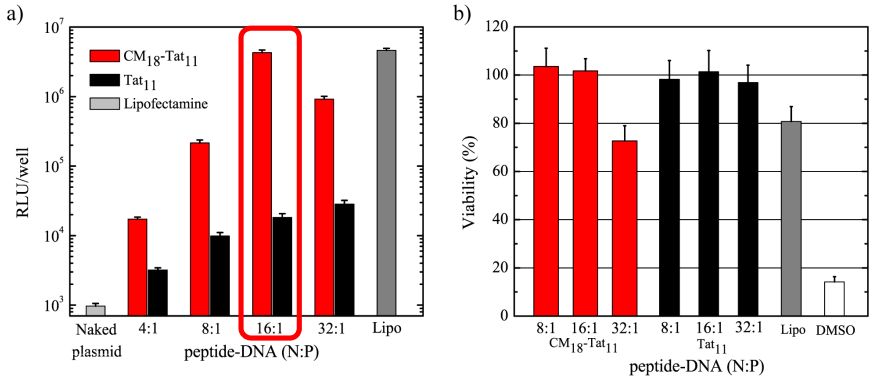

Fig. 3.3 CM_{18}-Tat_{11}/pDNA complex *in vitro* transfection efficiency and cytotoxicity. (**a**) Transgene expression is detected 24 hours after transfection by measuring luciferase activity from an aliquot of the HeLa cells external medium. Light grey column is the mean value obtained with naked DNA, dark grey column is for lipofectamine, while red and black column are respectively for CM_{18}-Tat_{11} and Tat_{11} DNA complex at N:P ratio from 4:1 to 32:1. The reported RLU/well values represent the mean of three independent measurements, each performed in triplicate. In red is highlighted the most efficient complex ratio. (**b**) Wst-8 assay to evaluate cell metabolic activity. The wst-8 reagent was added for 2 hours and absorbance at 450 nm measured. Untreated cells are defined as 100% viable, while cells exposed to 20% dimethyl sulfoxide (white column) are used as positive control for decreased metabolic activity.

The Tat_{11} 4:1 complex displays a TE comparable to its CM_{18}-Tat_{11} analogue, but at higher ratios it shows much lower TE levels. This is not surprising[227] and can be linked to the massive trapping of the complex within endosomes characteristic of Tat_{11}-mediated internalization[188,234]. Here it is important to stress that these Tat_{11} control experiments demonstrate, once again, the pivotal role of the CM_{18} module in the endosomal escape process, thanks to its concentration-dependent membrane-perturbing activity.

The TE analysis was corroborated by performing a complementary cytotoxicity assay (wst-8) on the same treated cells. Figure 3.3b shows that classical lipofection yields a 20% viability reduction (dark grey column), while no significant cell toxicity was observed for Tat_{11}/pDNA and CM_{18}-Tat_{11}/pDNA complexes (red and black columns), except for CM_{18}-Tat_{11}/pDNA complex at a N:P ratio of 32:1, in line with the observed reduction in luciferase production (Fig. 3.3a). The 32:1 complex corresponds to a CM_{18}-Tat_{11} concentration of about 7 μM, a value very close to the hemolytic threshold previously encountered between 8 and 16 μM. Finally, it is worth mentioning that similar measurements (TE and wst-8) were also carried out with analogous results on CHO-K1 cells to rule out any cell-specific activity of the chimera transfectant vector (e.i. TE for the 16:1 complex is reported in Fig. 3.4).

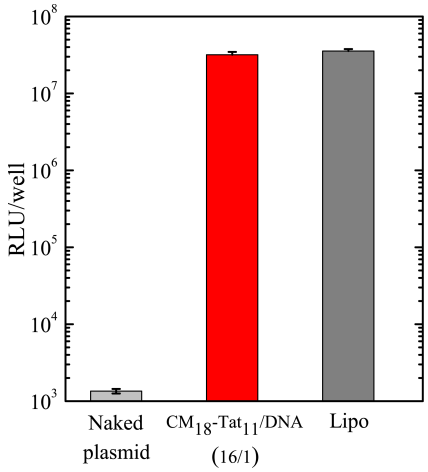

Fig. 3.4 CM_{18}-Tat_{11}/pDNA *in vitro* transfection efficiency in CHO-K1 cells. Transgene expression is detected 24 hours after transfection by measuring luciferase activity from an aliquot of the CHO-K1 cells external medium. Light grey column is the mean value obtained with naked DNA, dark grey column is for lipofectamine, while red column is for CM_{18}-Tat_{11}/DNA complex at N:P ratio 16:1. The reported RLU/well values represent the mean of three independent measurements, each performed in triplicate.

3.2 Gene vector intracellular trafficking

3.2.1 FRET-based real-time imaging of cell uptake dynamics

In order to gain better insight into the process of transfection by the peptide/pDNA complexes employed here, a FRET-based experiment was carried out in living cells. Preliminary *in cuvette* spectroscopic characterization of the peptide/pDNA complex was performed by using a suitable pair of fluorophores (i.e. Cy3 as *donor*, labels the DNA and atto633 as *acceptor*, labels peptides;). As shown in Fig. 3.5a, the characteristic donor-emission peak (560 nm; green curve) is fully quenched upon addition of the acceptor-labeled CM_{18}-Tat_{11} (dark yellow curve). On the contrary, no quenching effect is detected upon addition of unlabeled CM_{18}-Tat_{11} (Fig. 3.5b solid-green and dashed-green curves): this certifies that the observed quenching effect is indeed due to FRET (i.e. due to the close proximity of the two fluorophores within the peptide/pDNA complex).

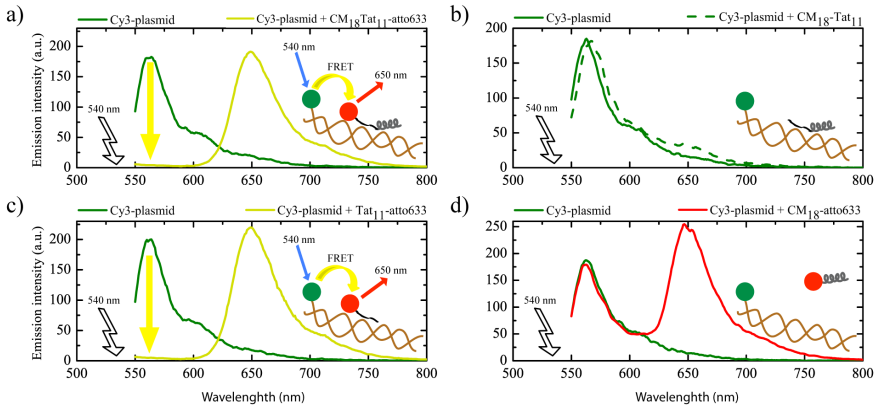

Fig. 3.5 Spectroscopic properties of peptides-atto633/pDNA-Cy3 complexes. Fluorescence spectra are recorded at 37 °C on a spectrofluorometer by exciting at 540 nm and collecting the fluorescence between 550 and 800 nm. First, a fluorescence emission measurement is performed on a phosphate buffer solution of Cy3-labeled pDNA alone (solid green line in **a**, **b**, **c**, **d**). Then, atto633-labeled (dark yellow line in **a**) or unlabeled (dashed green line line in **b**) CM_{18}-Tat_{11} or atto633-labeled Tat_{11} (dark yellow line in **c**) or atto633-labeled CM_{18} (red line in **d**) at N:P ratio 16:1 is added, and the emission spectrum recorded again.

Similar experiments were carried out with isolated Tat_{11} (Fig. 3.5c) and CM_{18} (Fig. 3.5d), as controls. The resulting spectra clearly indicate that the Tat_{11} module is the one responsible for DNA-binding (complete Cy3 quenching), while the CM_{18} module is likely unconstrained (unaltered Cy3 fluorescence spectrum upon acceptor addition). Finally, it is worth mentioning that the atto633 fluorophore alone does not show any significant interaction with labeled pDNA. Based on this knowledge, it can be concluded that FRET is an effective probe to monitor peptide/pDNA complex integrity. Experimentally, the Cy3 signal was recorded as a function of time: low-intensity signal implies stable complex formation, high-intensity signal implies free pDNA. Confocal timelapse imaging experiment were performed on cells incubated with CM_{18}-Tat_{11}-atto633/pDNA-Cy3 binary complexes at N:P ratio 16:1. The four panels in Fig. 3.6a show the petri-dish region selected and imaged at low magnification for 24 hours. It should be highlighted that in this time window cells are clearly replicating, as expected on the basis of HeLa cell cycle. The four panels in Fig. 3.6b and 3.6c show, for a selected area of the field, the fluorescence-signal distribution of CM_{18}-Tat_{11}-atto633 and Cy3-pDNA, respectively. It is evident that, while CM_{18}-Tat_{11}-atto633 signal slightly decreases during transfection (red line in Fig. 3.6d), the DNA-Cy3 signal grows (green line). The former effect can be ascribed to the metabolic degradation of the peptide module in the cells. In fact, after 72h incubation no detectable signal can be recorded (data not shown). On the contrary the increase in donor signal demonstrates that the peptide/pDNA complex is disassembled within vesicles during transfection. More in detail, up to 6h during internalization, the FRET effect is clearly visible (quenching of the *donor*, Fig. 3.6c, 0.5h and 6h panels): as stated above, this is proof of complex integrity. After 12h *donor* emission becomes detectable and reaches its maximum after 24h (Fig. 3.6c, 12h and 24h panels). This loss of FRET indicates that the peptide/pDNA complex is not intact within vesicles. Moreover the overlay of the green (Cy3) and red (atto633) signals at 24h (see Fig. 3.6e) can be used to identify the cells where complex disassembly is taking place (high donor, high acceptor, good colocalization, '+' labels in Fig. 3.7e) and distinguish them from those where the complex is likely still intact (low donor, high acceptor, poor colocalization, '-' labels in the figure). Assuming that these two phenotypes correspond at 24h to transfected and non-transfected cells respectively, by simply counting the number of 'positive' cells in respect of the entire cell population we obtained a 70% TE estimate, a level reminiscent of those typically obtained in transfection assays.

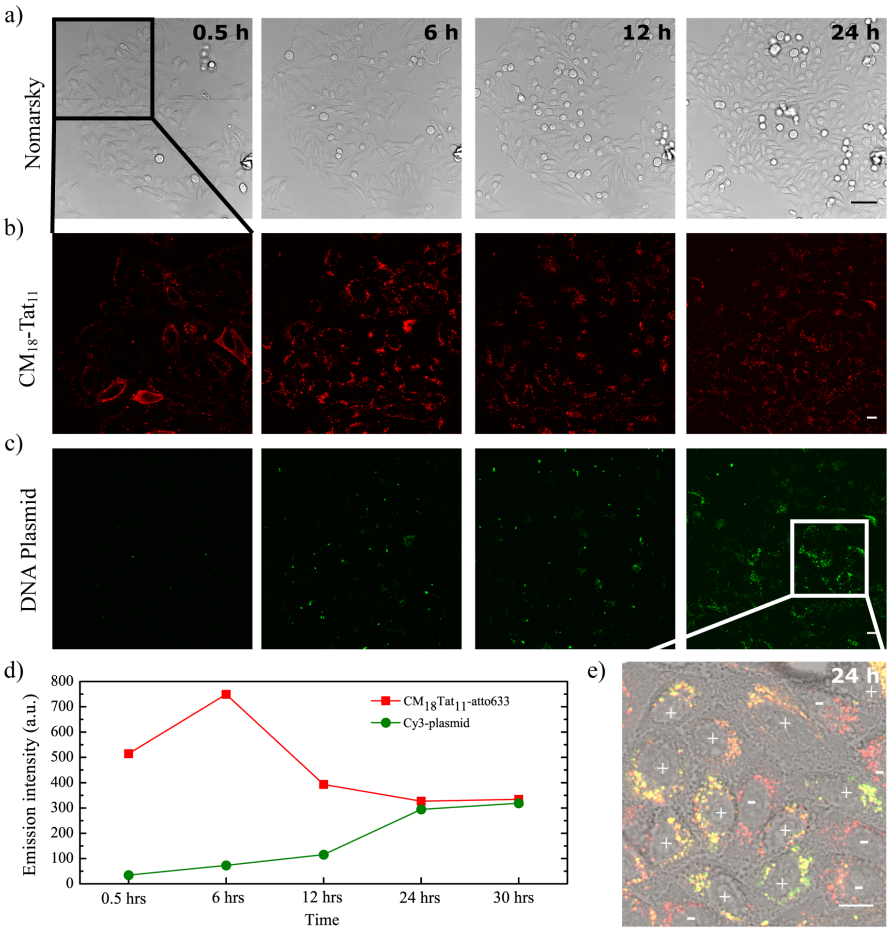

Fig. 3.6 Cell uptake dynamics of peptides-atto633/pDNA-Cy3 complexes. (**a**) Nomarsky images of CLSM timelapse assay performed on cells incubated with CM_{18}-Tat_{11}-atto633/Cy3-pDNA binary complexes at N:P ratio 16:1 applying the same treatments used for a typical transfection experiment. Scale bars: 50 µm. (**b**, **c**) Panels show the fluorescence signal distribution of CM_{18}-Tat_{11}-atto633 (b) and Cy3-plasmid (**c**) from the upper left quadrant of (**a**) panels during the time-lapse. (**d**) Quantitative evaluation of CM_{18}-Tat_{11}-atto633 (red line) and Cy3-pDNA (green line) signals during the time-lapse acquisition. (**e**) 24 hours CM_{18}-Tat_{11}-atto633 (**b**) and Cy3-plasmid (**c**) panels zoom merge. Scale bars: 10 µm.

In order to strengthen the overall interpretation of FRET experiments, acceptor-photobleaching measurements were performed at 24 hours on the two identified cell phenotypes (Fig. 3.6e). As shown in Fig. 3.7a, selective photobleaching of the atto633 acceptor signal on a putatively 'non-transfected' cell (see dashed circle) by short exposure to 633 nm laser at full power raises the donor fluorescence signal, thus showing that the cell is (still) loaded with intact peptide/pDNA complexes. Here the pDNA molecule is trapped inside the endosomal compartment, and still complexed with the chimera peptide, which in turn is not free to fully interact with the endosomal bilayer. The outcome of this scenario is pDNA endosomal entrapment and consequently weak transfection efficiency.

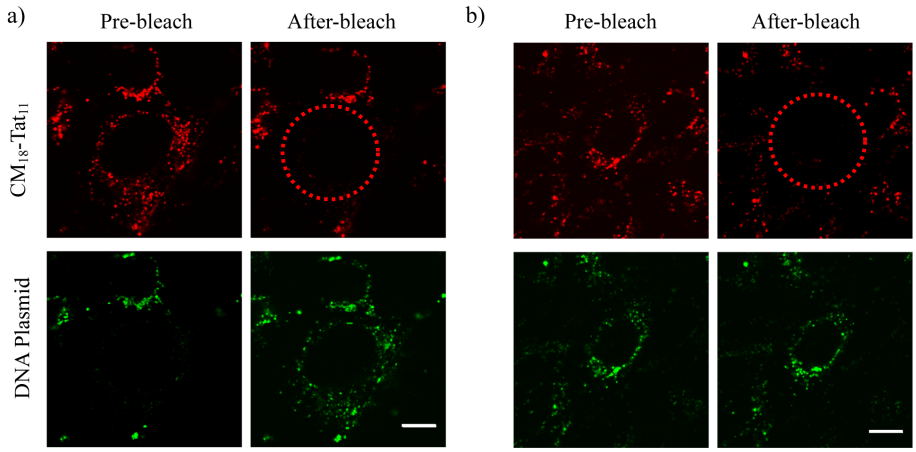

Fig. 3.7 Acceptor photobleaching assay. (**a**, **b**) acceptor photobleaching experiments on putatively non-transfected (**a**) or trasfected (**b**) cells. For both conditions, the first row of images shows CM_{18}-Tat_{11}-atto633 cell signal before and after a scanning bleaching of the whole cell with a 633nm laser at full power, while the second row shows the same for Cy3-pDNA signal. Dashed circles higlight the spot where the atto633 signal is quenched. Scale bar: 10 μm.

On the other hand, photobleaching of the acceptor in a putatively 'transfected' cell does not alter the intensity of the Cy3 donor signal (see Fig. 3.7b), confirming that the two fluorophores are not in close proximity: this in turn may result either from simple detachment of the two intact modules (pDNA and peptide) or from metabolic

degradation of one or both modules. It is worth stressing that the latter possibility is consistent with the co-localization observed after 12 hours between the pDNA-CM_{18}-Tat_{11} complex and a marker of the lysosome, the subcellular compartment dedicated to metabolic degradation (Fig. 3.8).

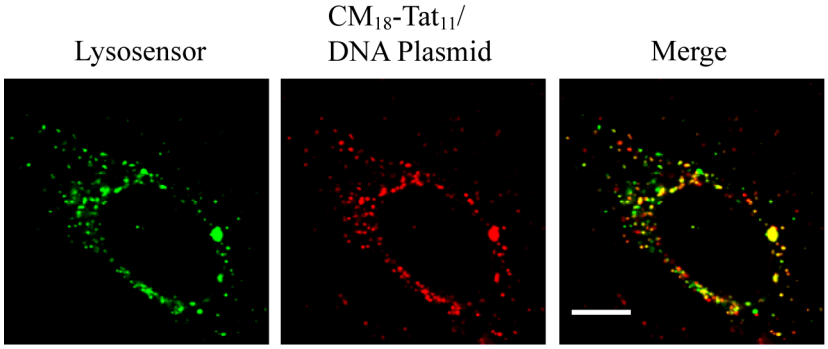

Fig. 3.8. Intracellular final fate of DNA/peptide complex in HeLa cells. Co-localization of Lysosensor signal (lysosome marker, green) with atto633-CM_{18}-Tat_{11}/pDNA 16:1 N:P complex signal (red) after 12 hours of treatment. The overlay (yellow) reveals that the complex is mostly delivered to the lysosomal compartment.

3.2.2 Complex integrity evaluation in endosomal-like conditions

In the attempt to further identify the specific metabolic processes responsible for such a regulation of peptide/pDNA complex integrity during vesicular trafficking, the complex integrity was tested in time by the EtBr exclusion-assay under selected conditions *in cuvette*. As shown in Fig. 3.9a, the lowering of pH from 7.4 to 4.5 (grey scale) that typically occurs within vesicles during the endolysosomal route does not affect complex stability. In fact complete exclusion of EtBr was detected in all tested conditions. On the contrary, in keeping with the final destination of the internalized complexes into lysosomes (see Fig 3.8), addition of the ubiquitous Cathepsin-B enzyme (a lysosomal cysteine protease composed of a dimer of disulfide-linked heavy and light chains) induces almost complete complex disassembly within 24 hours of incubation (with kinetics reminiscent of the FRET loss in cells), but only at pH below 6.5, as expected for this enzyme (Fig. 3.9b). It is worth mentioning that Cathepsin-B elective cutting-site is the peptide bond between adjacent arginine residues: the exclusive localization in the chimera vector of

arginine amino acid couples in multiple sites in the Tat_{11} sequence makes this result an additional clue for the crucial role of this module in complex formation (i.e. pDNA binding and condensation). Its degradation allows at the same time pDNA cargo release and the AMP module unperturbed interaction with the vesicle membrane bilayer.

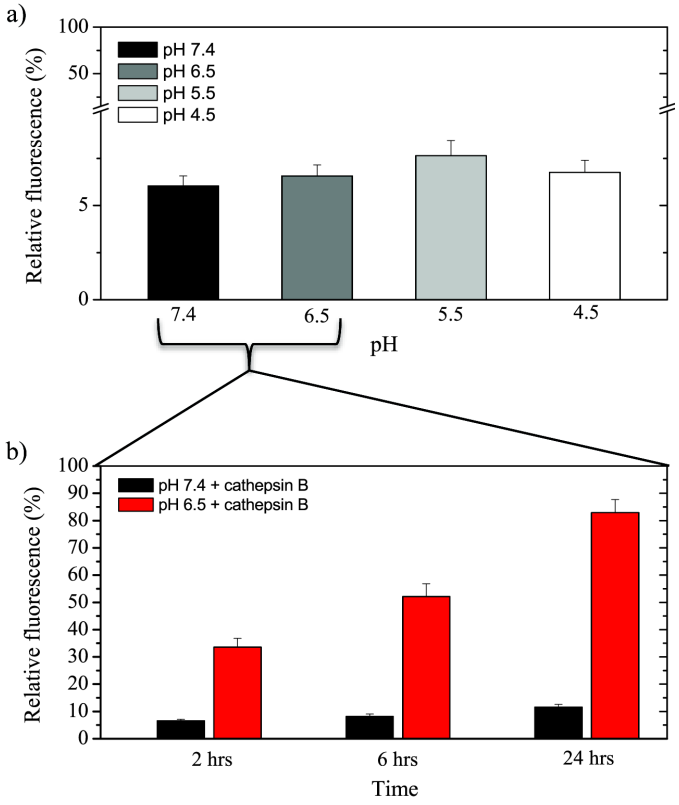

Fig. 3.9 *In vitro* peptide/pDNA complex stability evaluation in endosomal-like conditions. (**a**) EtBr exclusion assay performed as explained in phosphate buffer at different pH: 7.4 (black column), 6.5 (dark grey), 5.5 (light grey), 4.5 (white). Y-axis break from 10% to 15% at 70% of the axis length. (**b**) EtBr exclusion assay 24 hours time-lapse performed at 37°C incubating CM_{18}-Tat_{11}/pDNA binary complexes at pH=7.4 (black column) or pH=6.5 (red) with cathepsin B enzyme.

3.3 Concluding remarks

An ideal CPP for the successful delivery of DNA into cells should perform at least three different tasks: (1) it should tightly bind to the pDNA, thus forming a vector molecule of controlled physicochemical properties capable of protecting the plasmid from early degradation in the extracellular medium; (2) it should favor high-yield, non-toxic cellular uptake of the pDNA-cargo moiety; (3) it should provide an efficient intracellular route for cargo endosomal escape, thus allowing for an efficient transfection efficiency. In the second chapter I showed that the last two properties are potentially offered by a new class of chimeric peptides where the highly-efficient, non-toxic uptake of classical CPPs (i.e. Tat_{11}) is combined to the membrane-disruption ability of a linear cationic α-helical antimicrobial peptide (i.e. CM_{18}). In particular, the CM_{18}-Tat_{11} chimera was shown to possess the correct balance between 'peptide active concentration' (i.e. the concentration needed to perturb membrane integrity) and the specific cellular location where this concentration is achieved (the endosome) thereby promoting efficient intracellular delivery of a variety of biomolecules[230]. However, this property was shown when cargo molecules were co-administered, i. e. randomly encountered by the membrane-disruptive peptide in a subset of vesicles during their independent intracellular trafficking. The 'co-localization' prerequisite may hinder effective (and controlled) delivery of plasmids into cells. In order to tackle this issue and satisfy criterion (1) above, we tested the ability of the CM_{18}-Tat_{11} chimera to efficiently and safely deliver pDNA into living cells following its *conjugation* to the pDNA cargo. DNA-binding properties were shown to associate with the Tat_{11} module alone, in keeping with previous observations presented in the literature[179]. The α-helical CM_{18} module is dispensed from intra-molecular interactions and can exert its membrane-disruption functions. Although the 4:1 N:P complex is able to efficiently condense the pDNA molecule, it does not show significant TE values probably due to its low accumulation in the endosomal compartment. Instead, the 16:1 N:P vector molecule does possess the ability to efficiently enter cells and promote plasmid expression at levels comparable to those achievable by widely-used lipid-based systems. In this respect, it is worth mentioning that analogous peptide-based vectors for *in vitro* transfection usually do not reach the efficiency level of lipid standards, as detailed in several reports[221,225,227,228,235]. This can be explained by the massive peptide/pDNA

complex entrapment within endocytic vesicles, a major limiting factor that was successfully addressed here by the endosomolitic activity of the CM_{18} module. Moreover, CM_{18}-Tat_{11} ensures high transfection with no associated toxicity. The latter result is important since, although being the gold standards for transfection assays, lipid formulations typically elicit oxygen radical-mediated cell toxicity in both immortalized and primary cells[221,236] (e.i. 20% reduction in cell viability measured here). Clearly being non-toxic is a key prerequisite for a transfectant vector for its successful application *in vivo*[221].

Finally, about the vector intracellular fate we demonstrated that the complex progressively disassembles during its vesicular trafficking, with the pDNA becoming virtually completely free (and therefore competent for transfection) within 24 hours of treatment. Interestingly, the measured timing of complex disassembly mirrors that of actual transcription and translation of the luciferase reporter gene. Probably the pH-activated intra-vesicular enzymatic activity (e.i. by cathepsin B within lysosomes) affects peptide integrity, and consequently leads to its release from pDNA within vesicles (see schematic representation in Fig. 3.10).

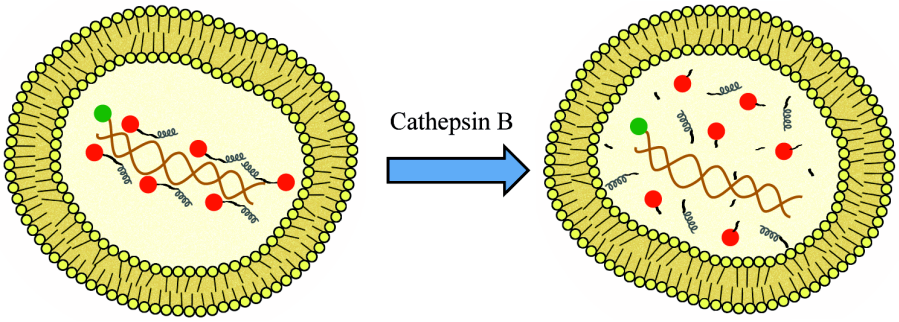

Fig. 3.10 Graphical scheme of CM_{18}-Tat_{11}/pDNA binary complexes disassembling evolution inside endosomal vesicles due to the simultaneous presence of proteolytic enzyme Cathepsin B and low pH values in vesicle milieu.

Overall the presented data support a model where a stable, self-assembled, ~100 nm-sized peptide/pDNA complex enters cells by endocytosis. During the physiological vesicular trafficking, the complex reaches the lysosomial

compartment where at least two mechanisms jointly favor pDNA release: i) the Tat_{11} module is enzymatically degraded, thus releasing both the plasmid and the CM_{18} module (FRET and cathepsin B data); *ii*) once at its critical membrane-perturbing concentration, the CM_{18} module destabilizes bilayer integrity and promotes pDNA release. Somewhat contradictorily, it is reported that the expression of luciferase occurs together with a visible entrapment of (naked) DNA molecules into vesicles. No reports thus far have fully clarified the mechanism of transport of pDNA from vesicles to the nucleus, but analogously to what shown here, the expression of a reporter gene is used as proof of the actual nuclear localization of the plasmid. Consistently with the presented results other authors showed that when a fluorescently-labeled variant of pDNA is used, no detectable amount of fluorescence is observed in the nucleus, even when high-delivery lipid vectors are used[237,238]. Probably only few pDNA molecules (below the detection limit) successfully escape from vesicles and gain access to the nucleus. This interpretation is supported by several studies on lipofection showing that a large fraction of the input pDNA never reaches the nucleus[239-241]. Interestingly, two studies showed that between 30 and 100 times more plasmid microinjected into the cytoplasm is necessary to give levels of gene expression equivalent to those observing following direct injection into the nucleus[242,243]. Indeed pDNA trafficking through the cytoplasm is inefficient and degradation likely plays a major role to further limit the amount of pDNA that can reach the nucleus. It was estimated that the half-life of naked pDNA in the cytoplasm of cells ranges between 50 minutes and 5 hours, so that if a half-life of 3 hours is assumed, during a typical 24 hours transfection experiment, less than 0.4% of the input pDNA would remain by 24 hours[240,241,244-248].

Chapter

4

CM_{18}-Tat_{11} membrane-perturbing activity in living cells

In the previous chapters CM_{18}-Tat_{11} peptide application as delivery vector was reported in co-treatment or in complex with the desired cargo. The chimeric peptide was exploited to promote effective cellular uptake and cytoplasmatic delivery of a several cargoes, from small organic molecules (Calcein, 622 Da) to proteins (GFP, 27 kDa), large polymers (dextran, 3-10-40 kDa), or entire DNA plasmids (pLUC, 5.7 kb, 3700kDa). Tests were performed with several cell lines like HeLa, CHO-K1 and HUVEC[230,249]. The role played by its two moieties during vector intracellular uptake and cargo release action were described. While Tat_{11} peptide is responsible for the promotion of an efficient endosomal uptake in eukaryotic cells, CM_{18} perturbs vesicle membranes in the endosomal network yielding efficient cargo escape. However, a number of aspects of CM_{18}-Tat_{11}-driven cargo endosomal escape are still unclear: the local interaction between the peptide and the endosomal vesicle bilayer shall be investigated in this chapter, specifically focusing on the the chimera endosomal membrane-perturbing mechanism. Since CM_{18}-Tat_{11} does contain a functional antimicrobial peptide (CM_{18}), it is expected that it acts according to one of the three "canonical" mechanisms of membrane permeabilization proposed for this class of sequences, i.e. the "barrel-stave", the

"toroidal", and the "carpet" model (reviewed in [140] and [250]). Briefly, the barrel-stave mechanism requires that peptides bind together (as staves) around a central lumen, forming a pore (the barrel); the peptide hydrophobic segments align with the lipid core region of the bilayer, while their hydrophilic segments face the lumen interior. In the toroidal pore, instead, the polar segments of the peptides associate with the polar head groups of the lipids so that the lipids are forced to tilt up to form a continuous bend from one side to the other of the membrane. Finally, in the carpet mechanism peptides accumulate on the bilayer surface and are attracted by Coulomb forces to the anionic phospholipid head groups covering the membrane surface in a carpet-like manner. Eventually, the surface-oriented peptides lead to the bilayer disruption in a detergent-like manner by forming micelles.

To date the membrane interaction and bilayer-disruption mechanism for AMPs were studied at the molecular level mainly by *in cuvette* and *in silico* assays. For the most significant peptide of the CM series, CM_{15}, a toroidal-pore mechanism was proposed. This conclusion was drawn by investigations upon artificial membrane systems (micelles, vesicles formed from *E. coli* polar lipid extract or eukaryotic mimic liposome) through far-UV CD analysis, site-direct spin-labeling electron paramagnetic resonance studies or MD simulations[195,251-254]. The possibility to directly probe the endosomal membrane location of the active peptide and its bilayer-perturbing mechanism on live cells would represent a significant advancement on the understanding of the mode of action of CM_{18}-Tat_{11}. To this end, two experimental platforms were recently proposed that are suitable to address two complementary aspects of peptide activity within vesicles in live cells, i.e. peptide intravesicular location and membrane-perturbing action. In the following paragraphs I shall first review the basics and potential benefit of each technique and then illustrate their application in the CM_{18}-Tat_{11} case of interest here.

4.1 CM_{18}-Tat_{11} intravesicular localization

4.1.1 Static dielectric constant imaging by a GFP chromophore analog

In an endosomal vesicle there is a strong variation of the polarity at the interface between the lipid bilayer and the internal lumen. As a consequence by measuring the static dielectric constant, ε, in a live cell at a peptide location inside a vesicle yields information on its distance from the lipid bilayer in the endosomal compartment. A few UV-absorbing dyes, such as laurdan and dansyl, were demonstrated to respond optically to ε *in cuvette*[255-257], but their application to cell imaging usually requires two-photon excitation. In a recent communication[258] it was reported the first visible-absorbing/emitting bioconjugable fluorophore that can be used for spatially-resolved ratiometric imaging of ε in live cells by confocal microscopy.

Methyl-4-{(E)-[5-(3,4-dimethoxyphenyl)-2-oxofuran-3(2H)-ylidene]-methyl} benzoate (highlighted with a green circle in Fig 4.1a) is structurally related to the green fluorescent protein chromophore, and can be straightforwardly synthesized from commercially available compounds by means of a single base-catalyzed condensation. Its absorption peaks at 420–430 nm with the extinction coefficient ranging from 30000 to 42000 M^{-1} cm^{-1} (see Fig 4.1b) but its broad spectrum makes it suitable for fluorescence microscopy by adopting common laser sources at 405 or 458 nm. This chromophore is a medium-to-good emitter in most solvents, and its fluorescence displays significant solvatochromism, peaking at ~500 nm in apolar solvents and at ~550 nm in polar ones (see Fig 4.1b). Solvatochromism can be attributed to the conjugated push–pull configuration of the cromophore provided by its functional groups. Moreover this probe shows negligible fluorescence in water, which makes it well-suited for imaging membrane organelles in cells, since the cytoplasmic background is suppressed[259,260].

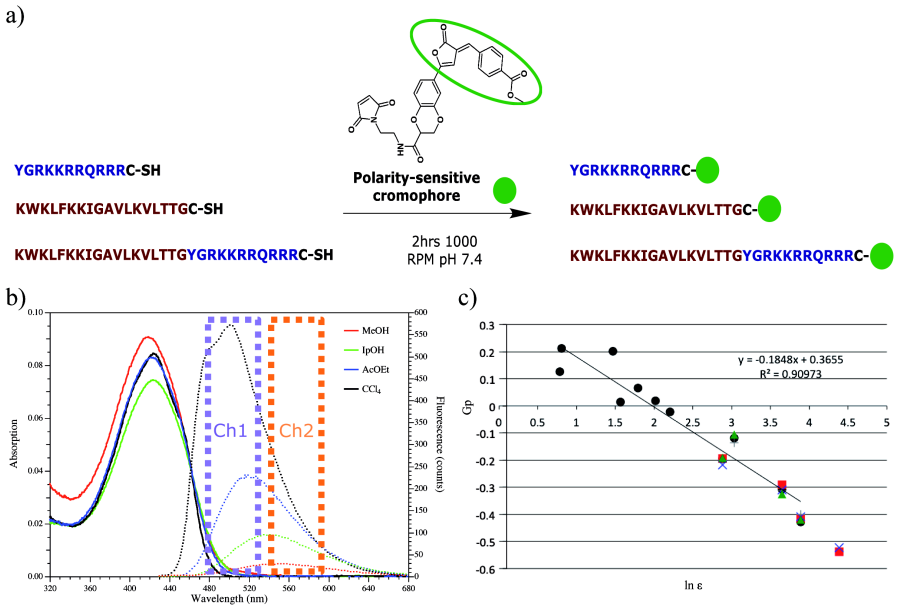

Fig. 4.1. Polarity probe labeling and spectroscopic characterization. (**a**) Schematic reaction between the peptides and the polarity-sensitive cromophore (green circles). Highlighted in green oval the original probe. (**b**) Absorption (dotted lines) and emission (full lines) spectra of the fluorophore in MeOH (red), IpOH (green), AcOEt (blue), and CCl_4 (black). Ch1 and Ch2 intervals are used for ratiometric recordings in emission. (**c**) Calibration plots of GP vs. ln(ε) for the polarity probe by itself (black circles) or conjugated to Tat_{11} (red squares), CM_{18} (blue crosses), CM_{18}-Tat_{11} (grey crosses), and a lipid molecule (green triangles). The line equation is in the *inset* on the right.

This probe can be easily functionalized for bioconjugation in order to allow its use for the study of molecules of interest in living cells. Indeed, replacement of the electron-rich dimethoxyphenyl residue with the electronically analogous 2,3-dihydro-1,4-benzodioxin-3-carboxylic acid residue affords a functionalization site that was exploited to link covalently to 1-myris-toyl-2-hydroxy-sn-glycero-3-phospho-ethanolamine. Notably, it targets lipid bilayer surfaces similarly to other probes bearing phospholipid analogs[261,262]. The introduction of functional groups did not significantly alter the absorption and emission spectral shape, although some reduction of the Stokes shift was reported. In the same way, the functionalization of the original probe with a maleimide group was shown. This approach make it

possible to label the peptides presented in this thesis by a simple reaction with their c-terminal cysteines (Fig. 4.1a).

Ratiometric recording is based on the intensity ratio computed at two or more wavelengths and is applicable to all fluorophores characterized by changes in excitation and/or emission spectra upon some intermolecular interaction[263]. Ratiometry has a relevant role in cell microscopy since the ratiometric response is unaffected by the indicator's concentration, the latter being little controllable in intracellular measurements[263]. The mentioned emission red-shift along with negligible displacement of the absorption band (centered around 410 nm) allowed the use of the GFP-analog probe as emission ratiometric indicator of local polarity. Generalized Polarization (GP) is a classical parameter for ratiometric imaging of polarity in cell microscopy[264]. It is defined as:

$$GP = \frac{I_{\lambda 1} - G \cdot I_{\lambda 2}}{I_{\lambda 1} + G \cdot I_{\lambda 2}},$$

where $I_{\lambda 1}$ and $I_{\lambda 2}$ represent the intensities collected in two wavelength ranges where the emission signal displays opposite trends as a function of medium polarity. G is a parameter accounting for the different collection efficiency in the two spectral ranges. From experiments in solvents of different polarities it is evident that the GP (with λ_1 = 480–525 and λ_2 = 540–580 nm) of the probe is an effective indicator of the local dielectric constant. It is linearly related to the logarithm of ε, indipendent of the molecule it is attached to (Fig. 4.1c).

4.1.2 Ratiometric imaging by confocal microscopy and image analysis

Cell fluorescence was measured using a Leica TCS SP5 SMD inverted confocal microscope (Leica Microsystems AG) interfaced with a diode laser (Picoquant) for excitation at 403 nm. Glass bottom Petri dishes containing cells were mounted in a thermostated chamber at 37°C (Leica Microsystems) and viewed with a 63x 1.2 NA water immersion objective (Leica Microsystems) during polarity fluorophore-labeled peptide or lipid incubation without the need of washing (due to the very low

signal intensity of the fluorophore in polar environments). Images were collected using low excitation power at the sample (10–20 μW) and monitoring the emission at λ_1 and λ_2 ranges by means of an Acousto Optical Beam Splitter (AOBS)-based built-in detectors of the confocal microscope. Data were analyzed by Leica Imaging package version 2.61 and by an ImageJ plugin 'RatioimmGP'. This process allowed the construction of a color-coded (blue: low ε values, red: high ε values) cell polarity map, where ε value was extracted from pixel by pixel GP measurement.

4.1.3 Evaluation of peptides intravesicular spatial distribution

In order to obtain a detailed intravesicular localization of the peptides of interest (administered in conjugation with the polarity probe), their ε value was measured in cultured CHO-K1 cells. As shown by the cell *Nomarsky* image and polarity map in Fig. 4.2a, when the polarity sensor is linked to the previously-described lipid molecule (see section 4.1.1), it localizes prevalently within endosomal vesicles and it seems to be embedded in the membrane bilayer (predominance of 'blue color' in the polarity map, as already oberved by Signore et al.[258]). The lipid polarity map represents a useful reference to study the polarity distribution of labeled peptides (CM_{18}, Tat_{11} or their chimera CM_{18}-Tat_{11}; see Figs 4.2b, c, d) within the intravesicular lumen. All peptides accumulate in the endosomal vesicles after 1 hour incubation. By a qualitative inspection of ε distribution histograms and color-coded zoom images for Tat_{11} and CM_{18}-Tat_{11} (see Figs 4.2e and f), it can be appreciated how the presence of the antimicrobial CM_{18} moiety in the chimera peptide is able to narrow the ε distribution of the fluorophore towards lower values (non polar) compared to isolated Tat_{11}.

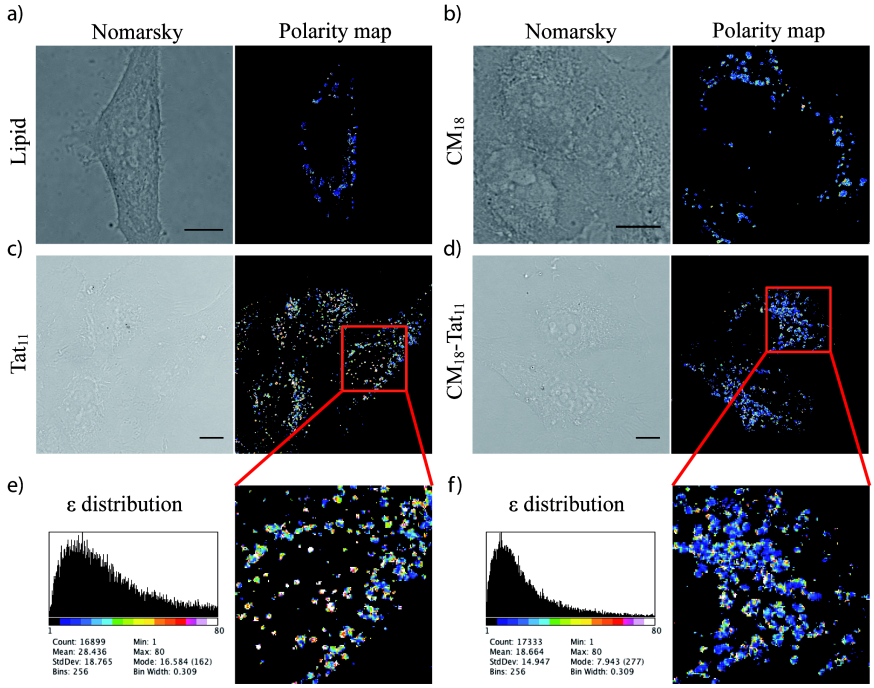

Fig. 4.2 Nomarsky images and polarity maps of CHO-K1 cells treated with GFP cromophore analog labeled (**a**) lipid molecule, (**b**) CM_{18}, (**c**), Tat_{11}, or (**d**) CM_{18}-Tat_{11} after 1 hour of medium incubation without washing. Scale bar: 10 µm. (**e**) and (**f**) respectively report the ε distribution histograms and zoom images of (**c**) and (**d**) for Tat_{11} and CM_{18}-Tat_{11}.

In order to achieve a quantitative evaluation of the peptides spatial distribution inside the vesicular lumen, cell averaged ε values from the polarity maps of 100 CHO-K1 cells per construct were collected. Figure 4.3a shows the ε averaged value distribution for each population of treated cells: as expected, for the lipid molecule (blue histograms) the polarity environment is characterized by a narrow ε distribution, centered at 10, in agreement with the value obtained from capacitance studies on excitable cells[265]. It is interesting to notice that the two moieties of the chimera peptide show opposite trends: the CM_{18}-treated cell population (black columns) yields an average ε value close to the one measured with the lipid (16.5 ± 1.5), while Tat_{11}-treated population (gray bars) yields a much higher average ε

together with a broader distribution (25 ±3). The chimera peptide distribution falls in the middle between those obtained with isolated moieties. It displays a ε distribution centered at 20 ±1.5 with a value distribution more rather similar to CM_{18} (see red histograms).

Some considerations concerning the peptides vesicular localization can be made from their polarity environment data. Figure 4.3b shows a schematic description of the molecular species localization in the vesicular membrane (same colors as their respective histograms; the polarity sensor is pictured in green). The lipid molecules are embedded within the membrane bilayer based on the measured low experimental ε value. On the contrary, Tat_{11} molecules are distributed both on the bilayer surface (Tat_{11} positive charges are supposed to interact with lipids polar heads and in the residual matrix components) and the vesicle internal lumen, in keeping with the broad ε distribution, centered at a high polarity value. Finally the chimera peptides and the antimicrobial moiety are both displayed anchored (due to the amphipatic α-helix of CM_{18}) to the hydrophobic milieu of the membrane bilayer according to the measured ε values (which are close to those characteristic of a non polar environment) and their narrow distribution. The higher average ε value measured for CM_{18}-Tat_{11} peptide compared to CM_{18} suggests that the presence of the CPP moiety may prevent a thorough insertion of the AMP moiety in the bilayer.

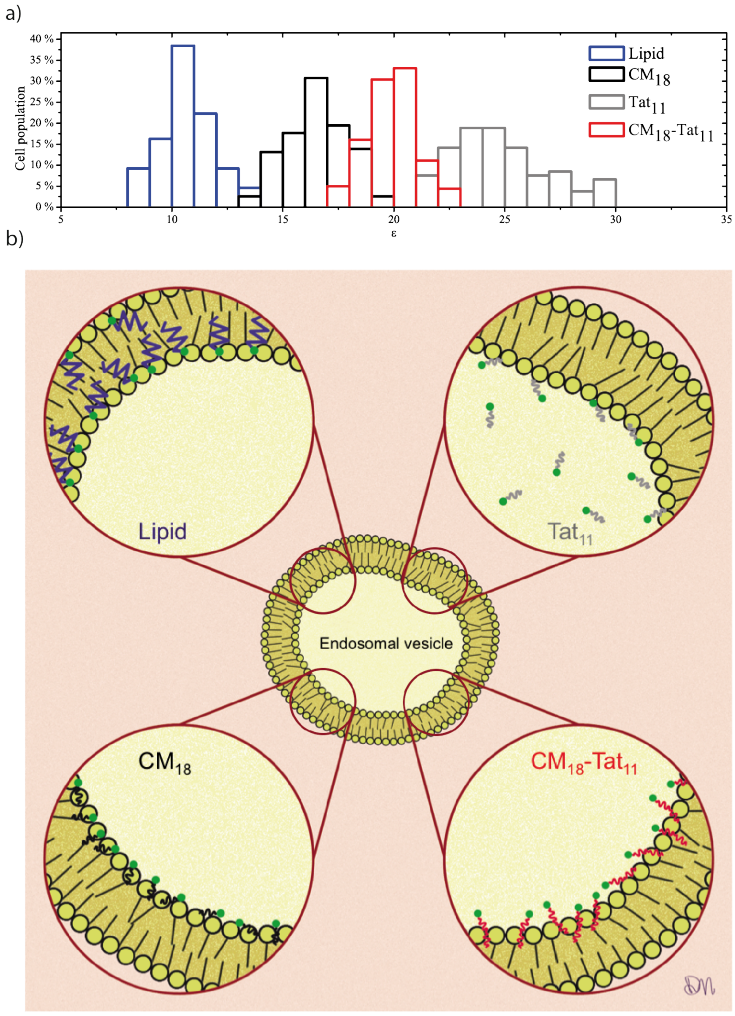

Fig. 4.3 Medium ε distribution in cell population and schematic vesicular membrane localization. (**a**) Medium ε value was extracted from the polarity maps of 100 CHO-K1 cells per molecule and its frequency in cell population pictured in blue for lipid, black for CM_{18}, gray for Tat_{11} and red for CM_{18}-Tat_{11}. (**b**) Graphic representation of the hypothetical distribution of the molecules of interest (represented with the same colors as in (**a**)) inside an endosomal vesicle. The polarity sensor is pictured as a green circle.

4.2 CM_{18}-Tat_{11} membrane-perturbing mechanism

4.2.1 Whole-cell patch-clamp analysis of membrane exogenous currents

In the previous paragraph the vesicular sub-localization of the chimera peptide was investigated, highlighting the membrane-anchoring action of the CM_{18} moiety. This result leaves an open question on how CM_{18}-Tat_{11} exerts its membrane-perturbing activity once accumulated in the proximity of the inner leaflet of the endosomal membrane. A strategy recently employed by Milani et al.[266] allows to assess the biophysical characteristics and the pore formation dynamics of membrane-active peptides under physiological conditions. Briefly, a custom-made, computer-controlled microperfusion system was used to rapidly apply (and remove) the peptide onto a cell, recorded in voltage-clamp, whole-cell configuration. All endogenous conductances were fully blocked[267] (Fig 4.4). Peptide insertion dynamics was therefore obtained by the time course of the exogenous current at a given potential (*Vh*). It was found that the isolated rod outer segment (OS)[268] was particularly suitable for these studies, because it was possible to easily block all the endogenous currents without using any drug (such as tetrodotoxin, tetraethylammonium, dihydropyridines, *etc*.), that could aspecifically interfere with the pore formed by the investigated peptides.

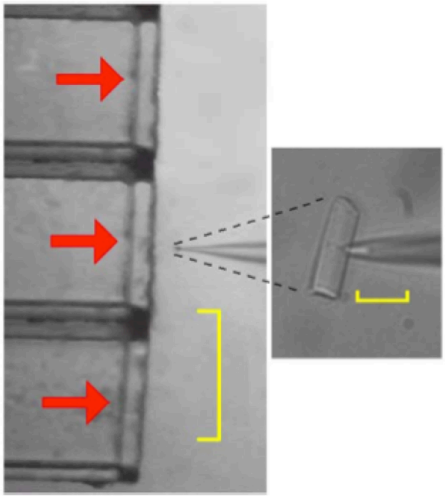

Fig. 4.4. The experimental set employed to investigate the permeabilisation properties of CM_{15} inserted in a natural eukaryotic membrane. *Left* panel, isolated rod outer segment (OS) recorded in whole-cell mode (visible on the right-side of this microphotograph) aligned in front of the multibarreled perfusion pipette for the rapid apply (and remove) of different peptide solutions (visible on the left-side; scale bar is 500 μm; horizontal red arrows denote perfusion flows); *Right* panel, the same OS with the inserted pipette at higher magnification (scale bar is 20 μm). Taken from Milani et al.[266]

Based on the electrophysiology study on CM_{15}, Milani et al.[266] were able to identify the dominant molecular mechanism of membrane disruption proposed for AMPs and summarized at the beginning of the chapter. In detail, the Cecropin-A/Melittin hybrid peptide CM_{15} produced voltage-independent permeabilisation of photoreceptor rod OS membranes. Repetitive peptide applications at concentrations >2 μM caused the progressive increase of the steady-state current amplitude; no single-channel events were detected at low peptide concentration (*i.e.*, ≤1 μM), thus excluding a barrel-stave mechanism of membrane permeabilization. The cell integrity and the substantial reversibility of permeabilization observed at concentrations as high as 10 μM of CM_{15} would not be expected in the case of a carpet mechanism of membrane destabilization, because at these concentrations the micellation process is expected to completely disrupt the OS membrane. Collectively, these results indicated that CM_{15} inserts in the plasma membrane according to a toroidal mechanism of pore formation.

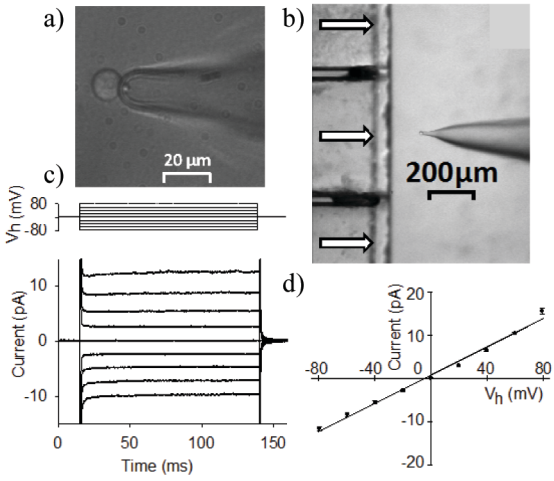

Fig. 4.5. Outline of the technique employed. (**a**) CHO-K1 cell recorded in whole-cell with a pressure-polished pipette; cell is aligned in front of the perfusion pipette (at low magnification in **b**) formed by square glass capillaries (500 μm of side) glued together; horizontal arrows denote perfusion flows. (**c**) Average whole-cell current recorded from representative cells (lower panel; pipette and external solution: 130 mM K^+ + 1 mM Ca^{2+}), subjected to 5 s voltage steps from –80 mV to +80 mV in 10 mV increments (top panel) starting from Vh=0 mV (traces are the average of 6 cells); (**d**) The average current evoked by each voltage step of **b** is plotted against the voltage step amplitude; the points are well fitted by a straight line (correlation coefficient ~0.99), whose angular coefficient gave Rm~6.1 GΩ.

The afore-mentioned approach was used to investigate CM_{18}-Tat_{11} action on the plasma membrane of suspended CHO-K1 cells. In detail, the patch pipette shank

was widened (Fig. 4.5a) through a combination of heat (applied outside of the shank) and air pressure (applied to its lumen) in order to minimize resistance, increase the sensitivity of membrane potential control, and reduce the charging time constant of the cell membrane capacitance. Peptides were applied and removed (in ~50 ms) by moving the automated multi-barreled perfusion pipette on a horizontal plane in front of the cell under study (Fig. 4.5b). This allowed to rapidly switch the cell back and forth from the stream of control perfusion solution (containing 130 mM of K^+ and 1 mM Ca^{2+} to preserve membrane integrity during long recordings) to a stream containing the tested peptide (dissolved in the same perfusion solution). Such an experimental strategy grants the possibility to quantitatively describe membrane activity by measuring the kinetics of current change following both peptide application and withdrawal. Patch pipettes were filled with the perfusion solution, to ensure that current was entirely driven by the holding potential (V_h). Under these conditions, and in the absence of peptides, no voltage- and/or calcium- and/or time-dependent conductance can be registered in CHO-K1 cells, but only a negligible background conductance. Indeed, the current amplitude is time-independent and very small at any physiological voltage value (Fig. 4.5c), yielding a linear (ohmic) current-voltage behavior (Fig. 4.5d) and a characteristic membrane resistance (R_m) above 5 GΩ. At such R_m value current amplitudes as small as 1 pA in a bandwidth of at least 1 kHz can be measured (i.e. any exogenous peptide-induced current can be detected down to the single-channel level). Given this high recording resolution, V_h was set to -20 mV to limit the current amplitude evoked by the strongly permeabilizing peptides, concomitantly ensuring a detectable current from the low permeabilizing ones. With the isolated CHO-K1 continuously held to V_h, R_m was checked before peptide application by means of a brief -10 mV step; various concentrations of CM_{18}-Tat_{11} (or CM_{18}, or Tat_{11}) were then delivered using the fast-perfusion system. Once the current was stable, the cell was returned to the control solution (without peptide) to assess the possible current level recovery and R_m was again measured. In the control solution, repetitive 10 mV pulses were routinely applied to check the access resistance stability.

4.2.2 Membrane-perturbing mechanism evaluation

Concentrations of CM_{18}-Tat_{11} from 0.5 to 3 µM did not elicit detectable currents down to single-channel events (recording were undistinguishable from the one of Fig. 4.6a, *light gray* trace). On the contrary, after 2.6±0.5 seconds (hereafter referred as *delay*) of application of 4 µM CM_{18}-Tat_{11}, a detectable current developed with a roughly exponential trend (activation time constant: 1.5±0.4 seconds) up to steady-state amplitude of 1.0±0.2 nA (Mean±SD values from n=15 cells). As shown by the representative curve in Fig. 4.6a (*black* trace), the permeabilization was irreversible, since the evoked current remained unaltered after peptide removal: these recordings are very similar to the ones obtained with viroporin-derived peptides[269].

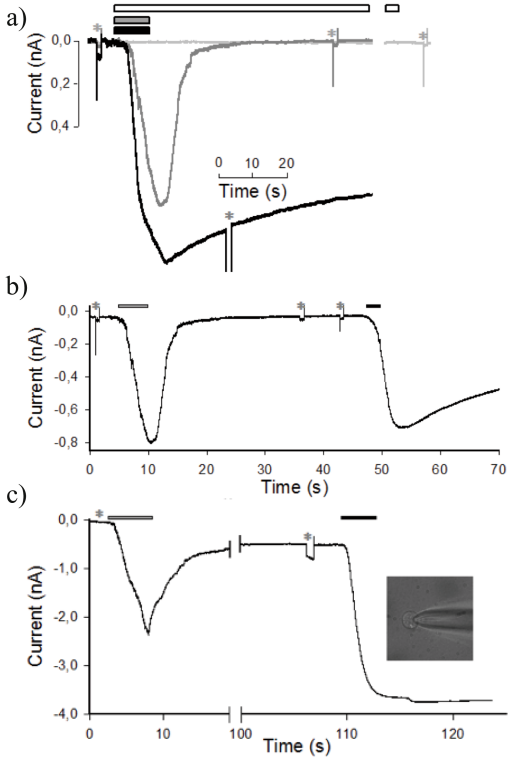

Fig. 4.6. Kinetics of peptide-induced membrane permeabilization of CHO-K1 cells. (**a**) Whole-cell currents recording elicited by the application (in three different cells), of CM_{18}-Tat_{11} (7 s, 4 µM; black bar and black trace), CM_{18} (grey bar and grey trace, recording from panel **a**), and Tat_{11} (71 s, 8 µM; white bar and light grey trace; trace break corresponds to 33s of uninterrupted Tat_{11} perfusion); traces were aligned with peptide timing application. (**b**) Current elicited by the application (for 7 s) and withdrawal of 4 µM CM_{18} (gray bar) and of 4 µM CM_{18}-Tat_{11} (3 s, black bar) on the same cell. (**c**) Whole-cell current recording elicited by the application and withdrawal of CM_{18} (9 s, 8 µM; gray bar) and of CM_{18}-Tat_{11} (7 s, 8 µM, black bar) on the same cell; inset, lysis and death of cell following >10 min application of CM_{18}-Tat_{11}. The membrane resistance in (**a**, **b**, and **c**) was checked before and after peptide application by means of -10 mV pulses, indicated by the asterisks.

Given the structural/functional modularity of CM_{18}-Tat_{11}, the two isolated CM_{18} and Tat_{11} moieties were used as controls for the chimera observed behavior. CHO-K1 cells exposed to CM_{18} concentrations from 0.5 to 4 μM invariably showed detectable membrane currents, i.e. membrane destabilization (amplitude at 4 μM: 1.0±0.1 nA; delay: 0.9±0.2 seconds; time constant of current activation: 2.1±0.7 seconds for n=7 cells). Contrary to what found for CM_{18}-Tat_{11}, however, in this case permeabilization was fully reversible for all tested concentrations upon peptide removal, i.e. current decays roughly exponentially, and R_m fully recovers its former level (representative curve in Fig. 4.6a, *dark grey* trace). However, at CM_{18} concentrations larger than 6 μM, and/or for longer and/or repetitive CM_{18} applications, the recovery of current and of R_m was progressively more incomplete. These recordings were very similar to the ones obtained with the analogous Cecropin-A/Melittin CM_{15} hybrid peptide inserted in the plasma membrane of isolated photoreceptor rod outer segments[266] and in CHO-K1 cells. Since CM_{15} forms transient toroidal pores in the membrane, as previously demonstrated by site-directed spin-labeling electron-paramagnetic-resonance studies[195] and patch-clamp analysis[266], it is reasonable to conclude that these two variants share the same membrane-destabilization mechanism based on the formation of toroidal pores. Finally, even continuous application of Tat_{11} (up to 5 minutes) at concentrations from 0.5 to 8 μM failed to elicit any current for all voltage values tested (from –80 mV to +80 mV), thus demonstrating that this module alone is not able to significantly permeabilize the membrane (Fig. 4.6a, *light grey* trace). In order to provide a direct comparison between membrane-destabilization properties of CM_{18}-Tat_{11} and CM_{18}, data were recorded during sequential administration of these peptides to the same cell at 4 μM (Fig. 4.6b). As expected, CM_{18} produced a reversible current, while CM_{18}-Tat_{11} comported an irreversible membrane destabilization on the same cell. Increasing the peptide concentration to 8 μM still produced a reversible effect in the case of CM_{18} (although with an incomplete recovery, Fig. 4.6c) while cell lysis and death were the outcomes in the case of CM_{18}-Tat_{11} (Fig. 4.6c, and 4.6 *inset*, experiment performed on the same cell).

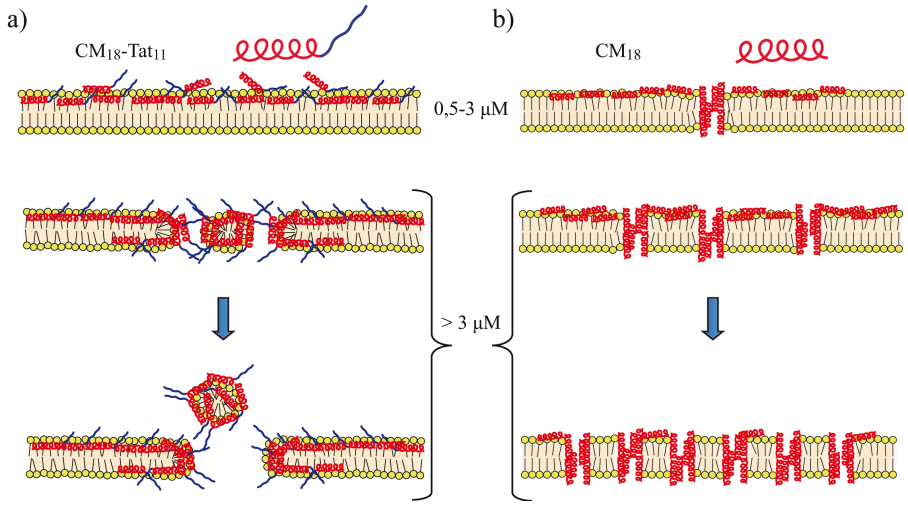

Fig. 4.7. Schematic representation of the membrane destabilization mechanism proposed here for CM_{18}-Tat_{11} (left panel) and CM_{18} (right panel) peptides.

The addition of Tat_{11} sequence to the pore-forming CM_{18} module appears to trigger a switch in its membrane destabilization mechanism (schematic representation in Fig. 4.7). The appearance of irreversible destabilization following an increase in CM_{18}-Tat_{11} concentration from 3 to 4 µM seems to indicate a threshold-effect. This is somewhat surprising in light of the well-known ability of Tat_{11} peptide to accumulate on the plasma membrane[230]. This behaviour can be linked to the fact that the main constituents of the CHO-K1 extracellular matrix (e.g. heparan sulfates and membrane-associated proteoglycans, which are the electrostatic counterparts of Tat_{11} responsible for its accumulation on the plasma membrane[230]) are altered by the trypsinization procedure used here to detach cells before the patch-clamp analysis. Interestingly this makes the plasma membrane more similar to the intracellular vesicle lipid bilayer (where the matrix components are mostly disassembled), i. e. the system where CM_{18}-Tat_{11} peptide should be active during its delivery applications. It is important to stress the main result reported here, i.e. Tat_{11} ability to favor irreversible carpet-like membrane destabilization. This behavior could stem from the high positive charge density of Tat_{11}, which leads to a stronger interaction of the peptide with the phospholipid head groups and to the consequent membrane carpeting effect. This observation is useful to readily explain the results

reported in previous chapters concerning CM_{18}-Tat_{11} application as a delivery vector. In fact, an irreversible membrane destabilization accounts for the observed vesicle release of macromolecules with hydrodynamic radii up to 100 nm (as for pDNA), a value considerably larger than the openings of transmembrane toroidal pores (~1-10 nm)[140].

In conclusion, the data presented here support the delivery scenario where CM_{18}-Tat_{11} peptides enter the cell with no membrane perturbing effects when used at low (i.e. nanomolar) concentrations, exploiting the Tat_{11}-promoted endocytic routes. Then, during the physiological vesicular trafficking, the peptides are held in proximity of the vesicle bilayer by their AMP moiety and can reach a critical concentration thus involving the destabilization of the endosomal bilayer integrity. The carpet mechanism employed by CM_{18}-Tat_{11} promotes the release of big size, co-administered or complexed macromolecules. Specifically, it is worth to mention that the experimental platforms described in this chapter highlight two interesting and unexpected synergetic effects between the two moieties in the chimera peptide. In fact, CM_{18} increases the membrane residence time of Tat_{11} (this can also explain the fact that CM_{18}-Tat_{11} has an endosomal uptake higher than Tat_{11}, as described in Sec. 2.2.2), while the latter promotes the switch of the AMP membrane-perturbing mechanism from “toroidal pore” to “carpet” model, widening the chimera range of drug-delivery applications.

Chapter

5

Concluding remarks and research perspectives

In the last decades intracellular delivery vectors based on CPPs have attracted much interest as they can potentially incorporate specific attributes required for efficient and selective cargo delivery. Among these, the Tat_{11} peptide is by far the most commonly employed in a variety of *in vivo* biotechnological studies. Nonetheless, a crucial limitation presently hampers Tat_{11}-based delivery: endosomal entrapment. After endocytic uptake from the cell medium, the internalized vector is not able to escape (or to let its cargo escape) from vesicular compartments avoiding enzymatic degradation or extracellular recycling.

I identified in the research of a viable endosomal-escaping sequence to conjugate with Tat_{11} the starting point for my investigation. Thus, the first chapter of this thesis work was dedicated to the mechanisms and agents recently exploited in literature for gaining an efficient endosomal escape. In particular I worked on the exploitation of a new source of aminoacidic sequences, which can be efficiently employed in different drug-delivery strategies due to their environment-independent membrane-perturbing activity. In fact for the class of linear cationic α-helical AMPs the lytic-activity can be independent from the environmental conditions of the

specific endosomal entry pathways (pH, enzymatic set, or membrane composition), relying instead only on peptide local concentration and its ratio compared to the membrane surface, which greatly increase during the endocytic trafficking. So I designed a peptide vector, CM_{18}-Tat_{11}, where the Tat_{11} motif is fused to the CM_{18} hybrid (KWKLFKKIGAVLKVLTTG, residues 1-7 of Cecropin-A and 2–12 of Melittin) derived from the well-known α-helical antimicrobial CM peptide series. In chapter 2 the resulting chimera was shown to retain both the structural and functional characteristics of the CM_{18} module, i.e. it did assume the typical α-helical secondary structure in hydrophobic environments and was able to perturb bacterial membranes at the expected concentration. At the same time, Tat_{11} addition successfully increased CM_{18} cellular uptake in eukaryotic cells and led to effective internalization, with no detectable cytotoxic effects in the range of concentrations of interest. Furthermore, the chimera peptide greatly enhanced the cytosolic localization of a vast range of membrane-impermeable molecules (i.e. Tat_{11}-EGFP fusion protein, Calcein, and different-size dextrans) after co-administration in the extracellular milieau.

Altogether, this set of results provides solid proof of CM_{18}-Tat_{11} potential as vector. Actually one must say that its efficacy was proved with cargo molecules co-administered and randomly encountered by the membrane-disruptive peptide in a subset of vesicles during their independent intracellular trafficking. The 'co-localization' prerequisite may hinder effective (and controlled) delivery into cells. In order to tackle this issue I tested the ability of the chimera to efficiently and safely deliver pDNA into living cells following its conjugation to the pDNA cargo (Chapter 3). I demonstrated that the CM_{18}-Tat_{11} possesses intrinsic pDNA binding properties: upon mixing the former with the plasmid, they spontaneously generate a mono-disperse solution of nanoparticles, with controlled physicochemical characteristics, in term of size, surface charge, and stability. Furthermore, by FRET-based spectrofluorimetric assays I showed that the DNA-binding properties are associated with the Tat_{11} module alone, while the α-helical CM_{18} module is dispensed from intra-molecular interactions and can freely exert its membrane-disruption activity. It is finally worth reporting that the 16:1 (N:P ratio) vector molecule does possess the ability to enter cells and promote plasmid expression at levels comparable to those achievable by widely-used lipid-based systems, without the associated cytotoxicity. The delivery complex described in Ch. 3 is clearly just a first example of the many suitable applications of CM_{18}-Tat_{11} as a delivery vector.

In fact, its demonstrated properties make it of interest for boosting the efficacy of a vast range of drugs through the formation of delivery nanoparticles.

In particular, CM_{18}-Tat_{11} ability for nucleic acids condensation recently prompted me to test its applicability in the field of the RNA interference technology. This powerful tool potentially triggers the specific knockout of target mRNA by means of the delivery of siRNA and inhibits the corresponding protein expression when delivered into mammalian cells. However, the low efficiency of siRNA delivery impairs its application in biological and pharmaceutical research[236]. Specifically, the endosomal engulfment represents at the moment a major bottleneck for siRNA efficient delivery[270]. As already seen with pDNA (Chapter 3), I was able to demonstrate that CM_{18}-Tat_{11}/siRNA complexes can form spontaneously in solution, with controlled size, surface charge, and stability.

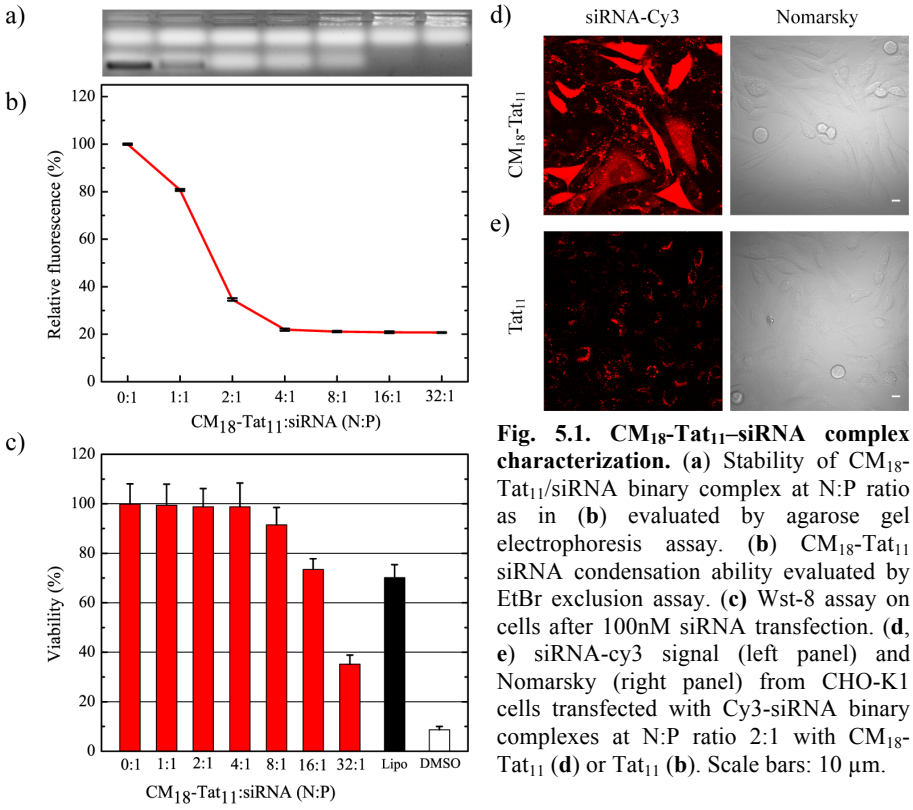

Fig. 5.1. CM_{18}-Tat_{11}–siRNA complex characterization. (**a**) Stability of CM_{18}-Tat_{11}/siRNA binary complex at N:P ratio as in (**b**) evaluated by agarose gel electrophoresis assay. (**b**) CM_{18}-Tat_{11} siRNA condensation ability evaluated by EtBr exclusion assay. (**c**) Wst-8 assay on cells after 100nM siRNA transfection. (**d**, **e**) siRNA-cy3 signal (left panel) and Nomarsky (right panel) from CHO-K1 cells transfected with Cy3-siRNA binary complexes at N:P ratio 2:1 with CM_{18}-Tat_{11} (**d**) or Tat_{11} (**b**). Scale bars: 10 µm.

The ability of cationic peptides to bind and form stable complexes with oligonucleotides (by means of ionic interactions between positively-charged amino acid residues and negatively-charged pDNA base pairs) is generally considered a basic prerequisite for the self-assembly of a stable oligonucleotide-delivery nanoparticle. Thus, to assess CM_{18}-Tat_{11} suitability as a siRNA carrier, I first performed an agarose-gel retardation assay and a standard ethidium bromide exclusion-assay on peptide/siRNA complexes at N:P ratios ranging from 0:1 (isolated siRNA) to 32:1. As shown in Fig. 5.1a,b, CM_{18}-Tat_{11} efficiently condenses the RNA molecules already starting from a N:P ratio of 2:1, and little improvement is given by the addition of more peptide units. In order to further investigate the physicochemical properties of peptide/siRNA complexes, particle size and ζ-Potential were measured by dynamic light scattering. At all N:P ratios CM_{18}-Tat_{11} formed homogenous, unimodal nano-particles with siRNA having sizes in the range of 50–100 nm. Moreover, CM_{18}-Tat_{11}/siRNA particles displayed a marked positive surface charge (zeta-potentials ranging from +20 to +25 mV), except for 1:1 N:P, which showed a ζ-Potential of -18 mV. It is worth mentioning that a diameter not exceeding 300 nm and an overall positive charge of the nanoparticle are crucial parameters for the vector to effectively bind to the negatively-charged-cell membrane counterpart and enter cells. I tested nanoparticle safety for cell delivery applications by performing Wst-8 assay on CHO-K1 cells treated with 100 nM siRNA delivered by CM_{18}-Tat_{11} in different N:P ratios or by lipofectamine. Figure 5.1c shows that classical lipofection yields a 30% viability reduction (black column), while no significant cell toxicity was observed for CM_{18}-Tat_{11}/siRNA complexes (red), except for high N:P ratios. From the evaluation of the above assays I selected the CM_{18}-Tat_{11}:siRNA 2:1 N:P ratio particle as a good candidate for a preliminary qualitative evaluation of its delivery skills in live CHO-K1 cells by confocal microscopy imaging. For this purpose I employed a siRNA molecule labeled with Cy3 fluorophore. As illustrated in Fig. 5.3d, siRNA-Cy3 delivered by CM_{18}-Tat_{11} peptide showed a diffuse signal from the cellular body of most of the cell population already after 45 minutes incubation. Moreover the active role of CM_{18} endosomolytic module in the cytosolic release of the complexed siRNA-Cy3 molecules is highlighted by images in Fig. 5.1f. siRNA-Cy3 molecules delivered by Tat_{11} module alonewere trapped inside the endosome in all cell population in spite of their high uptake. Their fate did not change with time. I believe that this preliminary study on CM_{18}-Tat_{11}-mediated siRNA delivery in live cells represents a solid base for further investigation on siRNA functional quantitative assay.

Finally, a detailed understanding of the chimera endosomal vesicle membrane accumulation and membrane-perturbing action is needed for the rational engineering of novel "modular" cell-penetrating peptides with membrane-disruptive properties based on CM_{18}-Tat_{11} prototype. To this end, I exploited two recently proposed experimental platforms that can yield valuable insights on the endosomal membrane location of the active peptide and its bilayer-perturbing mechanism *in vitro* (Chapter 4). These results impact the peptide vector field both from the methodological point of view (compared to what was done on other endosomolytic peptides until now through artificial membrane system analysis) and from that of the specific outcome of my research with the understanding of the determinant role respectively of the CM_{18} moiety on the intravesicular location (membrane anchoring) of the chimera peptide, and of the Tat_{11} moiety on the membrane-perturbing action of CM_{18}

In this thesis the potential of AMPs sequences for the improvement of CPPs delivery vectors efficiency was explored, addressing several issues about the interactions of both moieties with biological matter and cargo molecules. I deem that, based on the acquired information, optimized carriers for drug delivery can now be designed and applied to specific biological issues. In particular the peptide architecture proposed in this work and its detailed characterization provide reliable guidelines for the high-yield intracellular delivery of oligonucleotides, a field where endosomal escape still appears as the major limiting step[229].

Appendices

Appendix

A

High-yield, non-toxic gene transfer by CM_{18}-Tat_{11} and nanosecond electric pulses

Low-intensity millisecond-long electric-field pulses administered to cells cause plasma-membrane electroporation (EP), i.e. the reversible formation of membrane pores[271]. This process can yield the uptake of macromolecules that display poor membrane-crossing abilities[272]. This approach was extensively exploited for gene transfer applications since besides permeabilizing the cell membrane, electric pulses can also drive DNA towards the transient pores due to electrophoretic effects[273-276]. In all these applications, pulses must be administrated carefully in order to avoid excessive perturbation and even permanent cell damage[277]. The development of devices able to administer pulses in the kV/cm magnitude range at the nanosecond time scale (4-600 ns electric pulses, NPs) recently opened a number of exciting possibilities[278,279]. NPs are actively researched as they appear to target preferentially malignant cells[280] with reduced unwanted thermal effects, thus minimizing the damage to biological tissues[281]. In addition, by modulation of pulse parameters (magnitude, duration, frequency of repetition, and total number)[282,283], NPs showed the ability to perturb not only the plasma membrane, but also membranes of internal organelles (e.g. endosomal vesicles, endoplasmic reticulum, storage vacuoles, etc.[284,285]) thus suggesting new opportunities for targeted membrane electroporation[286]. To date, the reduced size and lifetime of nanopores together with

the intrinsic lack of selectivity limited NP application to the transfer of small/medium-sized cargoes (e.g. few applications with bleomycin, siRNA) through the plasma membrane[287-289]. In this context, some of the properties of CM_{18}-Tat_{11} chimeric peptide[230,249] can be exploited to extend NP applicability in the drug-delivery field. In particular, as shown in Ch. 3, CM_{18}-Tat_{11} was successfully employed as a delivery vector for pDNA. The CM_{18}-Tat_{11}/pDNA complex is readily taken up by cells, accumulates within endocytic vesicles, and promotes vesicle-membrane destabilization followed by cargo cytosolic release. However, this application requires a relatively-high peptide final concentration within vesicles, typically above 10 μM. Notably, these levels can be reached within vesicles even starting from much lower externally-delivered concentration levels that do not appear to perturb the cell membrane[230,249], but the lowest possible peptide concentration is desirable. In this appendix I shall demonstrate the possibility of using synergistically NPs and the chimeric vector. Specifically, I shall show that CM_{18}-Tat_{11}/pDNA vectors administered at very low concentration (not active *per se*) accumulate pDNA molecules into endosomal compartments and can lead to an efficient DNA transfer into the cytoplasm following NP-driven membrane destabilization trigger. Two experimental platforms are used to evaluate the cooperative action of NPs and CM_{18}-Tat_{11} peptide: (i) cytofluorimetric evaluation of the integrity of synthetic 1,2- dioleoyl-sn-glycero-3-phosphocholine (DOPC) giant unilamellar vesicles (GUVs) exposed to CM_{18}-Tat_{11} and NPs; (ii) *in vitro* transfection efficiency of a GFP-encoding plasmid conjugated to CM_{18}-Tat_{11} in presence of NPs. Finally, the molecular details of this cooperative process will be investigated by atomistic (MD) simulations on planar POPC bilayers exposed to the various peptides.

A.1 Evaluation of the cooperative action of NPs and CM_{18}-Tat_{11} peptide

A.1.1 CM_{18}-Tat_{11} and 10 ns NPs cooperative GUVs destabilization activity

In order to investigate the possible cooperative action of CM_{18}-Tat_{11} and NPs on membrane integrity, their co-administration effect was evaluated on GUVs stability.

Rhodamine-labeled GUVs were prepared according to the electroformation protocol described by Angelova et al.[290]. The resulting solution contained GUVs with diameters ranging from 1 to 100 μm, with a majority in the 10-20 μm range. When GUVs are exposed to atto-495-labeled CM_{18}-Tat_{11}, peptide accumulation on the surface of the intact spherical vesicles in suspension is readily visible by confocal-microscopy as shown in Fig. A.1.a. The same accumulation is observed also for isolated modules, CM_{18} and Tat_{11}. A peptide concentration of at least 1 μM is needed to obtain a detectable signal from the vesicle membrane. If vesicles loaded with 1 μM CM_{18}-Tat_{11} are exposed to even a single 10-ns electric pulse, several destabilized "ghost" vesicles deposit on the slide surface, as shown in Fig. A.1.b.

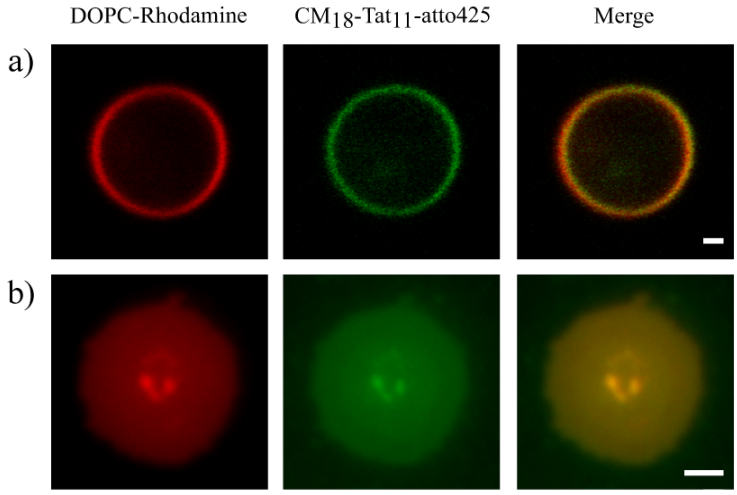

Fig. A.1 Qualitative evaluation of GUVs exposure to CM_{18}-Tat_{11} +/- 10 ns electric pulse(s). (**a**) Confocal fluorescence images of a rhodamine labeled GUV (in red) treated with 1 μM of atto-495 labeled CM_{18}-Tat_{11} peptide (in green). (**b**) GUV treated as in (**a**) plus a 10 ns electric pulse. Scale bar: 10 μm.

By contrast, identical NP administration to peptide-free GUVs does not cause any visible vesicle destabilization. Visual inspection of NP-exposed GUVs treated with 1 μM concentration of the two isolated modules, CM_{18} and Tat_{11}, reveals that the former is able to promote NP-driven vesicle disruption while the latter is not. In

order to obtain a more quantitative picture of the process, I analyzed GUV solutions under different conditions (varying peptide concentration, NP number and/or intensity) by flow cytometry. In such a destabilized system, collapsed vesicles appear preferentially within the debris fraction. Initially the rhodamine-labeled GUV population was exposed to sets of electric pulses different innumber and intensity (1-10-100 pulses; 0.5-2-6.5 kV/mm), without peptide addition. As reported in Fig. A.2.a, none of the tested conditions produces a significant decrease in the number of stable GUVs. Then different amounts of unlabeled CM_{18}-Tat_{11} peptide (from 0.1 to 10 μM) were administered to the GUVs solution, using commercial surfactant Triton X-100 as a positive control. Figure A.2.b shows that CM_{18}-Tat_{11} concentrations up to 3 μM do not destabilize the vesicle membrane, in keeping with the visual inspection described above.

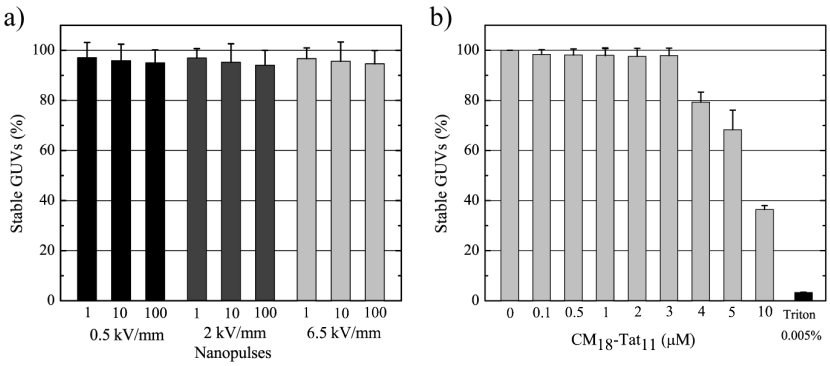

Fig. A.2 Quantitative evaluation of GUVs exposure to CM_{18}-Tat_{11} or 10 ns electric pulse(s). (**a**) Flow cytometry analysis of the stable GUVs % after different number and intensity NPs exposure. (**b**) Same analysis after CM_{18}-Tat_{11} peptide exposure at different concentrations. 0.005% of Triton detergent is used as positive control (right black column).

Once defined the non-destabilizing conditions for NPs and peptide-only treatments, the combination of 1 μM CM_{18}-Tat_{11} and 2 kV/mm electric NPs was tested. Notably, a single pulse is already sufficient to destabilize almost 25% of the vesicle population. The perturbation efficacy increases, as expected, with the number of pulses and reaches 70% with 100 pulses (Fig. A.3.a, red columns). The same quantitative evaluation was carried out on GUVs treated with the two isolated

control peptides. It is worth to notice that delivery of even 100 NPs at 2kV/mm to GUVs loaded with 1 μM of isolated Tat_{11} peptide is not able to promote vesicle-membrane perturbation (Fig. A.3.b, black columns). By contrast, the same treatment administered to GUVs loaded with 1 μM of the CM_{18} module produces the destabilization of more than 50% of the vesicles (Fig. A.3.b, gray columns). These results highlight a specific role of the CM_{18} module in the cooperation with NPs to produce membrane destabilization.

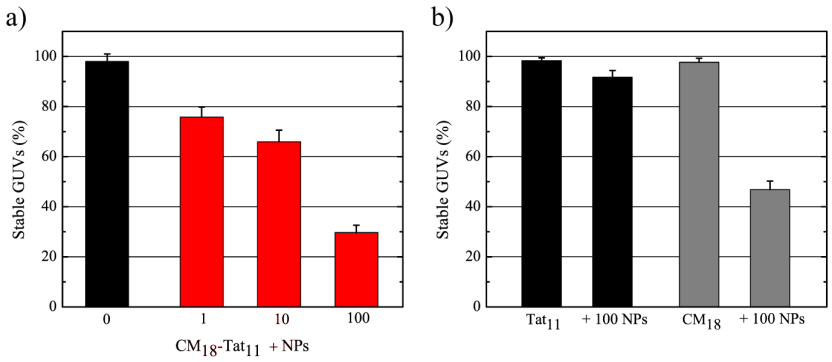

Fig. A.3 Quantitative evaluation of GUVs exposure to peptides or +/- 10 ns electric pulse. (**a**) Flow cytometry analysis of the stable GUVs % after 1 μM CM_{18}-Tat_{11} peptide exposure (black column) plus 1,10 or 100 electric pulses (10 ns each) administration (red columns). (**b**) Same analysis after 1 μM Tat_{11} (left black column) or CM_{18} (left gray column) peptide exposure plus 100 electric pulses administration (right black and gray colmns).

A.1.2 CM_{18}-Tat_{11} and 40 ns NPs cooperative activity on live-cell endosomal vesicles

A suitable experimental platform to probe the practical exploitability of CM_{18}-Tat_{11}/NPs cooperative effect in live cells can be found in the transfection system describe in the paragraph 3.2.2. CM_{18}-Tat_{11} ability to drive efficient pDNA transfection *in vitro* is strictly dependent on the peptide-pDNA stoichiometric ratio, which reflects onto the vector surface charge and its consequent ability to enter cells and accumulate within endosomes. In other words, peptide/pDNA formulations leading to intra-vesicular peptide concentrations below its critical endosomolityic threshold are not competent for gene transfer. As an example of this

condition CM_{18}-Tat_{11}/pDNA complexes formed at a N:P ratio of 4:1 was selected. When administered to cells, these complexes are not active *per se*[249] (see Fig. 3.3). An experimental protocol was set up to measure the TE in adherent HeLa cells upon the combined administration of peptide/pDNA vectors and NPs.

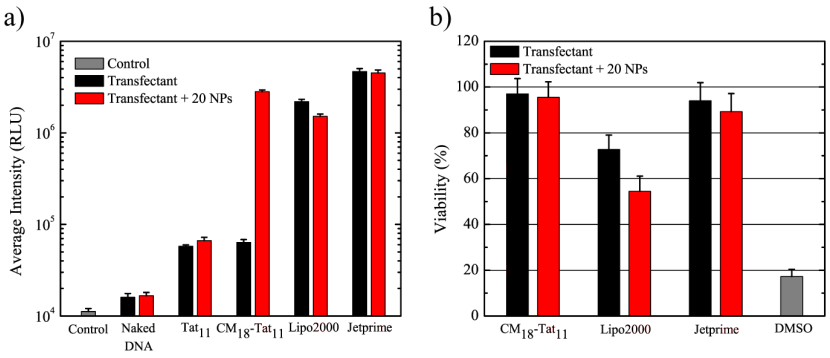

Fig. A.4 Vector/pDNA complex +/- 40 ns electric pulses *in vitro* TE and cytotoxicity. (**a**) Transgene expression is detected 24 hours after transfection by flow cytometry analysis of 15.000 detached HeLa cells per sample. An average GFP intensity per cell was obtained for each sample. Grey column represents the mean value obtained for un-treated cells, while red and black columns are respectively for vector/pDNA complex +/- 20 electric pulses (40 ns each). The reported average RLU values represent the mean of three independent measurements, each performed in triplicate. (**b**) Wst-8 assay to evaluate cell metabolic activity. Un-treated cells are defined as 100% viable, while cells exposed to 20% dimethyl sulfoxide (gray column) are used as positive control for decreased metabolic activity. As previously, red and black columns are respectively for vector/pDNA complex +/- 20 electric pulses.

As expected, if NPs are not administered, the TE elicited by a total CM_{18}-Tat_{11} concentration of 0.3 μM is of the same order of magnitude of naked pDNA (i.e. more than one order of magnitude lower than commercial transfectants) (Fig. A.4.a, black columns). Notably, the administration of n=20 NPs of 40 ns each is sufficient to increase CM_{18}-Tat_{11}-driven TE by more than one order of magnitude, making it similar to commercial standards (Fig A.4.a, red columns). Interestingly, the same treatment does not boost the TE levels reached by isolated Tat_{11}, Lipo2000 or Jetprime. This analysis can be implemented by performing a complementary cytotoxicity assay (WST-8) on the same transfected cells. Figure A.4.b shows that

classical lipofection, in absence of pulses, yields more than 20% viability reduction, while no significant cell toxicity is observed for CM_{18}-Tat_{11} and Jetprime (black columns). The administration of NPs causes an additional decrease in the viability of Lipo2000-treated cells, but does not affect CM_{18}-Tat_{11}- or Jetprime-treated cells (Fig. A.4.b, red columns). Additional tests on membrane permeabilization were conducted using the YO-PRO-1 assay (Fig. A.5).

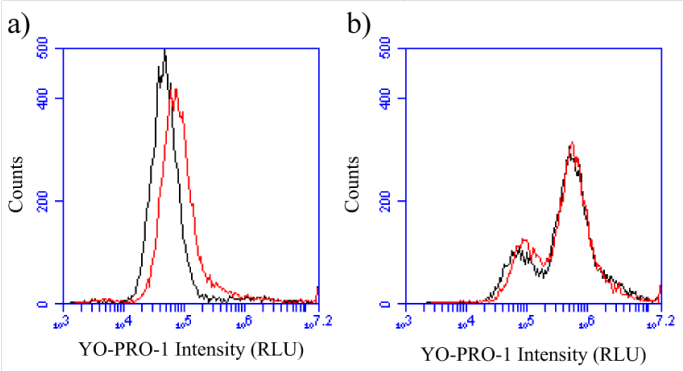

Fig. A.5 YO-PRO-1 assay on cells exposed to CM_{18}-Tat_{11} +/- 40 ns electric pulses. (a) YO-PRO-1 organic dye (5 µM) was administered to the medium of detached cells exposed (red line) or not (black line) to CM_{18}-Tat_{11} and its average fluorescence intensity per cell was evaluated by flow cytometry from 10.000 cells per sample. (**b**) Same conditions as in (**a**), but cells were analyzed 10 minutes after 20 NPs (40 ns) delivery.

Cells exposed only to CM_{18}-Tat_{11} do not show any increment in YO-PRO-1 signal compared to untreated cells, confirming that the plasma membrane is not perturbed. On the other hand the strong increase in the intracellular YO-PRO-1 signal after NPs administration (both in presence and absence of CM_{18}-Tat_{11}) indicates the formation of reversible nanopores at the level of the plasma membrane. Combined to TE data and WST-8 viability test, these assays confirm that NP-peptide cooperation leads to irreversible membrane destabilization only within endosomes, although NP-induced transient perturbation is still present at the plasma membrane.

A.1.3 Atomistic MD simulations of the molecular mechanism of NP-mediated cooperative effect

The results reported in the previous paragraphs indicate a synergy between NPs and membrane-perturbing peptides that can lead to irreversible membrane perturbation in a lipid bilayer environment. However, the mechanism by which this cooperation takes place in the lipid bilayer needs clarification. Atomistic MD simulations were employed to investigate at the molecular level the effect of NPs on membrane integrity in the presence of CM_{18}-Tat_{11} and control peptides. Because of obvious computational limitations, the simulation concerned only a fraction of the vesicle surface, i.e. the portion that is perpendicular to the applied field. The setting consisted of a planar POPC bilayer patch where a single chimera peptide is placed with its unstructured portion extruding from the membrane surface and its α-helical portion about 5 Å below the membrane-solution interface and parallel to the membrane surface (following the work performed by Bhargava et al.[291] on the CM_{15} analogue). Such localization is well suited to bury non-polar side chains in the hydrophobic core of the membrane, while positioning lysine residues to interact with lipid phosphates. As shown in Fig. A.6.a and b, once the bilayer patch is exposed to an electric field above the electrophoretic threshold, an hydrophilic pore forms in the bilayer within a couple of nanoseconds, in agreement with analogous simulations performed by others[289,292]. It is worth noting that the peptide α-helical structure is not affected by the electric field exposure. Also, there is no evidence of the peptide pulling out or in from the bilayer under these conditions, probably due to its strong stability in the membrane environment. During the 10 ns exposure to the electric field the nanopore starts to expand (see Fig. A.6.c) and, when located close enough to the pore mouth, the peptide is electrophoretically dragged along the field direction into the hydrophilic pore (see Fig. A.6.c) keeping its structural stability (i.e. the CM_{18} α-helix remains allocated under the polar heads but now almost perpendicular to the membrane surface, while the highly-charged unstructured Tat_{11} portion remains exposed to the hydrophilic milieu, facing the nanopore). As soon as the electric field is switched off, the nanopore starts to collapse (see Fig A.6.d), but the complete reversibility of the electroporation process is impaired by the presence of CM_{18}-Tat_{11} peptide within the pore membrane (see Fig. A.6.e and f).

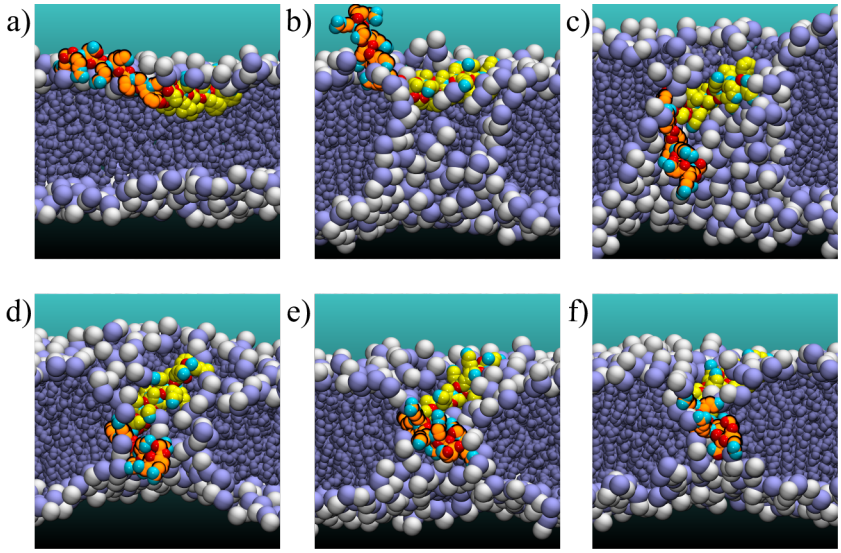

Fig. A.6 MD simulation of POPC bilayer patch exposure to CM_{18}-Tat_{11} and 10 ns electric pulse. Molecular snapshots of CM_{18}-Tat_{11} peptide (shown as van der Waals structure; CM_{18} in yellow and Tat_{11} in orange) interaction with an aqueous pore (water omitted for clarity) within a POPC membrane (headgroups shown as white and purple spheres and hydrophobic tails as purple chains) caused by a 10 ns perpendicular electric pulse. Panels (**a**) to (**c**) represent snapshots along the 10-ns application of a high electric field, while in (**d**,**e** and **f**) it is pictured the system configuration after the E field has been switched off.

This event introduces a defect in the membrane bilayer. Interestingly, subsequent administration of a new 10-ns long NP to the same bilayer causes the formation of a new nanopore always starting from the peptide location. It appears that the latter represents a 'weak' spot in the membrane. Finally, the same MD simulation process was operated with the two isolated peptide modules to better understand their involvement in the defect formation. As shown in Fig A.7 (upper panels), CM_{18} can be dragged into the pore and reoriented along the pore axis, even if it is sensibly slower compared to CM_{18}-Tat_{11}, probably due to its lower content of positive charges. As the electric field switches off, CM_{18} behaves similarly to the chimeric peptide and introduces a defect in the bilayer (Fig A.7, lower panels).

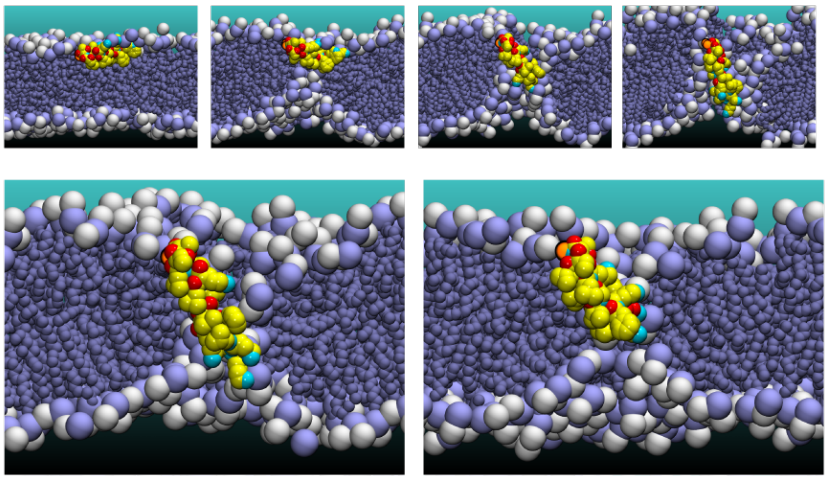

Fig A.7 MD simulation of CM_{18} molecular interaction with a membrane bilayer during NP shooting. The four upper panels represent snapshots along a 10-ns simulation run of the POPC bilayer/ CM_{18} during the application of a high electric field, while in the two lower panels it is pictured the system configuration after the E field has been switched off. The color setting is as in Fig A.6.

On the contrary, the Tat_{11} module placed in proximity of the bilayer does interact with phosphate negative charges and is strongly affected by the electric field due to its high charge density (consistently with a report by Herce et al.[293]). Anyway, Tat_{11} peptide is not able to linger on the hydrophilic nanopore long enough to impair the complete reversibility of the electroporation process (see Fig A.8).

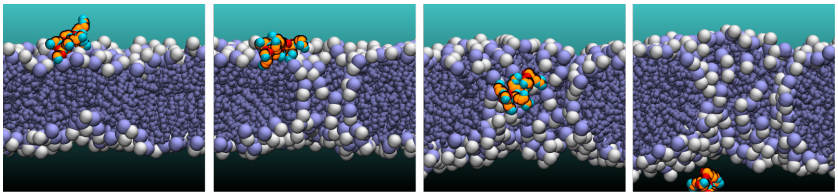

Fig A.8 MD simulation of Tat_{11} molecular translocation through a membrane bilayer during NP shooting. Molecular snapshots of the mechanism of electrotransfer of a Tat_{11} molecule through an electric field-promoted aqueous pore within a POPC membrane (color setting as in in Fig A.6). Snapshots were taken sequentially at 0, 2, 6, and 10 ns of an MD trajectory.

A.2 Concluding remarks

The rational under the new gene-transfer methodology proposed in this appendix is to test the possibility to exploit synergistically the CPP and AMP skills of CM_{18}-Tat_{11} with electroporation approaches in order to lower the required peptide concentration and, at the same time, confine NP-induced membrane perturbation to cell internal vesicles with negligible collateral damage to the plasma membrane. Preliminary *in cuvette* tests on GUVs proved that this hypothesis is viable: 10-ns electric pulses administrations to CM_{18}- or CM_{18}-Tat_{11}-loaded GUVs lead to a significant (more than 2/3) drop in the number of stable vesicles. The same procedure was then tested on endosomal vesicles of living cells. These are a much more complex membrane system and represent at the moment one of the most important obstacles to overcome for gene transfer by nonviral vectors[1,15,194]. 16:1 N:P ratio peptide/pDNA complex administered at micromolar concentrations in the medium represents a very efficient *in vitro* transfectant system (as showed in Chap. 3). On the contrary the 4:1 complex, despite its identical stability, does not exhibit a significant gene transfer activity at any tested concentration, most likely due to a CM_{18} accumulation within vesicles below its threshold activity. Notably, the TE of the 4:1 complex administered at nanomolar concentration can be increased at levels comparable with transfection golden standards by the concomitant exposure of cells to 40-ns pulses. The fourfold pulse length required for membrane-bilayer disruption by NPs in endosomal vesicles compared to GUVs can be attributed to their distinct composition and environment (e.g., presence of the plasma membrane and actin skeleton)[289]. Interestingly, the co-administration of CM_{18}-Tat_{11} and NPs shows no increase in toxicity. Although NPs are able to form pores both on external and on internal membranes, CM_{18}-Tat_{11} stabilizes only the latter and avoids any permanent damage at the level of the plasma membrane. Finally, based on atomistic MD simulations of planar POPC bilayer patches subjected to 10-ns pulses in the presence of the various peptides, light was shed on the molecular mechanism at the basis of the afore-mentioned cooperative perturbing action. In fact, MD data show that the CM_{18} module acts as a catalyst to stabilize the NP-elicited membrane defects, either alone or fused to Tat_{11}. The peptide (if located close enough to the pore mouth) can be electrophoretically dragged along the field direction into the hydrophilic pore while keeping its structural stability. As soon as the electric field is

switched off, the nanopore starts to collapse but the complete reversibility of the electroporation process is impaired by the persistency of CM_{18}-Tat_{11} peptide along the pore membrane. This property is not displayed by the Tat_{11} module, whose high electrophoretic mobility during NP administration (probably owing to Tat_{11} high positive charge) leads to rapid and complete peptide translocation.

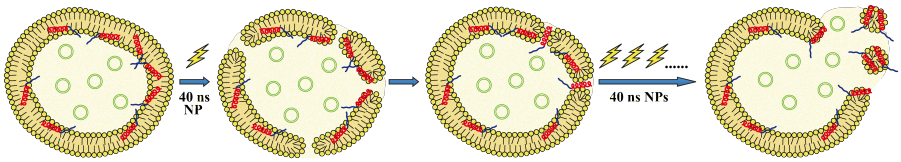

Fig. A.9 Schematic model of CM_{18}-Tat_{11} and NPs cooperative endosomal vesicle perturbation and pDNA release. CM_{18} α-helix is pictured in red, Tat_{11} unstructured coil is pictured in blue, while pDNA is in green. First endosomal vesicle shows the peptide accumulation on vesicle internal bilayer surface at low concentrations after the complex disassembling. In the second vesicle it is pictured the stochastic formation of nanopores after a single electric pulse administration to the cell, while in the third it is displayed how peptides, which are located on the edge of a nanopore defect in the bilayer after the electric field is switched off. The final outcome of multiple pulses administration is exhibited in the last vesicle picture where the proximity of several membrane defects leads to local bilayer micellization and release of pDNA molecules in the cytosolic lumen.

Based on the present data it can be proposed a mechanism (schematically pictured in Fig. A.7) where CM_{18}-Tat_{11} peptides first accumulate on the internal surface of the vesicle bilayer (following the endocytosis process). Then, NP-induced nanopores randomly form in different locations on the vesicle membrane. Each time a CM_{18}-Tat_{11} module falls close to the pore mouth, it can be elettrophoretically dragged into the pore lumen and thus fixes the defect. Multiple events eventually can lead to local bilayer micellization and release of pDNA molecules in the cytosolic lumen. These investigations, besides providing insights onto peptide-NP cooperation, enlighten the crucial role played by CM_{18} in the membrane destabilization process described throughout this thesis. In conclusion, this appendix shows for the first time that electric NPs can be successfully exploited for gene transfer applications through a co-administration with CM_{18}-Tat_{11} peptides at nanomolar concentration. I believe that this result can pave the way to further studies that combine external stimuli, like NPs, to peptidic vectors for targeted delivery.

Appendix

B

Methodological considerations

The material and methods employed for CM_{18}-Tat_{11} investigation are described comprehensively in this appendix for lightning the reading experience of the thesis chapters and of Appendix A.

B.1 Peptide synthesis, purification and labelling

All peptides were prepared by solid-phase synthesis using Fmoc chemistry on an automatic Liberty-12-Channel Automated Peptide Synthesizer with an integrated microwave system (CEM, North Carolina, USA). The crude peptides were purified by RP-HPLC on a Jupiter 4m Proteo 90 A column (250 × 10 mm; Phenomenex). The HPLC analysis and purification was performed on a Dionex Ultimate 3000 PLC system with autosampler. The correct purified product was confirmed by electrospray mass spectroscopy. The Cysteine residue added to the C-terminus of each peptide provided a sulfhydryl group for further ligation to the atto-633-maleimide fluorophore. The labeling of purified peptides was performed by incubating for 3 h with a 3-fold molar excess of atto-633-maleimide (ATTO-TEC GmbH, Germany), 150 mM PBS buffer, TCEP, at pH 7.4. Finally, atto-633-labeled peptides were purified by HPLC (see above) and then lyophilized overnight. The molecular weight of all conjugated-peptides was confirmed by electrospray mass

spectroscopy, and the concentration of each peptide stock solution was verified by UV-vis absorbance. The ESI-MS spectra of the peptides were obtained with an API3200QTRAP a Hybrid Triple Quadrupole/Linear Ion Trap (ABSciex, Foster City, California, USA). Peptides were stored at -80 °C.

B.2 CD measurements

CD spectra were recorded with a Jasco J-715 spectropolarimeter with the following conditions: speed 50 nm/min, resolution 1 nm, time response 1 sec, bandwidth 2.0 nm, using a 0.05/0.02 cm path cell, in spectroscopy grade THF. Peptides were at a concentration of about 0.1 mM (0.3-0.5 mg/ml) in PBS buffer pH 7.4 or 50% TFE in PBS. Secondary structure content was estimated via the CDSSTR program.

B.3 MD simulations

Molecular dynamics simulations of the CM_{18}-Tat_{11}peptide reported in chapter 2 were performed using the Duan et al. 2003 force field[294] in the Amber11 package[295]. The 50% (vol/vol) TFE/water mixture condition was simulated by solvating a randomly chosen configuration of the peptide in a truncated octahedron box of 870 TFE molecules and 3480 water molecules respectively, and using periodic boundary conditions. The force field for TFE was taken from ref.[296]. A total of 13 Cl- ions were added to the systems in order to neutralize the positive charges on the peptide. After constant pressure (1 atm) simulations to equilibrate the solvent, the lateral dimensions of the box reached the values of ~6.5nm, ensuring that even in the fully stretched configuration (very rarely reached, and only at the highest simulated temperatures) only limited contact was possible between peptide images. Extensive conformational exploration was achieved through the Replica Exchange Method[297] using 48 replicas with temperatures suitably chosen within an interval of 285 to 540 °K for a simulation time of 5ns, then reduced to 24 replicas within a 285-381 °K interval for the following 5ns. The SHAKE algorithm was used to constrain bonds involving hydrogen atoms, enabling the use of a 2-fs time step. The temperature was maintained using Langevin dynamics with a collision frequency of $2ps^{-1}$. Analysis of the trajectories was performed using the ptraj routine in AmberTools.

MD simulations for the NP/peptide interaction reported in App. A were performed as follows:

-System: The complete simulation system consists of a solvated membrane together with a CM_{18}-Tat_{11} peptide. The membrane model used for this study is an equilibrated fully-hydrated palmitoyl-oleoyl-phosphocholine (POPC) bilayer. In some occurrences, it contains a hydrophilic pore of initial diameter ~25 Å. It consists of 256 lipids units and roughly 22,400 water molecules organized in two lamellae above and below the lipids. At the temperature set for the study, *i.e.* 300 K, the bilayer is in the biologically-relevant liquid-crystal La phase. Three different systems were considered involving (a) CM_{18}-Tat_{11}, (b) only CM_{18} or (c) only Tat_{11}. The CM_{18}-Tat_{11} coordinates were taken from chapter 2 simulations and the peptide was set in two different configurations. Either just above the top membrane/solution interface or with the CM_{18} already adsorbed in the phosphate-glycerol region with the hydrophobic part looking toward the hydrophobic core and the hydrophilic moieties being in contact with the water region. For the anchored configurations, 7 lipid molecules were removed and the system was then equilibrated again. Same protocols were followed with the CM_{18}. A configuration with three peptides anchored instead of only one was built to test the concentration of peptide resulting in 21 lipid molecules being deleted. The Tat_{11} peptide was only placed in the solution at the interface between bulk water and the choline headgroups. To counterbalance the positive charge of the molecule, 13 chloride anions were added randomly to the solution for (a), 5 chloride anions for (b), and 7 chloride anions for (c). For configuration (a), simulation with an ionic concentration at 0.15M of NaCl was set up including 127 sodium cations and 140 chloride anions. When no electric field was applied, only counterions were present. The final dimensions of the system were 89 × 88 × 120 Å and the total number of atoms was roughly equal to 100,000 for all configurations.

-Simulations parameters: The MD simulation was carried out using the program NAMD2 targeted for massively-parallel architectures. The systems were examined at constant pressure and constant temperature (1 atm and 300 K) employing the Langevin dynamics and Langevin piston method. The equations of motion were integrated using the multiple time-step algorithm. A time-step of 2.0 fs was employed. Short- and long-range forces were calculated every 2 and 4 time steps, respectively. Chemical bonds between hydrogen and heavy atoms were constrained to their equilibrium value. Long-range, electrostatics forces were taken into account

using a fast implementation of the particle mesh Ewald (PME) method, with a direct space sum tolerance of 10^{-6} and a spherical truncation of 12 Å with a modified interaction potential through a switching distance of 10 Å. The water molecules were described using the TIP3P model. The parameters as implemented in the CHARMM36 version for the POPC lipid molecules and the CHARMM36 version for proteins[298] which treats more accurately proteins dynamics.

-Simulations protocols: The system was first equilibrated at constant temperature (300 K) and constant pressure (1 atm), using full 3D periodic boundary. Further simulations were performed using the standard "electric-field method" for which a constant electric field normal to the bilayer was applied to each particle of the system bearing a charge q_i of the system in the form of a force $F=q_i.E$, using 3D periodic boundary conditions. Using MD simulations, the value of the electric field that enables to porate the membrane is around 0.2 V/nm. Due to the length of the simulation box (120 Å), the transmembrane voltage amounts then to ~2.4 V. Compared to the field used in the experiments, it is one order of magnitude higher. Electric fields were applied for the three configurations (a), (b) and (c). For (a) and (b), the configuration with the CM_{18} anchored to the membrane was used as a starting point. However, due to the limitations of the simulation setup, fields of the magnitude actually used were not even able to maintain open an already formed pore, we could not simulate dynamics with a transmembrane voltage large enough to porate the membrane.

B.4 Bacterial killing assay

The bactericidal activity of the peptides against the laboratory standard strain (*Staphylococcus aureus*ATCC 33591) was evaluated by a liquid microdilution assay in 10 mM sodium phosphate buffer (SPB; pH 7.4), as previously described[299]. Briefly, *S. aureus* was grown in tryptone soy broth (TSB, Sigma). Exponentially growing bacteria were resuspended in SPB to obtain a density of $1x10^7$ colony forming units (CFUs)/ml. Ten microliters of each bacterial suspension were incubated at 37°C for 1 h in the presence of different concentrations of each peptide in 100 µl of SPB. Following incubation, samples were serially diluted in TSB to minimize the carryover effect and plated onto tryptone soy agar (Sigma) and the number of CFU was determined after 24 h of incubation at 37°C. The minimum

bactericidal concentration (MBC) was defined as the peptide concentration that causes 3 log10 CFUs/ml reduction in the number of viable bacteria.

B.5 Cell culture, transfections, viability tests and YO-PRO-1 membrane permeabilization analysis

HeLa, Chinese Hamster Ovary (CHO-K1), and Human Umbilical Vein Endothelial Cells (HUVEC) were purchased from ATCC and cultured following manufacturer's instructions. Cells were maintained at 37°C in a humidified 5% CO_2 atmosphere. For live cell microscopy cells were plated onto 35 mm glass-bottom petri dishes (WillCo-dish GWSt-3522) and imaged at 37 °C, 5% CO_2. Transfection of Tat_{11}-$EGFP^{178}$ and Caveolin-$E^{1}GFP^{300}$ plasmid was carried out using lipofectamine reagent (Invitrogen, Carlsbad CA) according to the manufacturer's instruction. To test cell viability, HeLa cells were incubated for 1 h at 37 °C with culture medium containing 8 μg/mL propidium iodide (PI) and increasing concentrations (from 4 to 256 μM) of each peptide. The medium was then discarded and the cells washed with PBS containing the same concentration of PI before confocal imaging. To test the effect of peptide treatment on cell metabolism we used the Wst-8 assay. In detail, HeLa cells were seeded onto 96-well plates, at $2x10^4$ cells/well, one day before treatment. Cells were treated with peptides in 100 μl medium with serum using the indicated concentrations for 1 hour. Cells were then exposed to the Wst-8 reagent according to the manufacturer's protocol (Sigma). Absorbance at 450 nm was measured 2 hours later on a Synergy HT multiplate reader (Bio Tek instruments). Untreated cells were defined as 100% viable, while cells exposed to 20% dimethyl sulfoxide (DMSO) for 1 hour were used as positive control. Cells exposed to the transfection protocol were also tested for membrane permeabilization using the YO-PRO-1 organic dye. YO-PRO-1 (5 μM) was administered to the medium of detached cells after transfection and its average fluorescence intensity per cell was evaluated by flow cytometry from 10.000 cells per sample 10 minutes after NP delivery.

B.6 Flow cytometry

HeLa cells were seeded 24 hours before the experiment in WillCo-dishes to reach a 70% confluence. For quantitative cellular uptake assays cells were treated with 0.1, 0.5, or 5 μM atto-633-labeled peptides. All treatments were performed in a total volume of 1 ml culture medium. After treatment, cells were washed three times in PBS buffer before trypsination for 1 minute in 0.25% trypsin solution (Invitrogen, Stockholm, Sweden). Cells were centrifuged at 1200 rpm for 5 minutes, and cell pellets dissolved in 500 μl PBS before cytometry measurement. Internalization of labeled peptides into cells was evaluated with a 635nm excitation laser (filter 655-730). For the quantitative cellular uptake assay, results for each peptide treatment were expressed as "normalized uptake" (i.e. the mean fluorescence value obtained from each sample divided by the one retrieved from CM-treated cells). For all the tested peptides, N=3 independent experiments were conducted, each of which in triplicate. For the quantification of Calcein release from endosomes, cells were treated with 250 μM Calcein± 0.5 μM of each peptide. Cells were excited at 488 nm and green fluorescence was collected using a 530 ± 30 nm band-pass filter. Results were expressed in a plot of the normalized cell number against cell-fluorescence counts. The mean intracellular fluorescence of N=50 cells with detectable Calcein release was quantified and divided by that of an equal number of control cells (those with only punctate fluorescence). The retrieved average fluorescence ratio of ~2.5 was used as a threshold-value to quantify the percentage of positive 'Calcein-releasing' cells in the sample. MACSQuant® analyzer was used to run samples and MACSQuantify software to analyze data. 1.5x103 cells per sample were acquired in triplicate and at least 4 independent experiments were performed.

B.7 Confocal microscopy and image analysis

Confocal laser scanning microscopy (CLSM) experiments reported in chapter 2 were performed with the Olympus Fluoview 1000 (Olympus, Melville, NY) confocal microscope interfaced with a 488nm Argon laser, a 543nm helium-neon laser, and a 633 nm diode laser. Glass-bottom Petri dishes containing plated cells were mounted in a temperature-controlled chamber at 37 °C and 5% CO2 and viewed with a 60 X 1.25 numerical aperture water-immersion objective. The following collection ranges were adopted: 500-540 nm (EGFP, Calcein, 3/10-kDa

Rhodamine green-dextrans, and 40-kDa fluorescein isothiocyanate (FITC)-dextrans), 550-600 nm (PI) and 650-750 (atto-633-labelled peptides). In a typical two-channel experiment images were collected in sequential mode to eliminate emission cross talk or bleed through between the various dyes. Photobleaching experiments for the analysis of Calcein release kinetics started with a six-time line-averaged image of the cell followed by a single-point bleaching (non-scanning) near the center of the nucleus with a 488nm laser pulse at full power for the minimum time required to photobleach all cell fluorescence except for the vesicular signal. Recovery was measured by starting a time-lapse acquisition within a few milliseconds from the end of bleaching (sampling rate has been tailored to the speed of the Calcein fluorescence recovery). All data collected were analyzed by ImageJ software version 1.37 (NIH Image; http://rsbweb.nih.gov/ij/). For each experiment, a region of interest (ROI) was selected inside the cell to calculate the mean increase in Calcein fluorescence. A ROI drawn outside the cell was used to calculate (and then subtract) the average background signal. Corrected intracellular fluorescence values were expressed in arbitrary units and plotted against time.

CLSM experiments reported in chapter 3 were performed using a Leica TCS SP5 inverted confocal microscope (Leica Microsystems AG, Wetzlar, Germany), interfaced with a He-Ne laser for excitation at 561 and 633 nm. Glass-bottom petri dishes containing transfected cells were mounted in a thermostated chamber (Leica Microsystems) and viewed with a 40×1.25 numerical aperture oil immersion objective (Leica Microsystems). Live cell imaging was always performed at 37 °C. Emission was monitored by means of the Acousto-Optical Beam Splitter (AOBS)-based built-in detectors of the confocal microscope. The following collection ranges were adopted: 460-530 nm (Lysosensor), 570-610 nm (Cy3), and 650-750 nm (atto-633). For FRET imaging, I did not acquire the sensitized-emission channel (excitation: 543 nm, collection 650-750 nm) because it is not ideal for monitoring the complex stability due to the co-presence of some external contributions, as atto-633 own excitation at 540 nm and DNA quenching effect. In a typical two-channel experiment images were collected in sequential mode to eliminate emission cross talk or bleed through between the various dyes. Acceptor photobleaching experiments for the analysis of complex integrity inside cell vesicles started with an eight-time line-averaged image of the cell followed by a scanning bleaching of the whole cell with a 633 nm laser at full power for the minimum time required to

photobleach the vesicular fluorescence signal in the second channel. After the bleaching I took a new eight-time line-averaged image of the cell for both channels.

B.8 Recombinant Tat_{11}-EGFP purification

The Tat_{11}-EGFP coding sequence was obtained by digestion of Tat_{11}-EGFP fragment from the pGEX2T-GST-Tat EGFP plasmid[300] with *BamHI* and *EcoRI* restriction endonucleases and cloned into the *BamHI* and *EcoRI*sites of the pGEX-6P-1 GST expression vector (GE Healthcare, Waukesha, WI, USA). Recombinant Tat_{11}-EGFP protein was expressed in *E. coli* BL21(DE3) strain (Invitrogen) and purified by affinity chromatography using Glutathione Sepharose 4B medium packed into gravity flow columns as indicated by the manufacturer (GE Healthecare Waukesha, WI, USA). Briefly, bacteria grown at 37°C until mid-log phase were induced by adding 1 mM isopropyl-ß-D-galactoside (IPTG) and incubated for an additional 4 h. The binding of the protein to the column was performed in PBS and the elution was carried out in 50 mMTris-HCl buffer, 150 mMNaCl, 1 mM EDTA, 1 mM DTT (ph 7.5) treatment with a Prescission TM Protease (GE Healthcare) overnight at 4°C.

B.9 Co-localization studies and cargo-delivery assays

In order to characterize the endocytic process involved in CM_{18}-Tat_{11} internalization we performed colocalization assays in living cells. HeLa cells were coincubated for 30 minutes at 37°C with 0.5 µM atto-633-labeled CM_{18}-Tat_{11} (as described above) and different dyes: 1 mg/ml FITC-dextran 70-kd (Sigma Genosys) to label macropinosomes, or 75 nM lysotracker (Invitrogen, Stockholm, Sweden) to label lysosomes. After incubation, cells were washed three times with PBS and examined at the confocal microscope. For a typical cargo-delivery assay, cells were seeded 24 hours before the experiment in WillCo-dishes to reach a 70% confluence. At the time of the experiment we added the cargo to be delivered (typically 5 µM of Tat_{11}-EGFP, 250 µM of Calcein, or 1 mg/mL of fluorescently labeled 3, 10, and 40-kDa dextrans) and a known concentration of the peptide to be tested (e.g. CM_{18}-Tat_{11} 0.5 µM). After 30 minutes (1 hour for Tat_{11}-EGFP) of incubation at 37 °C, cells were washed three times with PBS and then analyzed by confocal microscopy. We evaluated co-treatment (i.e. simultaneous incubation of cells with cargo

molecule and peptide) and time-shifted treatment (i.e. incubation of cells with the molecule, imaging, and then incubation of the same cells with the peptide): both yielded the same delivery results. For the DNA delivery assay we used a transfection solution (80% cell-growth medium without serum, 20% PBS) containing 1 μg/ml of pCMV-GLuc Control pDNA (New England BioLabs, Hitchin, UK) encoding for a secretable Gaussia Luciferase and 1.4 μM of Tat_{11} peptide. Cells were seeded in 96-well plates 24 h prior to the transfection experiment. The growth medium in the wells was replaced with the transfection solution and 1 μM of Tat_{11} (or CM_{18}-Tat_{11}) was added after 30 minutes. 6 hours later the transfection medium was replaced by fresh serum-containing medium and the cells were further incubated for 24 h. As a positive control, transfection of the luciferase DNA was also performed by using DOTAP/DOPC lipid formulations, as described previously[301]. The luciferase activity was measured from an aliquot of the external medium by using an assay kit from New England Biolabs and an injector-equipped Veritas microplate luminometer (Turner BioSystems, Sunnyvale, CA). The unit RLU/well was used to present the most accurate expression level in this experimental system[226]. The above-mentioned Tat_{11}:DNA complex was also produced using a Cy3 labeled pDNA (Mirus, Piscataway, NJ) in order to evaluate the complex cellular localization by means of fluorescence confocal microscopy.

B.10 Transfection vectors.

pCMV-GLuc 2 control plasmid (5.7 kb, 3700 kDa; New England Biolabs, Ipswich, MA) was used as a reporter gene. pCMV-GLuc 2 control plasmid was first transformed in One Shot TOP 10 chemically competent Escherichia coli and then was amplified in Luria Bertani broth media at 37 °C overnight. After that, a Plasmid Maxi Kit (Qiagen, Valencia, CA) was used for purification of the plasmid. The purified pDNA was dissolved in water at 1 μg/μl concentration and stored at -20 °C before use. Label IT® Cy3 plasmid delivery control (2.7 kb, 1730 kDa; Mirus Bio Corporation, Madison, WI) was used for confocal fluorescence microscopy experiments and agarose gel electrophoresis.

Peptide/pDNA binary complexes were prepared as follows: 1 μg of pDNA was dissolved in 200 μl of PBS solution and different volumes of the peptide solution were added to obtain the desired N:P molar ratio. The mixture was then incubated at

room temperature for 30 minutes. Finally, the transfection medium was added till 1 ml total volume (i.e. in CM_{18}-Tat_{11}:DNA complex 4:1, concentrations are 0.8 μM peptide and 0.3 nM DNA).

B.11 In vitro DNA transfection

Cells were plated in a 96-well plate at a density of 8×10^4 cells/ml, cultivated in growth medium with 10% FBS. 100 μl of medium were added to each well. After 24 hours the growth medium in each well was replaced with 100 μl transfection medium containing peptide/pDNA binary complexes. Incubation with the cells lasted 6 hours at 37 °C. Then, 200 μl growth medium replaced the transfection medium and cells were cultured for 24 hours at 37 °C in 5% (v/v) CO_2 after transfection. All transfection assays were carried out three times and each in sestuplicate simultaneously. For control lipid transfection Lipofectamine (Invitrogen, Carlsbad, CA) was used according to the manufacturer's instruction. For confocal live scanning microscopy (CLSM) cells were plated onto 35 mm glass-bottom petri dishes (WillCo-dish GWSt-3522) the day before the experiment to reach 70% confluence. After 24 hours growth cells medium was replaced with 1 ml transfection medium containing CM_{18}-Tat_{11}-atto633/Cy3-pDNA binary complexes at N:P ratio 16/1 prepared as explained in Sec. B.10. Incubation with the cells lasted 6 hours at 37 °C. Then we replaced transfection medium with growth medium. Transgene expression was detected 24 hours after transfection. The luciferase activity was measured from an aliquot of the external medium by using an assay kit from New England Biolabs and an injector-equipped Veritas microplate luminometer (Turner BioSystems, Sunnyvale, CA). The RLU/well unit was used to present the most accurate expression level in this experimental system.

B.12 EtBr exclusion assay.

DNA condensation was analyzed using an EtBr (Sigma, Taufkirchen, Germany) exclusion assay. Briefly, complexes were formed as described above in Sec. B.10. After 1 hour incubation, each sample was transferred into a black 96-well plate. Thereafter, 3.2 μl of EtBr solution was added to give a final EtBr concentration of 400nmol/l. After 10 minutes, fluorescence was measured on a Synergy HT multiplate reader (Bio Tek instruments) at λ_{ex} = 525nm and λ_{em} = 620nm. Results

are given as relative fluorescence and a value of 100% is attributed to the fluorescence of naked DNA with EtBr. The same assay was repeated in a 24 hours time-lapse incubating 1:16 N:P ratio CM_{18}-Tat_{11}/pDNA binary complexes in different solutions at 37°C: PBS buffer at pH=7.4 ± cathepsin B enzyme (Sigma-Aldrich, 10mU), PBS buffer at pH=6.5 (by addition of HCl) ± cathepsin B enzyme, PBS buffer at pH=5.5 or PBS buffer at pH=4.5.

B.13 Agarose gel electophoresis.

The stabilities of CM_{18}-Tat_{11}/pDNA binary complexes with different N:P ratio were evaluated by agarose gel electrophoresis assay. In brief 2 μL DNA Cy3 plasmid solution was mixed with the vector solutions at different N:P ratios in 200 μl PBS as final volume. The system incubated at 37 °C for 30 minutes. After complexes (50 μl per well) were electrophoresed on the 0.8% (w/v) agarose gel with TBE running buffer at 80 V for 40 minutes, an ImageQuant LAS 4000 biomolecular imager (GE Healthcare, Madison, WI) was used for the visualization of DNA position inside the gel. Naked DNA Cy3 plasmid was used as control.

B.14 Particle size and ζ-potential measurements.

Particle size and ζ-potentials of CM_{18}-Tat_{11}/pDNA binary complexes with different N:P ratios were measured at 25 °C by a Zetasizer Nano ZS90 (Malvern Instruments Ltd., UK) instrument equipped with a red laser of wavelength 630 nm. All the complexes were prepared using pCMV-GLuc 2 control plasmid in a total volume of 1 ml of PBS. Each sample was observed with 20 repeated measurements across 3 trials. Error bars in figures indicate standard deviations.

B.15 *In vitro* spectroscopic Förster Resonance Energy Transfer (FRET) measurements.

Fluorescence spectra were recorded at 37 °C on a Cary Eclipse spectrofluorometer (Varian) by setting the excitation and emission monochromator slits both to 5 nm;

the scanning speed was set to 120 nm/min, and data resolution to 1 nm. Emission spectra were recorded by exciting at 540 nm and collecting the fluorescence between 550 and 800 nm. First, a fluorescence emission measurement was performed on a PBS solution of Cy3-labeled pDNA alone. Then, atto633-labeled peptide at N:P ratio 16:1 was added, and the 550-800-nm emission spectrum recorded. FRET can be unequivocally measured by the extent of donor-emission quenching, as this depends only on donor-acceptor proximity in the complex (addition of unlabeled peptide does not affect donor emission). On the contrary, acceptor fluorescence does not only depend on the extent of its sensitized emission (FRET) but also on the sum of acceptor cross-excitation at 540 and acceptor quenching due to DNA binding (unlabeled plasmid is able to quench atto633-peptide fluorescence; data not shown).

B.16 GUVs preparation

1,2-Dioleoyl-sn-glycero-3-phosphocholine (DOPC) and 1,2-dioleoyl-*sn*-glycero-3-phosphoethanolamine-N-(lissamine rhodamine B sulfonyl) ammonium salt (DOPE-Rhodamine) were purchased from Avanti Polar Lipids (Alabaster, AL). DOPC was dissolved in chloroform at a mass concentration of 0.5 mg/mL. The dye DOPE-Rhodamine was added at a 1% molar concentration and the solution was stored at -20°C. Vesicles were prepared at 6°C using the electroformation protocol described by Angelova[290]. 15 μL of the lipid solution were deposited on the conducting side of two glass slides coated with indium tin oxide (Sigma, Saint Louis, MO). Slides were then kept under vacuum for two hours in a desiccator to remove all traces of organic solvent. A chamber was assembled with the slides spaced by a 1.5 mm silicone isolator (Sigma, Saint Louis, MO). The chamber was filled with a sucrose solution (240 mM sucrose, 1mM NaCl, 1mM KH_2PO_4/K_2HPO_4). The slides were connected to a function/arbitrary waveform generator (HP Agilent 33120A, Santa Clara, CA) and sinusoidal voltage of 25 mV peak to peak and 8 Hz was applied. The voltage was increased by 100 mV steps every 5 minutes, up to a value of 1225 mV and maintained under these conditions overnight. Finally, square-wave AC field of the same amplitude was applied at 4 Hz for one hour in order to detach the GUVs from the slides.

B.17 Vesicles exposure to electric pulses and/or peptides

20 µL of the GUVs solution were mixed with different amount of peptide (CM_{18}-Tat_{11}, CM_{18}, orTat_{11}) solution in sucrose buffer with a final volume of 200 µL. A control solution was also prepared with 20 µL of the GUVs solution and 180 µL of sucrose buffer. These preparations were transferred in conventional electroporation cuvettes (STD, Dutcher, Issy les Moulineaux, France). The distance between the two planar electrodes of the cuvette was d =0.1 cm. A number of 10 ns pulses (between 1 and 100) was then applied to the cuvette. A commercial generator purchased from FID (FID GmbH, Model FPG 10-ISM10, Burbach, Germany) with an output impedance of 50 Ω was used. It generates trapezoidal monopolar pulses with a full-width at half maximum of 10 ns. The output voltages applied were U = 0.5 kV, U = 2 kV and U = 6kV. This set-up was previously described by Silve et al.[302].

B.18 GUVs stability qualitative and quantitative assay

GUVs populations exposed to 1 µM concentrations of dye-labeled CM_{18}-Tat_{11} CM_{18} or Tat_{11} with or without 10-ns-long NPs were analyzed qualitatively by depositing the solution inside a chamber consisting of a glass coverslip mounted onto a glass slide with heated parafilm. All images were obtained with an inverted confocal microscope (Zeiss LSM510 ; Carl Zeiss, Jena, Germany) equipped with an objective Plan Apochromat 63x/ ON 1.4. For the red channel (Rhodamine-labeled vesicles) excitation wavelength was 543 nm and the emission filter was a 560 nm long pass. For the green channel (atto-495 peptide), excitation wavelength was 488 nm and the emission filter was a 500-530 band pass.

For the quantitative assays, the vesicle solution after pulse delivery or peptide exposure only was examined by flow cytometry on a BD Accuri C6 flow cytometer (BD Biosciences) to evaluate the number of stable GUVs through the analysis of event numbers inside a selected region of interest (ROI, obtained from stables vesicles solution) in the vesicle distribution graph (y FSC-A: size; x FL2-A: rhodamine signal) using the BD Accuri CFlow Plus software. Destabilized, collapsed vesicles were detected as debris components (falling out of the ROI) by the cytometer analysis. Thus, in order to evaluate the % of stable GUV in a sample, we measured the ratio between the ROI event number of treated and control

samples. GUVs exposed to 0.005% solution of commercial surfactant Triton X-100 (Sigma-Aldrich, Buchs, Switzerland) were used as positive control.

Bibliography

1 Medina-Kauwe, L. K., Xie, J. & Hamm-Alvarez, S. Intracellular trafficking of nonviral vectors. *Gene Ther* **12**, 1734-1751, (2005).

2 Tagami, T., Barichello, J. M., Kikuchi, H., Ishida, T. & Kiwada, H. The gene-silencing effect of siRNA in cationic lipoplexes is enhanced by incorporating pDNA in the complex. *Int J Pharm* **333**, 62-69, (2007).

3 Son, Y. J. *et al.* Biodistribution and anti-tumor efficacy of doxorubicin loaded glycol-chitosan nanoaggregates by EPR effect. *J Control Release* **91**, 135-145, (2003).

4 Schweichel, D. *et al.* Evaluation of DNA vaccination with recombinant adenoviruses using bioluminescence imaging of antigen expression: impact of application routes and delivery with dendritic cells. *J Gene Med* **8**, 1243-1250, (2006).

5 Xiang, S. *et al.* Uptake mechanisms of non-viral gene delivery. *J Control Release* **158**, 371-378, (2012).

6 Belting, M., Sandgren, S. & Wittrup, A. Nuclear delivery of macromolecules: barriers and carriers. *Adv Drug Deliv Rev* **57**, 505-527, (2005).

7 Torchilin, V. P. Recent approaches to intracellular delivery of drugs and DNA and organelle targeting. *Annu Rev Biomed Eng* **8**, 343-375, (2006).

8 El-Sayed, A. & Harashima, H. Endocytosis of gene delivery vectors: from clathrin-dependent to lipid raft-mediated endocytosis. *Mol Ther* **21**, 1118-1130, (2013).

9 Doherty, G. J. & McMahon, H. T. Mechanisms of endocytosis. *Annu Rev Biochem* **78**, 857-902, (2009).

10 Mercer, J., Schelhaas, M. & Helenius, A. Virus entry by endocytosis. *Annu Rev Biochem* **79**, 803-833, (2010).

11 Gruenberg, J. & van der Goot, F. G. Mechanisms of pathogen entry through the endosomal compartments. *Nat Rev Mol Cell Biol* **7**, 495-504, (2006).

12 Tauber, A. I. Metchnikoff and the phagocytosis theory. *Nat Rev Mol Cell Biol* **4**, 897-901, (2003).

13 Duncan, R. & Richardson, S. C. Endocytosis and intracellular trafficking as gateways for nanomedicine delivery: opportunities and challenges. *Mol Pharm* **9**, 2380-2402, (2012).

14 Canton, I. & Battaglia, G. Endocytosis at the nanoscale. *Chemical Society reviews* **41**, 2718-2739, (2012).

15 Fonseca, S. B., Pereira, M. P. & Kelley, S. O. Recent advances in the use of cell-penetrating peptides for medical and biological applications. *Adv Drug Deliv Rev* **61**, 953-964, (2009).

16 Herzog, M., Gerard, D., Hirth, L. & Laustriat, G. Natural fluorescence properties of brome mosaic virus protein. *Biochim Biophys Acta* **493**, 167-177, (1977).

17 Johnson, M. H. The distribution of a blastokinin-like uterine protein studied by immune fluorescence. *Fertil Steril* **23**, 929-939, (1972).

18 Vida, T. & Gerhardt, B. A cell-free assay allows reconstitution of Vps33p-dependent transport to the yeast vacuole/lysosome. *J Cell Biol* **146**, 85-98, (1999).

19 Hurley, J. H., Boura, E., Carlson, L. A. & Rozycki, B. Membrane budding. *Cell* **143**, 875-887, (2010).

20 Russell, M. R., Nickerson, D. P. & Odorizzi, G. Molecular mechanisms of late endosome morphology, identity and sorting. *Curr Opin Cell Biol* **18**, 422-428, (2006).

21 Scott, C. C. & Gruenberg, J. Ion flux and the function of endosomes and lysosomes: pH is just the start: the flux of ions across endosomal membranes influences endosome function not only through regulation of the luminal pH. *BioEssays : news and reviews in molecular, cellular and developmental biology* **33**, 103-110, (2011).

22 Saftig, P. & Klumperman, J. Lysosome biogenesis and lysosomal membrane proteins: trafficking meets function. *Nat Rev Mol Cell Biol* **10**, 623-635, (2009).

23 Marino, G., Madeo, F. & Kroemer, G. Autophagy for tissue homeostasis and neuroprotection. *Curr Opin Cell Biol* **23**, 198-206, (2011).

24 Underhill, D. M. & Goodridge, H. S. Information processing during phagocytosis. *Nature reviews. Immunology* **12**, 492-502, (2012).

25 Couzinet, S. *et al.* Phagocytic uptake of Encephalitozoon cuniculi by nonprofessional phagocytes. *Infect Immun* **68**, 6939-6945, (2000).

26 Chen, Q., Stone, P. R., McCowan, L. M. & Chamley, L. W. Phagocytosis of necrotic but not apoptotic trophoblasts induces endothelial cell activation. *Hypertension* **47**, 116-121, (2006).

27 Fadok, V. A. *et al.* A receptor for phosphatidylserine-specific clearance of apoptotic cells. *Nature* **405**, 85-90, (2000).

28 Swanson, J. A. Shaping cups into phagosomes and macropinosomes. *Nat Rev Mol Cell Biol* **9**, 639-649, (2008).

29 Hillaireau, H. & Couvreur, P. Nanocarriers' entry into the cell: relevance to drug delivery. *Cell Mol Life Sci* **66**, 2873-2896, (2009).

30 Kerr, M. C. & Teasdale, R. D. Defining macropinocytosis. *Traffic* **10**, 364-371, (2009).

31 Mercer, J. & Helenius, A. Virus entry by macropinocytosis. *Nat Cell Biol* **11**, 510-520, (2009).

32 Orth, J. D. & McNiven, M. A. Get off my back! Rapid receptor internalization through circular dorsal ruffles. *Cancer Res* **66**, 11094-11096, (2006).

33 Schafer, D. A., D'Souza-Schorey, C. & Cooper, J. A. Actin assembly at membranes controlled by ARF6. *Traffic* **1**, 892-903, (2000).

34 Nobes, C. & Marsh, M. Dendritic cells: new roles for Cdc42 and Rac in antigen uptake? *Curr Biol* **10**, R739-741, (2000).

35 Doherty, G. J. & McMahon, H. T. Mediation, modulation, and consequences of membrane-cytoskeleton interactions. *Annual review of biophysics* **37**, 65-95, (2008).

36 Mercer, J. & Helenius, A. Vaccinia virus uses macropinocytosis and apoptotic mimicry to enter host cells. *Science* **320**, 531-535, (2008).

37 Mercer, J. & Helenius, A. Gulping rather than sipping: macropinocytosis as a way of virus entry. *Current opinion in microbiology* **15**, 490-499, (2012).

38 Racoosin, E. L. & Swanson, J. A. Macropinosome maturation and fusion with tubular lysosomes in macrophages. *J Cell Biol* **121**, 1011-1020, (1993).

39 Kerr, M. C. *et al.* Visualisation of macropinosome maturation by the recruitment of sorting nexins. *J Cell Sci* **119**, 3967-3980, (2006).

40 Kasahara, K. *et al.* Role of Src-family kinases in formation and trafficking of macropinosomes. *J Cell Physiol* **211**, 220-232, (2007).

41 Liu, N. Q. *et al.* Human immunodeficiency virus type 1 enters brain microvascular endothelia by macropinocytosis dependent on lipid rafts and the mitogen-activated protein kinase signaling pathway. *J Virol* **76**, 6689-6700, (2002).

42 Hamasaki, M., Araki, N. & Hatae, T. Association of early endosomal autoantigen 1 with macropinocytosis in EGF-stimulated A431 cells. *The anatomical record. Part A, Discoveries in molecular, cellular, and evolutionary biology* **277**, 298-306, (2004).

43 Cavalli, V., Corti, M. & Gruenberg, J. Endocytosis and signaling cascades: a close encounter. *FEBS Lett* **498**, 190-196, (2001).

44 McMahon, H. T. & Boucrot, E. Molecular mechanism and physiological functions of clathrin-mediated endocytosis. *Nat Rev Mol Cell Biol* **12**, 517-533, (2011).

45 Bretscher, M. S. Endocytosis: relation to capping and cell locomotion. *Science* **224**, 681-686, (1984).

46 Smith, C. J., Grigorieff, N. & Pearse, B. M. Clathrin coats at 21 A resolution: a cellular assembly designed to recycle multiple membrane receptors. *EMBO J* **17**, 4943-4953, (1998).

47 Conner, S. D. & Schmid, S. L. Regulated portals of entry into the cell. *Nature* **422**, 37-44, (2003).

48 Huotari, J. & Helenius, A. Endosome maturation. *EMBO J* **30**, 3481-3500, (2011).

49 Naslavsky, N., Weigert, R. & Donaldson, J. G. Characterization of a nonclathrin endocytic pathway: membrane cargo and lipid requirements. *Mol Biol Cell* **15**, 3542-3552, (2004).

50 Smart, E. J. *et al.* Caveolins, liquid-ordered domains, and signal transduction. *Mol Cell Biol* **19**, 7289-7304, (1999).

51 Rothberg, K. G. *et al.* Caveolin, a protein component of caveolae membrane coats. *Cell* **68**, 673-682, (1992).

52 Pelkmans, L. & Helenius, A. Endocytosis via caveolae. *Traffic* **3**, 311-320, (2002).

53 Pelkmans, L. & Zerial, M. Kinase-regulated quantal assemblies and kiss-and-run recycling of caveolae. *Nature* **436**, 128-133, (2005).

54 Das, K., Lewis, R. Y., Scherer, P. E. & Lisanti, M. P. The membrane-spanning domains of caveolins-1 and -2 mediate the formation of caveolin hetero-oligomers. Implications for the assembly of caveolae membranes in vivo. *J Biol Chem* **274**, 18721-18728, (1999).

55 Hill, M. M. *et al.* PTRF-Cavin, a conserved cytoplasmic protein required for caveola formation and function. *Cell* **132**, 113-124, (2008).

56 Pelkmans, L., Kartenbeck, J. & Helenius, A. Caveolar endocytosis of simian virus 40 reveals a new two-step vesicular-transport pathway to the ER. *Nat Cell Biol* **3**, 473-483, (2001).

57 Hayer, A. *et al.* Caveolin-1 is ubiquitinated and targeted to intralumenal vesicles in endolysosomes for degradation. *J Cell Biol* **191**, 615-629, (2010).

58 Engel, S. *et al.* Role of endosomes in simian virus 40 entry and infection. *J Virol* **85**, 4198-4211, (2011).

59 Simionescu, M., Popov, D. & Sima, A. Endothelial transcytosis in health and disease. *Cell and tissue research* **335**, 27-40, (2009).

60 Stuermer, C. A. The reggie/flotillin connection to growth. *Trends Cell Biol* **20**, 6-13, (2010).

61 Riento, K., Frick, M., Schafer, I. & Nichols, B. J. Endocytosis of flotillin-1 and flotillin-2 is regulated by Fyn kinase. *J Cell Sci* **122**, 912-918, (2009).

62 Babuke, T. *et al.* Hetero-oligomerization of reggie-1/flotillin-2 and reggie-2/flotillin-1 is required for their endocytosis. *Cellular signalling* **21**, 1287-1297, (2009).

63 Langhorst, M. F. *et al.* Trafficking of the microdomain scaffolding protein reggie-1/flotillin-2. *Eur J Cell Biol* **87**, 211-226, (2008).

64 Payne, C. K., Jones, S. A., Chen, C. & Zhuang, X. Internalization and trafficking of cell surface proteoglycans and proteoglycan-binding ligands. *Traffic* **8**, 389-401, (2007).

65 Kirkham, M. *et al.* Ultrastructural identification of uncoated caveolin-independent early endocytic vehicles. *J Cell Biol* **168**, 465-476, (2005).

66 D'Souza-Schorey, C. & Chavrier, P. ARF proteins: roles in membrane traffic and beyond. *Nat Rev Mol Cell Biol* **7**, 347-358, (2006).

67 Lundmark, R. *et al.* The GTPase-activating protein GRAF1 regulates the CLIC/GEEC endocytic pathway. *Curr Biol* **18**, 1802-1808, (2008).

68 Doherty, G. J. & Lundmark, R. GRAF1-dependent endocytosis. *Biochem Soc Trans* **37**, 1061-1065, (2009).

69 Howes, M. T. *et al.* Clathrin-independent carriers form a high capacity endocytic sorting system at the leading edge of migrating cells. *J Cell Biol* **190**, 675-691, (2010).

70 Kalia, M. *et al.* Arf6-independent GPI-anchored protein-enriched early endosomal compartments fuse with sorting endosomes via a Rab5/phosphatidylinositol-3'-kinase-dependent machinery. *Mol Biol Cell* **17**, 3689-3704, (2006).

71 Gauthier, N. C. *et al.* Helicobacter pylori VacA cytotoxin: a probe for a clathrin-independent and Cdc42-dependent pinocytic pathway routed to late endosomes. *Mol Biol Cell* **16**, 4852-4866, (2005).

72 D'Souza-Schorey, C., Li, G., Colombo, M. I. & Stahl, P. D. A regulatory role for ARF6 in receptor-mediated endocytosis. *Science* **267**, 1175-1178, (1995).

73 Paleotti, O. *et al.* The small G-protein Arf6GTP recruits the AP-2 adaptor complex to membranes. *J Biol Chem* **280**, 21661-21666, (2005).

74 Donaldson, J. G. & Radhakrishna, H. Expression and properties of ADP-ribosylation factor (ARF6) in endocytic pathways. *Methods Enzymol* **329**, 247-256, (2001).

75 Blagoveshchenskaya, A. D., Thomas, L., Feliciangeli, S. F., Hung, C. H. & Thomas, G. HIV-1 Nef downregulates MHC-I by a PACS-1- and PI3K-regulated ARF6 endocytic pathway. *Cell* **111**, 853-866, (2002).

76 Radhakrishna, H. & Donaldson, J. G. ADP-ribosylation factor 6 regulates a novel plasma membrane recycling pathway. *J Cell Biol* **139**, 49-61, (1997).

77 Naslavsky, N., Weigert, R. & Donaldson, J. G. Convergence of non-clathrin- and clathrin-derived endosomes involves Arf6 inactivation and changes in phosphoinositides. *Mol Biol Cell* **14**, 417-431, (2003).

78 Lau, A. W. & Chou, M. M. The adaptor complex AP-2 regulates post-endocytic trafficking through the non-clathrin Arf6-dependent endocytic pathway. *J Cell Sci* **121**, 4008-4017, (2008).

79 Ridley, A. J. Signalling by Rho family proteins. *Biochem Soc Trans* **25**, 1005-1010, (1997).

80 Zhang, B. & Zheng, Y. Regulation of RhoA GTP hydrolysis by the GTPase-activating proteins p190, p50RhoGAP, Bcr, and 3BP-1. *Biochemistry* **37**, 5249-5257, (1998).

81 Li, R., Zhang, B. & Zheng, Y. Structural determinants required for the interaction between Rho GTPase and the GTPase-activating domain of p190. *J Biol Chem* **272**, 32830-32835, (1997).

82 Kumari, S., Mg, S. & Mayor, S. Endocytosis unplugged: multiple ways to enter the cell. *Cell research* **20**, 256-275, (2010).

83 Dalton, P. D., Lleixa Calvet, J., Mourran, A., Klee, D. & Moller, M. Melt electrospinning of poly-(ethylene glycol-block-epsilon-caprolactone). *Biotechnology journal* **1**, 998-1006, (2006).

84 Grafahrend, D. *et al.* Control of protein adsorption on functionalized electrospun fibers. *Biotechnology and bioengineering* **101**, 609-621, (2008).

85 Lamaze, C., Chuang, T. H., Terlecky, L. J., Bokoch, G. M. & Schmid, S. L. Regulation of receptor-mediated endocytosis by Rho and Rac. *Nature* **382**, 177-179, (1996).

86 Johannes, L. & Lamaze, C. Clathrin-dependent or not: is it still the question? *Traffic* **3**, 443-451, (2002).

87 Padari, K. *et al.* Cell transduction pathways of transportans. *Bioconjug Chem* **16**, 1399-1410, (2005).

88 Laufer, S. D. & Restle, T. Peptide-mediated cellular delivery of oligonucleotide-based therapeutics in vitro: quantitative evaluation of overall efficacy employing easy to handle reporter systems. *Curr Pharm Des* **14**, 3637-3655, (2008).

89 Ciftci, K. & Levy, R. J. Enhanced plasmid DNA transfection with lysosomotropic agents in cultured fibroblasts. *Int J Pharm* **218**, 81-92, (2001).

90 Shiraishi, T., Pankratova, S. & Nielsen, P. E. Calcium ions effectively enhance the effect of antisense peptide nucleic acids conjugated to cationic tat and oligoarginine peptides. *Chem Biol* **12**, 923-929, (2005).

91 Abes, S. *et al.* Vectorization of morpholino oligomers by the (R-Ahx-R)4 peptide allows efficient splicing correction in the absence of endosomolytic agents. *J Control Release* **116**, 304-313, (2006).

92 Pack, D. W., Putnam, D. & Langer, R. Design of imidazole-containing endosomolytic biopolymers for gene delivery. *Biotechnology and bioengineering* **67**, 217-223, (2000).

93 Yang, L., Harroun, T. A., Weiss, T. M., Ding, L. & Huang, H. W. Barrel-stave model or toroidal model? A case study on melittin pores. *Biophys J* **81**, 1475-1485, (2001).

94 Neu, M., Fischer, D. & Kissel, T. Recent advances in rational gene transfer vector design based on poly(ethylene imine) and its derivatives. *J Gene Med* **7**, 992-1009, (2005).

95 Miller, D. K., Griffiths, E., Lenard, J. & Firestone, R. A. Cell killing by lysosomotropic detergents. *J Cell Biol* **97**, 1841-1851, (1983).

96 Koltover, I., Salditt, T., Radler, J. O. & Safinya, C. R. An inverted hexagonal phase of cationic liposome-DNA complexes related to DNA release and delivery. *Science* **281**, 78-81, (1998).

97 Tamm, L. K. & Han, X. Viral fusion peptides: a tool set to disrupt and connect biological membranes. *Bioscience reports* **20**, 501-518, (2000).

98 Daleke, D. L. Regulation of transbilayer plasma membrane phospholipid asymmetry. *J Lipid Res* **44**, 233-242, (2003).

99 Nakase, I. *et al.* Efficient intracellular delivery of nucleic acid pharmaceuticals using cell-penetrating peptides. *Acc Chem Res* **45**, 1132-1139 (2011).

100 Hirsch-Lerner, D. *et al.* Effect of "helper lipid" on lipoplex electrostatics. *Biochim Biophys Acta* **1714**, 71-84, (2005).

101 Lee, L. K., Williams, C. L., Devore, D. & Roth, C. M. Poly(propylacrylic acid) enhances cationic lipid-mediated delivery of antisense oligonucleotides. *Biomacromolecules* **7**, 1502-1508, (2006).

102 Gooding, M., Browne, L. P., Quinteiro, F. M. & Selwood, D. L. siRNA delivery: from lipids to cell-penetrating peptides and their mimics. *Chem Biol Drug Des* **80**, 787-809, (2012).

103 Gao, X., Kim, K. S. & Liu, D. Nonviral gene delivery: what we know and what is next. *AAPS J* **9**, E92-104, (2007).

104 Subbarao, N. K., Parente, R. A., Szoka, F. C., Jr., Nadasdi, L. & Pongracz, K. pH-dependent bilayer destabilization by an amphipathic peptide. *Biochemistry* **26**, 2964-2972, (1987).

105 Wadia, J. S., Stan, R. V. & Dowdy, S. F. Transducible TAT-HA fusogenic peptide enhances escape of TAT-fusion proteins after lipid raft macropinocytosis. *Nat Med* **10**, 310-315, (2004).

106 Stayton, P. S. *et al.* Molecular engineering of proteins and polymers for targeting and intracellular delivery of therapeutics. *J Control Release* **65**, 203-220, (2000).

107 Maeda, T., Kawasaki, K. & Ohnishi, S. Interaction of influenza virus hemagglutinin with target membrane lipids is a key step in virus-induced hemolysis and fusion at pH 5.2. *Proc Natl Acad Sci U S A* **78**, 4133-4137, (1981).

108 Bullough, P. A., Hughson, F. M., Skehel, J. J. & Wiley, D. C. Structure of influenza haemagglutinin at the pH of membrane fusion. *Nature* **371**, 37-43, (1994).

109 Kaplan, I. M., Wadia, J. S. & Dowdy, S. F. Cationic TAT peptide transduction domain enters cells by macropinocytosis. *J Control Release* **102**, 247-253, (2005).

110 Plank, C., Oberhauser, B., Mechtler, K., Koch, C. & Wagner, E. The influence of endosome-disruptive peptides on gene transfer using synthetic virus-like gene transfer systems. *J Biol Chem* **269**, 12918-12924, (1994).

111 Esbjorner, E. K., Oglecka, K., Lincoln, P., Graslund, A. & Norden, B. Membrane binding of pH-sensitive influenza fusion peptides. positioning, configuration, and induced leakage in a lipid vesicle model. *Biochemistry* **46**, 13490-13504, (2007).

112 Midoux, P., Kichler, A., Boutin, V., Maurizot, J. C. & Monsigny, M. Membrane permeabilization and efficient gene transfer by a peptide containing several histidines. *Bioconjug Chem* **9**, 260-267, (1998).

113 Pichon, C., Goncalves, C. & Midoux, P. Histidine-rich peptides and polymers for nucleic acids delivery. *Adv Drug Deliv Rev* **53**, 75-94, (2001).

114 Midoux, P. *et al.* Specific gene transfer mediated by lactosylated poly-L-lysine into hepatoma cells. *Nucleic Acids Res* **21**, 871-878, (1993).

115 Pichon, C. *et al.* Cytosolic and nuclear delivery of oligonucleotides mediated by an amphiphilic anionic peptide. *Antisense Nucleic Acid Drug Dev* **7**, 335-343, (1997).

116 Klink, D. T., Chao, S., Glick, M. C. & Scanlin, T. F. Nuclear translocation of lactosylated poly-L-lysine/cDNA complex in cystic fibrosis airway epithelial cells. *Mol Ther* **3**, 831-841, (2001).

117 Rittner, K. *et al.* New basic membrane-destabilizing peptides for plasmid-based gene delivery in vitro and in vivo. *Mol Ther* **5**, 104-114, (2002).

118 Numata, K. & Kaplan, D. L. Silk-Based Gene Carriers with Cell Membrane Destabilizing Peptides. *Biomacromolecules* **11**, 3189-3195, (2010).

119 Simeoni, F., Morris, M. C., Heitz, F. & Divita, G. Insight into the mechanism of the peptide-based gene delivery system MPG: implications for delivery of siRNA into mammalian cells. *Nucleic Acids Res* **31**, 2717-2724, (2003).

120 Morris, M. C., Chaloin, L., Mery, J., Heitz, F. & Divita, G. A novel potent strategy for gene delivery using a single peptide vector as a carrier. *Nucleic Acids Res* **27**, 3510-3517, (1999).

121 Kwon, E. J., Bergen, J. M. & Pun, S. H. Application of an HIV gp41-derived peptide for enhanced intracellular trafficking of synthetic gene and siRNA delivery vehicles. *Bioconjug Chem* **19**, 920-927, (2008).

122 Lundberg, P., El-Andaloussi, S., Sutlu, T., Johansson, H. & Langel, U. Delivery of short interfering RNA using endosomolytic cell-penetrating peptides. *FASEB J* **21**, 2664-2671, (2007).

123 El-Andaloussi, S., Johansson, H. J., Lundberg, P. & Langel, U. Induction of splice correction by cell-penetrating peptide nucleic acids. *J Gene Med* **8**, 1262-1273, (2006).

124 Wyman, T. B. *et al.* Design, synthesis, and characterization of a cationic peptide that binds to nucleic acids and permeabilizes bilayers. *Biochemistry* **36**, 3008-3017, (1997).

125 Lee, H., Jeong, J. H. & Park, T. G. A new gene delivery formulation of polyethylenimine/DNA complexes coated with PEG conjugated fusogenic peptide. *J Control Release* **76**, 183-192, (2001).

126 Han, J., Lim, M. & Yeom, Y. I. Receptor-mediated gene transfer to cells of hepatic origin by galactosylated albumin-polylysine complexes. *Biol Pharm Bull* **22**, 836-840, (1999).

127 Min, S. H. *et al.* A composite gene delivery system consisting of polyethylenimine and an amphipathic peptide KALA. *J Gene Med* **8**, 1425-1434, (2006).

128 Parente, R. A., Nir, S. & Szoka, F. C., Jr. Mechanism of leakage of phospholipid vesicle contents induced by the peptide GALA. *Biochemistry* **29**, 8720-8728, (1990).

129 Li, W., Nicol, F. & Szoka, F. C., Jr. GALA: a designed synthetic pH-responsive amphipathic peptide with applications in drug and gene delivery. *Adv Drug Deliv Rev* **56**, 967-985, (2004).

130 Kichler, A., Leborgne, C., Marz, J., Danos, O. & Bechinger, B. Histidine-rich amphipathic peptide antibiotics promote efficient delivery of DNA into mammalian cells. *Proc Natl Acad Sci U S A* **100**, 1564-1568, (2003).

131 Lam, J. K., Liang, W. & Chan, H. K. Pulmonary delivery of therapeutic siRNA. *Adv Drug Deliv Rev* **64**, 1-15, (2012).

132 Bechinger, B. Towards membrane protein design: pH-sensitive topology of histidine-containing polypeptides. *J Mol Biol* **263**, 768-775, (1996).

133 Vogt, T. C. & Bechinger, B. The interactions of histidine-containing amphipathic helical peptide antibiotics with lipid bilayers. The effects of charges and pH. *J Biol Chem* **274**, 29115-29121, (1999).

134 Kichler, A., Mason, A. J. & Bechinger, B. Cationic amphipathic histidine-rich peptides for gene delivery. *Biochim Biophys Acta* **1758**, 301-307, (2006).

135 Andaloussi, S. E. *et al.* Design of a peptide-based vector, PepFect6, for efficient delivery of siRNA in cell culture and systemically in vivo. *Nucleic Acids Res* **39**, 3972-3987, (2011).

136 Cheng, J. *et al.* Structure-function correlation of chloroquine and analogues as transgene expression enhancers in nonviral gene delivery. *J Med Chem* **49**, 6522-6531, (2006).

137 Pooga, M. *et al.* Cell penetrating PNA constructs regulate galanin receptor levels and modify pain transmission in vivo. *Nat Biotechnol* **16**, 857-861, (1998).

138 Varkouhi, A. K., Scholte, M., Storm, G. & Haisma, H. J. Endosomal escape pathways for delivery of biologicals. *J Control Release* **151**, 220-228, (2011).

139 Brooks, H., Lebleu, B. & Vives, E. Tat peptide-mediated cellular delivery: back to basics. *Adv Drug Deliv Rev* **57**, 559-577, (2005).

140 Brogden, K. A. Antimicrobial peptides: pore formers or metabolic inhibitors in bacteria? *Nat Rev Microbiol* **3**, 238-250, (2005).

141 Raagel, H., Saalik, P. & Pooga, M. Peptide-mediated protein delivery-which pathways are penetrable? *Biochim Biophys Acta* **1798**, 2240-2248, (2010).

142 Sato, H. & Feix, J. B. Peptide-membrane interactions and mechanisms of membrane destruction by amphipathic alpha-helical antimicrobial peptides. *Biochim Biophys Acta* **1758**, 1245-1256, (2006).

143 Zhang, X. *et al.* Dual functions of the human antimicrobial peptide LL-37-target membrane perturbation and host cell cargo delivery. *Biochim Biophys Acta* **1798**, 2201-2208, (2010).

144 Sandgren, S. *et al.* The human antimicrobial peptide LL-37 transfers extracellular DNA plasmid to the nuclear compartment of mammalian cells via lipid rafts and proteoglycan-dependent endocytosis. *J Biol Chem* **279**, 17951-17956, (2004).

145 Legendre, J. Y. *et al.* Dioleoylmelittin as a novel serum-insensitive reagent for efficient transfection of mammalian cells. *Bioconjug Chem* **8**, 57-63, (1997).

146 Andreu, D. *et al.* Shortened cecropin A-melittin hybrids. Significant size reduction retains potent antibiotic activity. *FEBS Lett* **296**, 190-194, (1992).

147 Boman, H. G., Wade, D., Boman, I. A., Wahlin, B. & Merrifield, R. B. Antibacterial and antimalarial properties of peptides that are cecropin-melittin hybrids. *FEBS Lett* **259**, 103-106, (1989).

148 Tossi, A., Sandri, L. & Giangaspero, A. Amphipathic, alpha-helical antimicrobial peptides. *Biopolymers* **55**, 4-30, (2000).

149 Oren, Z., Lerman, J. C., Gudmundsson, G. H., Agerberth, B. & Shai, Y. Structure and organization of the human antimicrobial peptide LL-37 in phospholipid membranes: relevance to the molecular basis for its non-cell-selective activity. *Biochem J* **341 (Pt 3)**, 501-513, (1999).

150 Gudmundsson, G. H. *et al.* The human gene FALL39 and processing of the cathelin precursor to the antibacterial peptide LL-37 in granulocytes. *Eur J Biochem* **238**, 325-332, (1996).

151 Larrick, J. W. *et al.* Human CAP18: a novel antimicrobial lipopolysaccharide-binding protein. *Infect Immun* **63**, 1291-1297, (1995).

152 Sorensen, O., Cowland, J. B., Askaa, J. & Borregaard, N. An ELISA for hCAP-18, the cathelicidin present in human neutrophils and plasma. *J Immunol Methods* **206**, 53-59, (1997).

153 Turner, J., Cho, Y., Dinh, N. N., Waring, A. J. & Lehrer, R. I. Activities of LL-37, a cathelin-associated antimicrobial peptide of human neutrophils. *Antimicrob Agents Chemother* **42**, 2206-2214, (1998).

154 Sood, R. & Kinnunen, P. K. Cholesterol, lanosterol, and ergosterol attenuate the membrane association of LL-37(W27F) and temporin L. *Biochim Biophys Acta* **1778**, 1460-1466, (2008).

155 Henzler Wildman, K. A., Lee, D. K. & Ramamoorthy, A. Mechanism of lipid bilayer disruption by the human antimicrobial peptide, LL-37. *Biochemistry* **42**, 6545-6558, (2003).

156 Altenbach, C. & Hubbell, W. L. The aggregation state of spin-labeled melittin in solution and bound to phospholipid membranes: evidence that membrane-bound melittin is monomeric. *Proteins* **3**, 230-242, (1988).

157 Bechinger, B. Structure and functions of channel-forming peptides: magainins, cecropins, melittin and alamethicin. *J Membr Biol* **156**, 197-211, (1997).

158 Bechinger, B. The structure, dynamics and orientation of antimicrobial peptides in membranes by multidimensional solid-state NMR spectroscopy. *Biochim Biophys Acta* **1462**, 157-183, (1999).

159 Altenbach, C., Froncisz, W., Hyde, J. S. & Hubbell, W. L. Conformation of spin-labeled melittin at membrane surfaces investigated by pulse saturation recovery and continuous wave power saturation electron paramagnetic resonance. *Biophys J* **56**, 1183-1191, (1989).

160 Legendre, J. Y. & Szoka, F. C., Jr. Cyclic amphipathic peptide-DNA complexes mediate high-efficiency transfection of adherent mammalian cells. *Proc Natl Acad Sci U S A* **90**, 893-897, (1993).

161 Rozema, D. B., Ekena, K., Lewis, D. L., Loomis, A. G. & Wolff, J. A. Endosomolysis by masking of a membrane-active agent (EMMA) for cytoplasmic release of macromolecules. *Bioconjug Chem* **14**, 51-57, (2003).

162 Meyer, M., Philipp, A., Oskuee, R., Schmidt, C. & Wagner, E. Breathing life into polycations: functionalization with pH-responsive endosomolytic peptides and polyethylene glycol enables siRNA delivery. *J Am Chem Soc* **130**, 3272-3273, (2008).

163 Boeckle, S., Fahrmeir, J., Roedl, W., Ogris, M. & Wagner, E. Melittin analogs with high lytic activity at endosomal pH enhance transfection with purified targeted PEI polyplexes. *J Control Release* **112**, 240-248, (2006).

164 Tan, Y. X. *et al.* Truncated peptides from melittin and its analog with high lytic activity at endosomal pH enhance branched polyethylenimine-mediated gene transfection. *J Gene Med* **14**, 241-250, (2012).

165 Wade, D. *et al.* Antibacterial peptides designed as analogs or hybrids of cecropins and melittin. *Int J Pept Protein Res* **40**, 429-436, (1992).

166 Piers, K. L., Brown, M. H. & Hancock, R. E. Improvement of outer membrane-permeabilizing and lipopolysaccharide-binding activities of an antimicrobial cationic peptide by C-terminal modification. *Antimicrob Agents Chemother* **38**, 2311-2316, (1994).

167 Gazit, E., Boman, A., Boman, H. G. & Shai, Y. Interaction of the mammalian antibacterial peptide cecropin P1 with phospholipid vesicles. *Biochemistry* **34**, 11479-11488, (1995).

168 Shai, Y. Mode of action of membrane active antimicrobial peptides. *Biopolymers* **66**, 236-248, (2002).

169 Steiner, H., Andreu, D. & Merrifield, R. B. Binding and action of cecropin and cecropin analogues: antibacterial peptides from insects. *Biochim Biophys Acta* **939**, 260-266, (1988).

170 Juvvadi, P., Vunnam, S., Merrifield, E. L., Boman, H. G. & Merrifield, R. B. Hydrophobic effects on antibacterial and channel-forming properties of cecropin A-melittin hybrids. *J Pept Sci* **2**, 223-232, (1996).

171 Christensen, B., Fink, J., Merrifield, R. B. & Mauzerall, D. Channel-forming properties of cecropins and related model compounds incorporated into planar lipid membranes. *Proc Natl Acad Sci U S A* **85**, 5072-5076, (1988).

172 Huang, H. W. Action of antimicrobial peptides: two-state model. *Biochemistry* **39**, 8347-8352, (2000).

173 Zasloff, M. Antimicrobial peptides of multicellular organisms. *Nature* **415**, 389-395, (2002).

174 Brasseur, R. & Divita, G. Happy birthday cell penetrating peptides: already 20 years. *Biochim Biophys Acta* **1798**, 2177-2181,(2012).

175 Bechara, C. & Sagan, S. Cell-penetrating peptides: 20 years later, where do we stand? *FEBS Lett* **587**, 1693-1702, (2013).

176 Milletti, F. Cell-penetrating peptides: classes, origin, and current landscape. *Drug Discov Today* **17**, 850-860, (2012).

177 Milletti, F. Cell-penetrating peptides: classes, origin, and current landscape. *Drug Discov Today* **17**, 850-860, (2012).

178 Cardarelli, F., Serresi, M., Bizzarri, R., Giacca, M. & Beltram, F. In vivo study of HIV-1 Tat arginine-rich motif unveils its transport properties. *Mol Ther* **15**, 1313-1322, (2007).

179 Cardarelli, F., Serresi, M., Bizzarri, R. & Beltram, F. Tuning the transport properties of HIV-1 Tat arginine-rich motif in living cells. *Traffic* **9**, 528-539, (2008).

180 Cardarelli, F., Serresi, M., Albanese, A., Bizzarri, R. & Beltram, F. Quantitative analysis of Tat peptide binding to import carriers reveals unconventional nuclear transport properties. *J Biol Chem* **286**, 12292-12299, (2011).

181 Frankel, A. D. & Pabo, C. O. Cellular uptake of the tat protein from human immunodeficiency virus. *Cell* **55**, 1189-1193, (1988).

182 Vives, E., Brodin, P. & Lebleu, B. A truncated HIV-1 Tat protein basic domain rapidly translocates through the plasma membrane and accumulates in the cell nucleus. *J Biol Chem* **272**, 16010-16017, (1997).

183 Rothbard, J. B. *et al.* Arginine-rich molecular transporters for drug delivery: role of backbone spacing in cellular uptake. *J Med Chem* **45**, 3612-3618, (2002).

184 Richard, J. P. *et al.* Cell-penetrating peptides. A reevaluation of the mechanism of cellular uptake. *J Biol Chem* **278**, 585-590, (2003).

185 Nakase, I. *et al.* Cellular uptake of arginine-rich peptides: roles for macropinocytosis and actin rearrangement. *Mol Ther* **10**, 1011-1022, (2004).

186 Richard, J. P. *et al.* Cellular uptake of unconjugated TAT peptide involves clathrin-dependent endocytosis and heparan sulfate receptors. *J Biol Chem* **280**, 15300-15306, (2005).

187 Ferrari, A. *et al.* Caveolae-mediated internalization of extracellular HIV-1 tat fusion proteins visualized in real time. *Mol Ther* **8**, 284-294, (2003).

188 Lundin, P. *et al.* Distinct uptake routes of cell-penetrating peptide conjugates. *Bioconjug Chem* **19**, 2535-2542, (2008).

189 Kilic, G., Doctor, R. B. & Fitz, J. G. Insulin stimulates membrane conductance in a liver cell line: evidence for insertion of ion channels through a phosphoinositide 3-kinase-dependent mechanism. *J Biol Chem* **276**, 26762-26768, (2001).

190 Neuhaus, E. M. & Soldati, T. A myosin I is involved in membrane recycling from early endosomes. *J Cell Biol* **150**, 1013-1026, (2000).

191 Ruan, G., Agrawal, A., Marcus, A. I. & Nie, S. Imaging and tracking of tat peptide-conjugated quantum dots in living cells: new insights into nanoparticle uptake, intracellular transport, and vesicle shedding. *J Am Chem Soc* **129**, 14759-14766, (2007).

192 Vandenbroucke, R. E., De Smedt, S. C., Demeester, J. & Sanders, N. N. Cellular entry pathway and gene transfer capacity of TAT-modified lipoplexes. *Biochim Biophys Acta* **1768**, 571-579, (2007).

193 Rinne, J. *et al.* Internalization of novel non-viral vector TAT-streptavidin into human cells. *BMC Biotechnol* **7**, 1, (2007).

194 El-Sayed, A., Futaki, S. & Harashima, H. Delivery of macromolecules using arginine-rich cell-penetrating peptides: ways to overcome endosomal entrapment. *AAPS J* **11**, 13-22, (2009).

195 Pistolesi, S., Pogni, R. & Feix, J. B. Membrane insertion and bilayer perturbation by antimicrobial peptide CM15. *Biophys J* **93**, 1651-1660, (2007).

196 Respondek, M., Madl, T., Gobl, C., Golser, R. & Zangger, K. Mapping the orientation of helices in micelle-bound peptides by paramagnetic relaxation waves. *J Am Chem Soc* **129**, 5228-5234, (2007).

197 Piantavigna, S. *et al.* A mechanistic investigation of cell-penetrating Tat peptides with supported lipid membranes. *Biochim Biophys Acta* **1808**, 1811-1817, (2011).

198 Rusnati, M. *et al.* The basic domain in HIV-1 Tat protein as a target for polysulfonated heparin-mimicking extracellular Tat antagonists. *J Biol Chem* **273**, 16027-16037, (1998).

199 Sugita, T. *et al.* Comparative study on transduction and toxicity of protein transduction domains. *Br J Pharmacol* **153**, 1143-1152, (2008).

200 Duchardt, F., Fotin-Mleczek, M., Schwarz, H., Fischer, R. & Brock, R. A comprehensive model for the cellular uptake of cationic cell-penetrating peptides. *Traffic* **8**, 848-866, (2007).

201 Jones, R. A. *et al.* Poly(2-alkylacrylic acid) polymers deliver molecules to the cytosol by pH-sensitive disruption of endosomal vesicles. *Biochem J* **372**, 65-75, (2003).

202 Wallach, D. F. & Steck, T. L. Fluorescence Techniques in Microdetermination of Metals in Biological Materials. Ii. An Improved Method for Direct Complexometric Titration of Calcium in Small Serum Samples. *Anal Biochem* **6**, 176-180, (1963).

203 Chen, Y. & Simon, S. M. In situ biochemical demonstration that P-glycoprotein is a drug efflux pump with broad specificity. *J Cell Biol* **148**, 863-870, (2000).

204 Ellerbroek, S. M. *et al.* SGEF, a RhoG guanine nucleotide exchange factor that stimulates macropinocytosis. *Mol Biol Cell* **15**, 3309-3319, (2004).

205 Armstrong, J. K., Wenby, R. B., Meiselman, H. J. & Fisher, T. C. The hydrodynamic radii of macromolecules and their effect on red blood cell aggregation. *Biophys J* **87**, 4259-4270, (2004).

206 Paine, P. L., Moore, L. C. & Horowitz, S. B. Nuclear envelope permeability. *Nature* **254**, 109-114, (1975).

207 Meier, O. *et al.* Adenovirus triggers macropinocytosis and endosomal leakage together with its clathrin-mediated uptake. *J Cell Biol* **158**, 1119-1131, (2002).

208 Matsuo, H. *et al.* Role of LBPA and Alix in multivesicular liposome formation and endosome organization. *Science* **303**, 531-534, (2004).

209 Henderson, E., Haydon, P. G. & Sakaguchi, D. S. Actin filament dynamics in living glial cells imaged by atomic force microscopy. *Science* **257**, 1944-1946, (1992).

210 Luo, D. & Saltzman, W. M. Synthetic DNA delivery systems. *Nat Biotechnol* **18**, 33-37, (2000).

211 Kay, M. A., Glorioso, J. C. & Naldini, L. Viral vectors for gene therapy: the art of turning infectious agents into vehicles of therapeutics. *Nat Med* **7**, 33-40, (2001).

212 Warnock, J. N., Daigre, C. & Al-Rubeai, M. Introduction to viral vectors. *Methods Mol Biol* **737**, 1-25, (2011).

213 Thomas, C. E., Ehrhardt, A. & Kay, M. A. Progress and problems with the use of viral vectors for gene therapy. *Nat Rev Genet* **4**, 346-358, (2003).

214 Viola, J. R., El-Andaloussi, S., Oprea, II & Smith, C. I. Non-viral nanovectors for gene delivery: factors that govern successful therapeutics. *Expert Opin Drug Deliv* **7**, 721-735, (2010).

215 Jo, J. & Tabata, Y. Non-viral gene transfection technologies for genetic engineering of stem cells. *Eur J Pharm Biopharm* **68**, 90-104, (2008).

216 Li, S. & Huang, L. Nonviral gene therapy: promises and challenges. *Gene Ther* **7**, 31-34, (2000).

217 Pack, D. W., Hoffman, A. S., Pun, S. & Stayton, P. S. Design and development of polymers for gene delivery. *Nat Rev Drug Discov* **4**, 581-593, (2005).

218 Petros, R. A. & DeSimone, J. M. Strategies in the design of nanoparticles for therapeutic applications. *Nat Rev Drug Discov* **9**, 615-627, (2010).

219 Bolhassani, A. Potential efficacy of cell-penetrating peptides for nucleic acid and drug delivery in cancer. *Biochim Biophys Acta* **1816**, 232-246, (2011).

220 Glover, D. J., Lipps, H. J. & Jans, D. A. Towards safe, non-viral therapeutic gene expression in humans. *Nat Rev Genet* **6**, 299-310, (2005).

221 Lehto, T. *et al.* A peptide-based vector for efficient gene transfer in vitro and in vivo. *Mol Ther* **19**, 1457-1467, (2011).

222 Ignatovich, I. A. *et al.* Complexes of plasmid DNA with basic domain 47-57 of the HIV-1 Tat protein are transferred to mammalian cells by endocytosis-mediated pathways. *J Biol Chem* **278**, 42625-42636, (2003).

223 Liu, Z., Li, M., Cui, D. & Fei, J. Macro-branched cell-penetrating peptide design for gene delivery. *J Control Release* **102**, 699-710, (2005).

224 Lo, S. L. & Wang, S. An endosomolytic Tat peptide produced by incorporation of histidine and cysteine residues as a nonviral vector for DNA transfection. *Biomaterials* **29**, 2408-2414, (2008).

225 Liu, B. R., Lin, M. D., Chiang, H. J. & Lee, H. J. Arginine-rich cell-penetrating peptides deliver gene into living human cells. *Gene* **505**, 37-45, (2012).

226 Yamano, S. *et al.* Modified Tat peptide with cationic lipids enhances gene transfection efficiency via temperature-dependent and caveolae-mediated endocytosis. *J Control Release* **152**, 278-285, (2011).

227 Yi, W. J. *et al.* Enhanced nuclear import and transfection efficiency of TAT peptide-based gene delivery systems modified by additional nuclear localization signals. *Bioconjug Chem* **23**, 125-134, (2012).

228 Hoyer, J. & Neundorf, I. Peptide vectors for the nonviral delivery of nucleic acids. *Acc Chem Res* **45**, 1048-1056, (2012).

229 Said Hassane, F., Saleh, A. F., Abes, R., Gait, M. J. & Lebleu, B. Cell penetrating peptides: overview and applications to the delivery of oligonucleotides. *Cell Mol Life Sci* **67**, 715-726, (2010).

230 Salomone, F. *et al.* A novel chimeric cell-penetrating peptide with membrane-disruptive properties for efficient endosomal escape. *J Control Release* **163**, 293-303, (2012).

231 Meade, B. R. & Dowdy, S. F. Enhancing the cellular uptake of siRNA duplexes following noncovalent packaging with protein transduction domain peptides. *Adv Drug Deliv Rev* **60**, 530-536, (2008).

232 Deshayes, S., Morris, M., Heitz, F. & Divita, G. Delivery of proteins and nucleic acids using a non-covalent peptide-based strategy. *Adv Drug Deliv Rev* **60**, 537-547, (2008).

233 Wender, P. A. *et al.* The design, synthesis, and evaluation of molecules that enable or enhance cellular uptake: peptoid molecular transporters. *Proc Natl Acad Sci U S A* **97**, 13003-13008, (2000).

234 Erazo-Oliveiras, A., Muthukrishnan, N., Baker, R., Wang, T. & Pellois, J. Improving the endosomal escape of cell-penetrating peptides and their cargos: strategies and challenges. *Pharmaceuticals* **5**, 1177-1209, (2012).

235 Mae, M. *et al.* A stearylated CPP for delivery of splice correcting oligonucleotides using a non-covalent co-incubation strategy. *J Control Release* **134**, 221-227, (2009).

236 Gooding, M., Browne, L. P., Quinteiro, F. M. & Selwood, D. L. siRNA delivery: from lipids to cell-penetrating peptides and their mimics. *Chem Biol Drug Des* **80**, 787-809, (2012).

237 Cardarelli, F., Pozzi, D., Bifone, A., Marchini, C. & Caracciolo, G. Cholesterol-dependent macropinocytosis and endosomal escape control the transfection efficiency of lipoplexes in CHO living cells. *Mol Pharm* **9**, 334-340, (2012).

238 Pozzi, D. *et al.* Transfection efficiency boost of cholesterol-containing lipoplexes. *Biochim Biophys Acta* **1818**, 2335-2343, (2012).

239 Coonrod, A., Li, F. Q. & Horwitz, M. On the mechanism of DNA transfection: efficient gene transfer without viruses. *Gene Ther* **4**, 1313-1321, (1997).

240 James, M. B. & Giorgio, T. D. Nuclear-associated plasmid, but not cell-associated plasmid, is correlated with transgene expression in cultured mammalian cells. *Mol Ther* **1**, 339-346, (2000).

241 Tseng, W. C., Haselton, F. R. & Giorgio, T. D. Transfection by cationic liposomes using simultaneous single cell measurements of plasmid delivery and transgene expression. *J Biol Chem* **272**, 25641-25647, (1997).

242 Ludtke, J. J., Sebestyen, M. G. & Wolff, J. A. The effect of cell division on the cellular dynamics of microinjected DNA and dextran. *Mol Ther* **5**, 579-588, (2002).

243 Dean, D. A., Byrd, J. N., Jr. & Dean, B. S. Nuclear targeting of plasmid DNA in human corneal cells. *Curr Eye Res* **19**, 66-75, (1999).

244 Escriou, V., Ciolina, C., Helbling-Leclerc, A., Wils, P. & Scherman, D. Cationic lipid-mediated gene transfer: analysis of cellular uptake and nuclear import of plasmid DNA. *Cell Biol Toxicol* **14**, 95-104, (1998).

245 Lechardeur, D. *et al.* Metabolic instability of plasmid DNA in the cytosol: a potential barrier to gene transfer. *Gene Ther* **6**, 482-497, (1999).

246 Zelphati, O., Liang, X., Hobart, P. & Felgner, P. L. Gene chemistry: functionally and conformationally intact fluorescent plasmid DNA. *Hum Gene Ther* **10**, 15-24, (1999).

247 Pollard, H. *et al.* Ca2+-sensitive cytosolic nucleases prevent efficient delivery to the nucleus of injected plasmids. *J Gene Med* **3**, 153-164, (2001).

248 Banks, G. A., Roselli, R. J., Chen, R. & Giorgio, T. D. A model for the analysis of nonviral gene therapy. *Gene Ther* **10**, 1766-1775, (2003).

249 Salomone, F., Cardarelli, F., Signore, G., Boccardi, C. & Beltram, F. In Vitro Efficient Transfection by CM18-Tat11 Hybrid Peptide: A New Tool for Gene-Delivery Applications. *PLoS One* **8**, e70108, (2013).

250 Bechinger, B. & Lohner, K. Detergent-like actions of linear amphipathic cationic antimicrobial peptides. *Biochim Biophys Acta* **1758**, 1529-1539, (2006).

251 Schlamadinger, D. E., Wang, Y., McCammon, J. A. & Kim, J. E. Spectroscopic and computational study of melittin, cecropin A, and the hybrid peptide CM15. *J Phys Chem B* **116**, 10600-10608, (2012).

252 Alfieri, K. N., Vienneau, A. R. & Londergan, C. H. Using infrared spectroscopy of cyanylated cysteine to map the membrane binding structure and orientation of the hybrid antimicrobial peptide CM15. *Biochemistry* **50**, 11097-11108, (2011).

253 Zangger, K. *et al.* Positioning of micelle-bound peptides by paramagnetic relaxation enhancements. *J Phys Chem B* **113**, 4400-4406, (2009).

254 McMahon, H. A., Alfieri, K. N., Clark, K. A. & Londergan, C. H. Cyanylated Cysteine: A Covalently Attached Vibrational Probe of Protein-Lipid Contacts. *J Phys Chem Lett* **1**, 850-855, (2010).

255 Parasassi, T., De Stasio, G., Ravagnan, G., Rusch, R. M. & Gratton, E. Quantitation of lipid phases in phospholipid vesicles by the generalized polarization of Laurdan fluorescence. *Biophys J* **60**, 179-189, (1991).

256 Huang, H. *et al.* Use of dansyl-cholestanol as a probe of cholesterol behavior in membranes of living cells. *J Lipid Res* **51**, 1157-1172, (2010).

257 Hohsaka, T. *et al.* Position-specific incorporation of dansylated non-natural amino acids into streptavidin by using a four-base codon. *FEBS Lett* **560**, 173-177, (2004).

258 Signore, G. *et al.* Imaging the static dielectric constant in vitro and in living cells by a bioconjugable GFP chromophore analog. *Chem Commun (Camb)* **49**, 1723-1725, (2013).

259 Signore, G., Nifosi, R., Albertazzi, L. & Bizzarri, R. A novel coumarin fluorescent sensor to probe polarity around biomolecules. *J Biomed Nanotechnol* **5**, 722-729, (2009).

260 Signore, G., Nifosi, R., Albertazzi, L., Storti, B. & Bizzarri, R. Polarity-sensitive coumarins tailored to live cell imaging. *J Am Chem Soc* **132**, 1276-1288, (2010).

261 Haidekker, M. A. *et al.* Phospholipid-bound molecular rotors: synthesis and characterization. *Bioorg Med Chem* **10**, 3627-3636, (2002).

262 Stockl, M. T. & Herrmann, A. Detection of lipid domains in model and cell membranes by fluorescence lifetime imaging microscopy. *Biochim Biophys Acta* **1798**, 1444-1456, (2010).

263 Demchenko, A. P. The concept of lambda-ratiometry in fluorescence sensing and imaging. *J Fluoresc* **20**, 1099-1128, (2010).

264 Gaus, K., Zech, T. & Harder, T. Visualizing membrane microdomains by Laurdan 2-photon microscopy. *Mol Membr Biol* **23**, 41-48, (2006).

265 Glaser, R. *Biophysics*. (2000).

266 Milani, A., Benedusi, M., Aquila, M. & Rispoli, G. Pore forming properties of cecropin-melittin hybrid peptide in a natural membrane. *Molecules* **14**, 5179-5188, (2009).

267 Vedovato, N. & Rispoli, G. A novel technique to study pore-forming peptides in a natural membrane. *Eur Biophys J* **36**, 771-778, (2007).

268 Rispoli, G., Sather, W. A. & Detwiler, P. B. Visual transduction in dialysed detached rod outer segments from lizard retina. *J Physiol* **465**, 513-537, (1993).

269 Madan, V. *et al.* Plasma membrane-porating domain in poliovirus 2B protein. A short peptide mimics viroporin activity. *J Mol Biol* **374**, 951-964, (2007).

270 Dominska, M. & Dykxhoorn, D. M. Breaking down the barriers: siRNA delivery and endosome escape. *J Cell Sci* **123**, 1183-1189, (2010).

271 Neumann, E. & Rosenheck, K. Permeability changes induced by electric impulses in vesicular membranes. *J Membr Biol* **10**, 279-290, (1972).

272 Teissie, J., Eynard, N., Gabriel, B. & Rols, M. P. Electropermeabilization of cell membranes. *Adv Drug Deliv Rev* **35**, 3-19, (1999).

273 Escoffre, J. M., Teissie, J. & Rols, M. P. Gene transfer: how can the biological barriers be overcome? *J Membr Biol* **236**, 61-74, (2010).

274 Golzio, M., Teissie, J. & Rols, M. P. Direct visualization at the single-cell level of electrically mediated gene delivery. *Proc Natl Acad Sci U S A* **99**, 1292-1297, (2002).

275 Paganin-Gioanni, A. *et al.* Direct visualization at the single-cell level of siRNA electrotransfer into cancer cells. *Proc Natl Acad Sci U S A* **108**, 10443-10447, (2011).

276 Satkauskas, S. *et al.* Mechanisms of in vivo DNA electrotransfer: respective contributions of cell electropermeabilization and DNA electrophoresis. *Mol Ther* **5**, 133-140, (2002).

277 Gehl, J. & Mir, L. M. Determination of optimal parameters for in vivo gene transfer by electroporation, using a rapid in vivo test for cell permeabilization. *Biochem Biophys Res Commun* **261**, 377-380, (1999).

278 Breton, M. & Mir, L. M. Microsecond and nanosecond electric pulses in cancer treatments. *Bioelectromagnetics,* doi:10.1002/bem.20692, (2011).

279 Sundararajan, R. Nanosecond electroporation: another look. *Mol Biotechnol* **41**, 69-82, (2009).

280 Vernier, P. T., Li, A., Marcu, L., Craft, C. M. & Gundersen, M. A. Ultrashort pulsed electric fields induce membrane phospholipids translocation and caspase activation: Differential sensitivities of Jurkat T lymphoblasts and rat glioma C6 cells. *IEEE Transactions on Dielectrics and Electrical Insulation* **10**, 795-809, (2003).

281 Schoenbach, K. H., Beebe, S. J. & Buescher, E. S. Intracellular effect of ultrashort electrical pulses. *Bioelectromagnetics* **22**, 440-448, (2001).

282 Vernier, P. T., Sun, Y. & Gundersen, M. A. Nanoelectropulse-driven membrane perturbation and small molecule permeabilization. *BMC Cell Biol* **7**, 37, (2006).

283 Ibey, B. L., Xiao, S., Schoenbach, K. H., Murphy, M. R. & Pakhomov, A. G. Plasma membrane permeabilization by 60- and 600-ns electric pulses is determined by the absorbed dose. *Bioelectromagnetics* **30**, 92-99, (2009).

284 Pakhomov, A. G. *et al.* Long-lasting plasma membrane permeabilization in mammalian cells by nanosecond pulsed electric field (nsPEF). *Bioelectromagnetics* **28**, 655-663, (2007).

285 Vernier, P. T. *et al.* Calcium bursts induced by nanosecond electric pulses. *Biochem Biophys Res Commun* **310**, 286-295, (2003).

286 Napotnik, T. B. *et al.* Electropermeabilization of endocytotic vesicles in B16 F1 mouse melanoma cells. *Med Biol Eng Comput* **48**, 407-413, (2010).

287 Pakhomov, A. G. *et al.* Lipid nanopores can form a stable, ion channel-like conduction pathway in cell membrane. *Biochem Biophys Res Commun* **385**, 181-186, (2009).

288 Chen, N. *et al.* Leukemic cell intracellular responses to nanosecond electric fields. *Biochem Biophys Res Commun* **317**, 421-427, (2004).

289 Breton, M., Delemotte, L., Silve, A., Mir, L. M. & Tarek, M. Transport of siRNA through lipid membranes driven by nanosecond electric pulses: an experimental and computational study. *J Am Chem Soc* **134**, 13938-13941, (2012).

290 Angelova, I. A. & Dimitrov, S. D. Liposome electroformation. *Faraday Discussions of the Chemical Society* **1986**, 303-311, (1986).

291 Bhargava, K. & Feix, J. B. Membrane binding, structure, and localization of cecropin-mellitin hybrid peptides: a site-directed spin-labeling study. *Biophys J* **86**, 329-336, (2004).

292 Delemotte, L., Dehez, F., Treptow, W. & Tarek, M. Modeling membranes under a transmembrane potential. *J Phys Chem B* **112**, 5547-5550, (2008).

293 Herce, H. D. & Garcia, A. E. Molecular dynamics simulations suggest a mechanism for translocation of the HIV-1 TAT peptide across lipid membranes. *Proc Natl Acad Sci U S A* **104**, 20805-20810, (2007).

294 Duan, Y. *et al.* A point-charge force field for molecular mechanics simulations of proteins based on condensed-phase quantum mechanical calculations. *J Comput Chem* **24**, 1999-2012, (2003).

295 AMBER 11 v. 11 (University of California, San Francisco, 2010).

296 Dupradeau, F. Y. *et al.* The R.E.D. tools: advances in RESP and ESP charge derivation and force field library building. *Phys Chem Chem Phys* **12**, 7821-7839, (2010).

297 Mitsutake, A., Sugita, Y. & Okamoto, Y. Generalized-ensemble algorithms for molecular simulations of biopolymers. *Biopolymers* **60**, 96-123, (2001).

298 Huang, J. & MacKerell, A. D., Jr. CHARMM36 all-atom additive protein force field: validation based on comparison to NMR data. *J Comput Chem* **34**, 2135-2145, (2013).

299 Mangoni, M. L. *et al.* Comparative analysis of the bactericidal activities of amphibian peptide analogues against multidrug-resistant nosocomial bacterial strains. *Antimicrob Agents Chemother* **52**, 85-91, (2008).

300 Serresi, M., Bizzarri, R., Cardarelli, F. & Beltram, F. Real-time measurement of endosomal acidification by a novel genetically encoded biosensor. *Anal Bioanal Chem* **393**, 1123-1133, (2009).

301 Cardarelli, F., Pozzi, D., Bifone, A., Marchini, C. & Caracciolo, G. Cholesterol-dependent macropinocytosis and endosomal escape control the transfection efficiency of lipoplexes in CHO living cells. *Mol Pharm* **9**, 334-340, (2012).

302 Silve, A., Leray, I. & Mir, L. M. Demonstration of cell membrane permeabilization to medium-sized molecules caused by a single 10 ns electric pulse. *Bioelectrochemistry* **87**, 260-264 (2012).

Acknowledgements

I would like to express my gratitude to many people for their support and assistance during my PhD experience.

My first acknowledgements go to my advisor, Fabio Beltram: I had the luck of working with him in these years of PhD study. I would like to thank him for giving me the opportunity to work in the NEST research center: his constant support and precious suggestions stimulated me many times in improving my work and in succeeding in this research project.

I would also like to thank Francesco Cardarelli and Michela Serresi for their good friendship and for closely helping me in organizing the measurements and in interpreting experimental results. I gratefully acknowledge as well Giovanni Signore and Claudia Boccardi for their constant and precious technical support. During these years I also benefited from stimulating discussions with Barbara Storti and Carmine Di Rienzo, and I get this chance to thank them.

Of course I would say a real big “thank you!” to all the people I had the pleasure to meet at the NEST laboratory and at Scuola Normale Superiore, and who helped me in many ways: among these The Leader, F. Forandini, David Porciani&Blondie, Mariagrazia Di Luca, Riccardo Nifosí, Sara Macchi, Gerardo Abbandonato, Subrata Mal, Sebastian Sulis Sato, Giacomo Lanza, Marco Brondi, Paolo Faraci, Laura Marchetti, Marco Travagliati and all the PhD and undergraduate students in the lab.

Last but not least, a mention goes to my family and all my friends: they did not contribute directly to this work but they were part of my everyday life, giving me the strength to face many difficulties.